NEUTRON DIFFRACTION STUDIES OF THE TEMPERATURE DEPENDENCE OF THE SUBLATTICE MAGNETIZATION AND SPIN CORRELATIONS OF IRON CARBONATE

A THESIS

Presented to

The Faculty of the Division of Graduate

Studies and Research

by

Ralph Frederick Altman

In Partial Fulfillment

of the Requirements for the Degree

Doctor of Philosophy

in the School of Physics

Georgia Institute of Technology

February, 1975

NEUTRON DIFFRACTION STUDIES OF THE TEMPERATURE DEPENDENCE OF THE SUBLATTICE MAGNETIZATION AND SPIN CORRELATIONS OF IRON CARBONATE

Approved:

Chairman

Date approved by Chairman: 12/2/74

ACKNOWLEDGMENTS

The author wishes to thank his thesis advisor, Dr. S. Spooner, for guidance and advice given during the course of this investigation. The many helpful discussions with Drs. H. A. Gersch and D. P. Landau who served as members of the reading committee are gratefully acknowledged. The counsel and encouragement of these three men were invaluable.

The author expresses his appreciation to Dr. J. E. Rives for his help with some of the experimental aspects of the investigation and to H. A. Mook for making his $FeCO_3$ inelastic scattering data available. Thanks are extended to Drs. J. Stevenson and D. C. O'Shea for serving on the thesis defense committee. The author is grateful to the members of the staff of the Georgia Tech Research Reactor for their assistance in gathering the neutron diffraction scattering data and to Mrs. Lydia S. Geeslin for her help in preparing this manuscript.

Finally, the author would like to thank his wife and daughters for their patience, love, and support during this endeavor.

This research was supported by U. S. Atomic Energy Commission contract #AT-(40-1)-3674.

TABLE OF CONTENTS

TABLE OF CONTENTS (Concluded)

LIST OF TABLES

LIST OF ILLUSTRATIONS

LIST OF ILLUSTRATIONS (Continued)

LIST OF ILLUSTRATIONS (Concluded)

SUMMARY

Previous experiments indicate that the magnetic properties of the highly anisotropic antiferromagnetic material $FeCO_3$ can be accurately described using an Ising model Hamiltonian. The unique temperature dependence of the sublattice magnetization and the spin correlations of an Ising system provide a means of testing the Ising character of a magnetic system and of defining the Hamiltonian parameters. This dissertation is concerned with the measurement of these properties using neutron diffraction techniques and their calculation using a Monte Carlo computer technique.

The integrated intensity of the (300) magnetic Bragg peak of $FeCO_3$ was measured from 6.6 K to 40.1 K using a double axis neutron diffractometer. From these data, the sublattice magnetization was determined. The sublattice magnetization was then calculated as a function of temperature using a Monte Carlo technique based on an Ising model Hamiltonian of the form:

$$H = K_{NN} \sum_{i,j} \sigma_{iz} \sigma_{jz} + K_{NNN} \sum_{i,k} \sigma_{iz} \sigma_{kz}$$

where the sums i,j and i,k are taken over pairs of nearest and next-nearest neighbors, respectively. The nearest neighbor constant, K_{NN}, was determined to be 7.4 K and the next-nearest neighbor constant, K_{NNN}, was determined to be -1.6 K. The agreement between the neutron results and the Monte Carlo results is only fair if the impurity content of the natural

sample indicated the presence of two percent magnesium and three percent manganese by weight. When models of these impurity ions are included in the Monte Carlo calculation, the results are in excellent agreement with the neutron data.

Diffuse magnetic data were taken at three temperatures above the Néel temperature of a second natural $FeCO_3$ sample. To minimize inelastic scattering effects the data were taken using a triple axis diffractometer with the energy analyzing axis set to accept elastically scattered neutrons. The neutron diffraction cross section for diffuse scattering was calculated using spin correlation coefficients which were generated by the Monte Carlo program. The calculated cross section falls well within the statistical accuracy of the neutron data, with one exception. There is a diffraction vector dependent anisotropy in the neutron data that does not appear in the calculated cross section. Further work in the areas of the magnetic form factor of $FeCO_3$ or spin correlations may reveal the origin of the anisotropy, but a satisfactory explanation was not developed during this investigation. One striking feature of the diffuse neutron data that is characteristic of Ising systems is the persistence of the magnetic anisotropy above the ordering temperature.

CHAPTER I

INTRODUCTION

The magnetic properties of iron carbonate have been broadly investigated. The properties studied include the magnetic structure,[1] susceptibility,[2,3,4] magnetization,[2,5,6] and specific heat.[7] The electronic transitions of the Fe^{2+} ion in $FeCO_3$ have been measured in both Raman[8,9] and infrared[10] studies. Relaxation frequencies and the hyperfine interaction have been investigated in Mössbauer[11,12,13] studies, and the magnon energy versus wavevector relationship has been determined in an inelastic neutron scattering experiment.[14]

One of the reasons for the interest in $FeCO_3$ is the highly anisotropic character of the Fe^{2+} ground state. The crystal field levels of the iron ion are not completely understood.[8,9,10] However, the experimental evidence indicates that the ground state can be accurately described by an Ising Hamiltonian. This Ising character was first suggested by J. Kanamori in a crystal field study of the Fe^{2+} ion in $FeCL_2$[15] and in the later extension of this work to explain Mössbauer data taken on $FeTiO_3$ and $FeCO_3$.[13]

Three of the experiments in particular provide strong evidence for this Ising character. The first is the magnetization study[2] in which a metamagnetic transition, which is peculiar to highly anisotropic materials, was observed. This transition is one from a fully ordered antiferromagnetic state to a ferromagnetic state in the presence of an external field applied along the spin direction. The second is the Mössbauer study by

Koon[11] in which slow electronic relaxations are measured. Slow electronic relaxations are characteristic of Ising systems. Finally, there is the neutron scattering experiment by Wrege.[14] In this study, magnon energies were found to have very little, if any, wavevector dependence, as would be expected of magnons in an Ising system. More will be said about these experiments and the others as their results become relevant to the discussion.

The Hamiltonian of Magnetic Ising Systems

The simple form of the Ising Hamiltonian is responsible for the interest in Ising systems. The simplest form of the Hamiltonian for a spin only exchange coupled magnetic system that includes anisotropy is

$$H = \sum_{i,j}{}' \left\{ J_{\|}(\vec{r}_i - \vec{r}_j) S_i^z S_j^z + J(\vec{r}_i - \vec{r}_j)(S_i^x S_j^x + S_i^y S_j^y) \right\} \qquad (1)$$

where the sum (i,j) is taken over pairs of magnetic ions, J is the exchange integral for the pairs of ions separated by distance $\vec{r}_i - \vec{r}_j$, and $\vec{S}_i$ and $\vec{S}_j$ are the spin angular momentum operators for ions at the i^{th} and j^{th} sites. In the isotropic limit, the Hamiltonian has the Heisenberg form

$$H = \sum_{i,j}{}' J(\vec{r}_i - \vec{r}_j)\vec{S}_i \cdot \vec{S}_j \ . \qquad (2)$$

The isotropic form appears to be more manageable, but is still complicated by the fact that the individual angular momenta, $\vec{S}_i$, do not commute with the Hamiltonian. In the extreme anisotropic or Ising limit, a significant simplification occurs. In this limit, the Hamiltonian has the Ising form

$$H = \sum_{i,j} J(\vec{r}_i - \vec{r}_j) S_i^z S_j^z \quad , \tag{3}$$

and the operators S_i^z, S_j^z do commute with the Hamiltonian. Since S_i^z and S_j^z commute with the Hamiltonian, they are constants of the motion. The temperature series expansions for their thermal expectation values are relatively simple, and these series have been calculated for some common crystal systems.

Magnetic Properties of Ising Systems

If the Hamiltonian of a magnetic quantum mechanical system is known, then the thermal equilibrium value of a magnetic property of the system is given by

$$< F > = \int d\vec{q}\ F(\vec{q}) e^{-E(\vec{q})/kT} / \int d\vec{q}\ e^{-E(\vec{q})/kT} \quad . \tag{4}$$

If the system has discrete energy levels, as an Ising system does, then the thermal equilibrium value of property F is given by

$$< F > = \sum_u F(u) e^{-E_u/kT} / \sum_u e^{-E_u/kT} \tag{5}$$

where the sum u is over all possible energy Eigenstates for the system and F(u) and E_u are respectively the property value and the energy of configuration u. This sum is equivalent to the trace of a matrix, and from this fact, it follows that it does not matter what set of system configurations is used in the evaluation of the sum, so long as the set is a complete set for the system.

The sum (5) is simple in form but difficult to evaluate, even for an Ising system. Consider a system of N spin one half atoms periodically arranged in space with their spins constrained to lie along an axis of quantization. For this array of spins, the sum contains 2^N terms. For a collection of 100 spins, there would be $\simeq 1.27 \times 10^{30}$ terms, and this is an impossible number of terms to handle even with the fastest computers.

The Effective Field Theory Approach

Although sum (5) is difficult to evaluate directly, some exact solutions for two dimensional crystals exist. However, the three dimensional case has still not been solved exactly and approximate solutions for this case indicate that there are significant differences between the two and three dimensional cases. The simplest and the most commonly used approximations are the so called effective field approximations.[16] The approach taken in the effective field theories is the following. Instead of treating the Hamiltonian for an entire array of spins, the Hamiltonian for a small part of the array is treated exactly, and the effect of the rest of the spin system on the small part is treated in an approximate way. In the Weiss[17] molecular field approximation, the Hamiltonian for a single ion is treated separately. As an example, consider an Ising spin system that has first neighbor coupling only. The Hamiltonian for a single ion can be extracted from (3) and has the form

$$H_i = J\, S_i^z \sum_j S_j^z \qquad (6)$$

where there are n nearest neighbors. The approximation is now made that

the sum on j can be replaced by $n < S_j^z >$. The single ion Hamiltonian is rewritten as

$$H_i = - g\mu_\beta S_i^z H_{eff} . \tag{7}$$

Here the effective field, H_{eff}, is given by

$$H_{eff} = Jn < S_j^z > / g\mu_\beta , \tag{8}$$

μ_β is the magnetic moment of a Bohr magneton and g is the Lande' g-factor. To find the expectation value for S_i^z, one now uses (5) with Hamiltonian (8).

$$< S_i^z > = \sum_{S_i^z = -M_s}^{+M_s} S_i^z e^{-g\mu_\beta S_i^z H_{eff}} / \sum_{S_i^z = -M_s}^{+M_s} e^{-g\mu_\beta S_i^z H_{eff}} \tag{9}$$

$$= (M_s + \tfrac{1}{2})\operatorname{cotn}[(M_s + \tfrac{1}{2})x] - \tfrac{1}{2} \operatorname{cotn}(x/2)$$

where

$$x \equiv Jn < S_j > /kT \tag{10}$$

and M_s is the z component spin quantum number for the magnetic atoms under consideration. Now, for a ferromagnetic system, all the magnetic atoms in the array are assumed to be identical, so it is clear that $< S_i > = < S_j >$, and therefore (9) can be used to find $< S_i^z > = < S^z >$ as a function of temperature.

The simple approximation described above yields a temperature dependence for $< S^z >$ that is qualitatively correct, but quantitatively incorrect. A spontaneous ordering temperature is predicted by (9), but its value has been shown to be high by as much as 40 percent.[16] Later in this thesis, the functional dependence of $< S >$ on temperature will also be shown to have a significant error in it. For properties above the ordering temperature, the Weiss molecular field approximation does not produce even qualitatively correct results. In particular, this model predicts no short range order above the ordering temperature.

The more sophisticated effective field theories treat the Hamiltonian of a pair or more atoms exactly. Oguchi[18] first treated the pair Hamiltonian exactly. But his treatment again assumed that the interaction of the pair with the rest of the crystal was proportional to the average magnetization of the sample. This treatment produces a slight improvement in the predicted ordering temperature and predicts a finite short range order above the critical temperature. But the Oguchi approximation leads to essentially the same temperature dependence for the magnetization that the Weiss approximation produces. The more complicated effective field theories produce improved results for some limited temperature ranges. However, none of them produce accurate results over a broad temperature range. For instance, both the constant coupling approximation[19] and the Bethe-Peierls-Weiss[20] approximation produce a more accurate temperature dependence for the magnetization of a sample close to the ordering temperature than the first two approximate methods do. However, the constant coupling method does not predict complete magnetic saturation at zero

temperature in the absence of an external magnetic field. The B-P-W method predicts that the spontaneous magnetization passes through a maximum and then returns to zero at a finite temperature.

Temperature Series Approximations

Another technique that is commonly used to obtain approximations for the sum (5) are temperature series expansions. Two methods are used extensively. The first method is expansion by cumulants, and the second method uses Padé approximants. Only some of the more relevant results will be cited here.

Rather than trying to evaluate sum (5) directly, a temperature series is written for the partition function or its logarithm, and thermal equilibrium property values are calculated from this series by taking the appropriate thermodynamic derivative. The Hamiltonian usually has the form

$$H = \sum_{i,j}{}' J(\vec{r}_i - \vec{r}_j) S_i^z S_j^z - g\mu_\beta H_o \sum_{i=1}{}' S_i^z \qquad (11)$$

where the first sum is the same sum used in (1) and H_o is an external magnetic field. The partition function is defined by

$$Z = \text{TRACE}(e^{-H/kT}) \ . \qquad (12)$$

The two quantities that are of the most interest for this discussion are $< S_i^z >$ and the susceptibility, χ. These quantities are given by

$$< S_i^z > = kT \frac{\partial}{\partial H_o} [\ln(Z)]/Ng\mu_\beta \qquad (13)$$

and

$$\chi = kT \frac{\partial^2}{\partial H_o^2} [\ln(Z)] . \tag{14}$$

A number of authors[21,22] have made high temperature expansions in powers of $\frac{1}{kT}$ for the logarithm of Z by cumulants. From this expansion, they calculate a series for χ and also $\frac{1}{\chi}$. The reciprocal of the susceptibility is of interest because $\frac{1}{\chi}$ is expected to go to zero at the ordering temperature. The ordering point can therefore be estimated by finding the smallest positive zero of the $\frac{1}{\chi}$ series. The ordering temperature is found to depend on the spin quantum number S, the number of neighbor interactions considered, and crystal system. These are the results that indicate that the effective field ordering temperatures are high.

A good deal of work has been done on the critical indices for Ising systems using Padé approximants, and these results are more general in nature. Low temperature series expansions[23] indicate that just below the ordering point $< S_i >$ should vary as

$$< S_i > \propto (1 - T/T_N)^{\beta} \tag{15}$$

with $\beta = 0.312 \, ^{+0.003}_{-0.006}$.[24,25] The value of β has been shown to be very insensitive to the details of the crystal system. A Mössbauer study[11] of long range order in $FeCO_3$ indicates that, close to the critical temperature, $FeCO_3$ obeys this power law very well and confirms the β value just quoted.

High temperature series results[26] indicate that just above the

ordering temperature the spin correlations, defined as $< S(\vec{r}_i)S(\vec{o}) >$, obey a modified Ornstein-Zernike law. The modified form is

$$< S^z(\vec{r}_i)S^z(\vec{o}) > \propto e^{-\kappa|\vec{r}_i|}/|\vec{r}_i|^{(1+\eta)} \tag{16}$$

with $\eta = 0.056 \pm 0.008$ for Ising systems. The inverse correlation range parameter κ is found to have the form

$$\kappa \propto (T/T_N - 1)^{\nu} \tag{17}$$

with $\nu = 0.643 \pm 0.003$ for three dimensions. These results have been compared with neutron diffraction data[27] on the binary alloy system Beta-Brass, with good agreement. However, a corroborating experiment on a magnetic Ising system has yet to be performed.

The Monte Carlo Technique

Two problems are consistently encountered in using all of the approximate techniques discussed so far. Either the method is easy to use but does not produce very accurate results, or the method involves a tedious calculation and is only valid for a limited temperature range and a specific crystal model. There is an additional consideration that has not been discussed but is rather evident. As the physical system under study becomes more complicated, the arithmetic required to use these approximate techniques to treat the system becomes more involved. The first complication that one would like to treat is the addition of interactions with more than the first shell of neighbors. A second and less tractable complication

is the inclusion of impurity ions in the host magnetic lattice.

All of these complications can be handled rather easily, however, using the Monte Carlo technique. This technique was first used to treat an interacting many body system by Metropolis.[28] The essence of the technique is as follows. Consider again the expression for the expectation value for some property F. Instead of trying to evaluate every term in the sum (5), one could estimate its value by choosing only a small number of terms. The value of the sum would depend upon the method used to select the terms. System configurations could, for example, be selected at random and the properties for these configurations used in the evaluation of the sum. A better way to choose the system configurations would be to choose only those configurations that make a large contribution to the sum. This method is generally called importance sampling, and is just the selection that the Monte Carlo technique described in this dissertation produces.

The Monte Carlo technique can be used to calculate the temperature dependence of any magnetic property that can be defined by (5). In particular, it can be used to calculate both the sublattice magnetization and spin correlation coefficients. The technique is particularly useful in treating systems like $FeCO_3$ for which temperature series do not exist. Only one real problem is encountered in the use of this technique. The calculation is in practice carried out for a model of finite size, but the experimental results used for comparison are from a sample that is effectively infinite in size. To make a meaningful comparison, the Monte Carlo calculation must be carried out for models of different sizes, and an extrapolation of the results to infinite size must then be made.

Fortunately, the finite size effects are important only for temperatures close to the ordering temperature where the series expansions give good results. The two computational techniques therefore complement each other and allow a dependable prediction of property values over the entire temperature range of interest.

The Study of Long Range Order with Neutron Diffraction

A magnetic order parameter and the hyperfine field have been measured as a function of temperature using Mössbauer techniques.[11,12,13] In the work by Koon, the temperature dependence of the order parameter was established with good accuracy near the ordering temperature. His results indicate that the long range order parameter, η, is given by the power law

$$\eta = D(1 - T/T_N)^{\beta} \tag{18}$$

with $\beta = .318 \pm .002$. The result is in good agreement with the value of $\beta = .312 \begin{smallmatrix} +.003 \\ -.006 \end{smallmatrix}$ calculated for a cubic Ising model. In this work, the results close to the ordering temperature are based on the location of peak positions and are very accurate. However, the order parameter for temperatures less than 0.9 T_N were determined primarily by the broadening of the peaks. The analysis of the data in this region produced a large error limit on the order parameter.

In addition to the problem of accuracy, the analysis of the Mössbauer data is sufficiently involved that there remains some question as to the relationships between the order parameter η, the hyperfine field, and the sublattice magnetization of the sample. The Mössbauer studies were the

only experiments from which information on long range order in $FeCO_3$ could be obtained. In view of the problems of accuracy and interpretation, an independent measurement of the sublattice magnetization was undertaken. Neutron diffraction provides a relatively direct means of measuring this quantity. As will be shown later, the sublattice magnetization is simply related to the integrated intensity of a magnetic Bragg peak.

Only two experimental complications arise when the neutron diffraction method is used. The first problem is called secondary extinction and can almost be eliminated by careful sample selection. The second problem is that of diffuse scattering. This problem is more difficult to deal with. As the sample temperature is raised close to the ordering point, the intensity of a magnetic Bragg peak falls towards zero. At the same time, neutron scattering due to fluctuations in the spin density, or critical scattering, increases. It is difficult to correct for critical scattering below the ordering point because a good theory for the description of this scattering has yet to be developed. However, the dependence of critical scattering on the scattering angle is sufficiently different from the Bragg scattering dependence to allow an approximate correction to be made.[29] Additionally, in the region close to the ordering temperature, the Mössbauer work provides evidence that the sublattice magnetization can be treated using the power law just cited. In this respect, these two experimental techniques complement each other.

The Study of Short Range Order with Neutron Diffraction

No previous attempt to measure short range order in $FeCO_3$ above the ordering temperature has been made. Neutron diffraction again provides a

relatively direct method of determining the spacial dependence of spin correlations as a function of temperature. This experiment is more difficult than the Bragg experiment, however. The biggest problem is the lack of intensity of diffracted neutrons. The cross section for critical scattering is an order of magnitude smaller than the Bragg scattering cross section. The low counting rates that result mean that the sample must be held at a fixed temperature for long periods of time. For $FeCO_3$, the temperatures of interest lie about halfway between liquid helium and liquid nitrogen temperatures, and a sophisticated temperature control unit is required.

The analysis of the diffuse (critical scattering) data is also more difficult. A detailed knowledge of the magnetic form factor of the Fe^{2+} ion is required, as well as an accurate measurement of the resolution characteristics of the diffractometer used in the study. Further, the diffuse scattering, which is elastic, is of the same order of magnitude as the inelastic scattering from phonons and magnons. The inelastic scattering must either be eliminated experimentally, or an attempt must be made to account for the inelastic contribution to the data. Previous attempts at this correction have been less than satisfactory. Fortunately, the Ising nature of $FeCO_3$ does simplify the situation. Recent inelastic neutron studies[14,30] indicate that there are no magnons in $FeCO_3$ with energies less than 0.0106 eV above the ordering temperature. An energy analyzing axis can therefore be used to eliminate all of the magnon scattering from the data. This third axis of the diffractometer also minimizes the phonon contribution to the data.

Summary of Objectives

First, the sublattice magnetization of $FeCO_3$ is measured from liquid helium temperature through the ordering point using neutron diffraction. The sublattice magnetization for an Ising system is calculated using the Monte Carlo technique. The effects of second nearest neighbor interactions and impurities on this temperature dependence are investigated. A comparison between the neutron diffraction results and the Monte Carlo results is made as a further test of the Ising character of $FeCO_3$. This comparison allows the determination of the interaction constants appropriate to $FeCO_3$.

Diffuse magnetic data are collected above the ordering temperature with a triple axis diffractometer. Spin correlation coefficients are generated, again with the Monte Carlo technique. Comparison is made with the high temperature series results. The spin correlation coefficients are Fourier inverted to give the wave vector dependent susceptibility, and comparison is made with the diffuse neutron data.

CHAPTER II

THEORY

Crystal Field Theory

The characteristic of $FeCO_3$ that has caused the interest in this material is the Ising nature of the Fe^{2+} ground state. Although the crystal field energy levels of the Fe^{2+} ion are not central to this dissertation, the Ising nature of the ground state clearly is. So, before proceeding further, it is necessary to consider the crystal field studies that have played such an important role in establishing the Ising character. Three important points will be discussed. The first is that the ground state of the Fe^{2+} ion is a doublet that is split by an exchange interaction. The second is that for this doublet ground state all of the transverse angular momentum components $< L^x >$, $< L^y >$, $< S^x >$, $< S^y >$ are zero. Here $\vec{L}$ is the orbital angular momentum operator for an ion and $\vec{S}$ is the spin angular momentum operator. The trigonal axis is assumed to lie along the Z axis (see Figure 1). The third point is that the first excited state for the ion has an energy that is high enough not to affect magnetic properties up to and a little above the transition temperature.

Before starting the discussion of the crystal field results, one more point should be mentioned. The Heisenberg Hamiltonian that is most commonly encountered has the form

$$H = \sum_{i,j} J(\vec{r}_i - \vec{r}_j)(S_i^x S_j^x + S_i^y S_j^y + S_i^z S_j^z) \qquad (19)$$

where the sums i,j are again taken over pairs of magnetic ions. The object of this section is to argue that for the ground state of the Fe^{2+} ion in $FeCO_3$, the Hamiltonian can be reduced to the form

$$H = \sum_{i,j}' J(\vec{r}_i - \vec{r}_j)\sigma_i^z\sigma_j^z \tag{20}$$

where σ_i^z and σ_j^z can take on only two possible values which are chosen to be ± 1 for convenience.

The problem is the following. Strictly speaking, the form (19) is applicable only to magnetic ions that have no orbital angular momentum. The Hamiltonian is more complicated for ions whose orbital angular momentum has a non zero expectation value. All of the experimental as well as the theoretical work on $FeCO_3$ indicates that the orbital angular momentum of the Fe^{2+} ion has a non zero expectation value. However, a more complicated Hamiltonian is still not needed to discuss the exchange split ground doublet for the following reason. It has been demonstrated that $FeCO_3$ undergoes a metamagnetic transition below the ordering temperature.[2] This transition means that the smallest anisotropic energy splitting is much larger than the exchange splitting. This fact, in turn, suggests that at low temperatures, when an Fe^{2+} ion turns over, both its spin and orbital angular momentum reverse direction at once, and there are only two possible states for each ion. It remains to be shown that the spin orbit coupling and the exchange interaction, which are both normally isotropic, are in this case completely anisotropic. If these two points which are related to the three points mentioned earlier can be established, then the form

(20) should provide a reasonable representation for the ground state.

Kanamori[15] first postulated the Ising character of $FeCO_3$ in a paper on $FeCl_2$. Later Okiji and Kanamori[13] extended the study to $FeCO_3$. Kanamori's results were used to explain the Mössbauer results of Koon[11] and Ok[12] and also used in the interpretation of Wrege's[14] inelastic neutron data. Griffith[31] has also performed a crystal field calculation that is applicable to $FeCO_3$, and his treatment is more general than Kanamori's. Prinz, Forester, and Lewis[10] have elaborated on Griffith's work and used this more general approach to explain their infrared results as well as some recent Raman results.[8,9] The conclusions that are drawn from both approaches support the claim that the ground state of $FeCO_3$ is Ising like.

Figure 1 shows the rhombohedral unit cell of $FeCO_3$. Also shown are the six oxygen atoms at the corner of the unit cell. Taken together, these six oxygen atoms form a crystal field at the iron site that has a large component with cubic symmetry and a smaller component with trigonal symmetry. The cubic field splits the ^5D free Fe ion ground state ($L = 2$, $S = 2$) into a triplet and a doublet with a separation that is typically 10,000 cm^{-1} (Figure 2). The triplet lies lowest. The trigonal field splits the triplet into a singlet and a doublet with a separation of around 1,000 cm^{-1}. The assumption is then made that the doublet lies lowest.

Next, the spin orbit interaction is considered. In the limit that the trigonal splitting is very much larger than the spin orbit splitting, the spin orbit interaction splits the orbital doublet into five equally spaced doublets. The orbital part of the ground doublet has the form

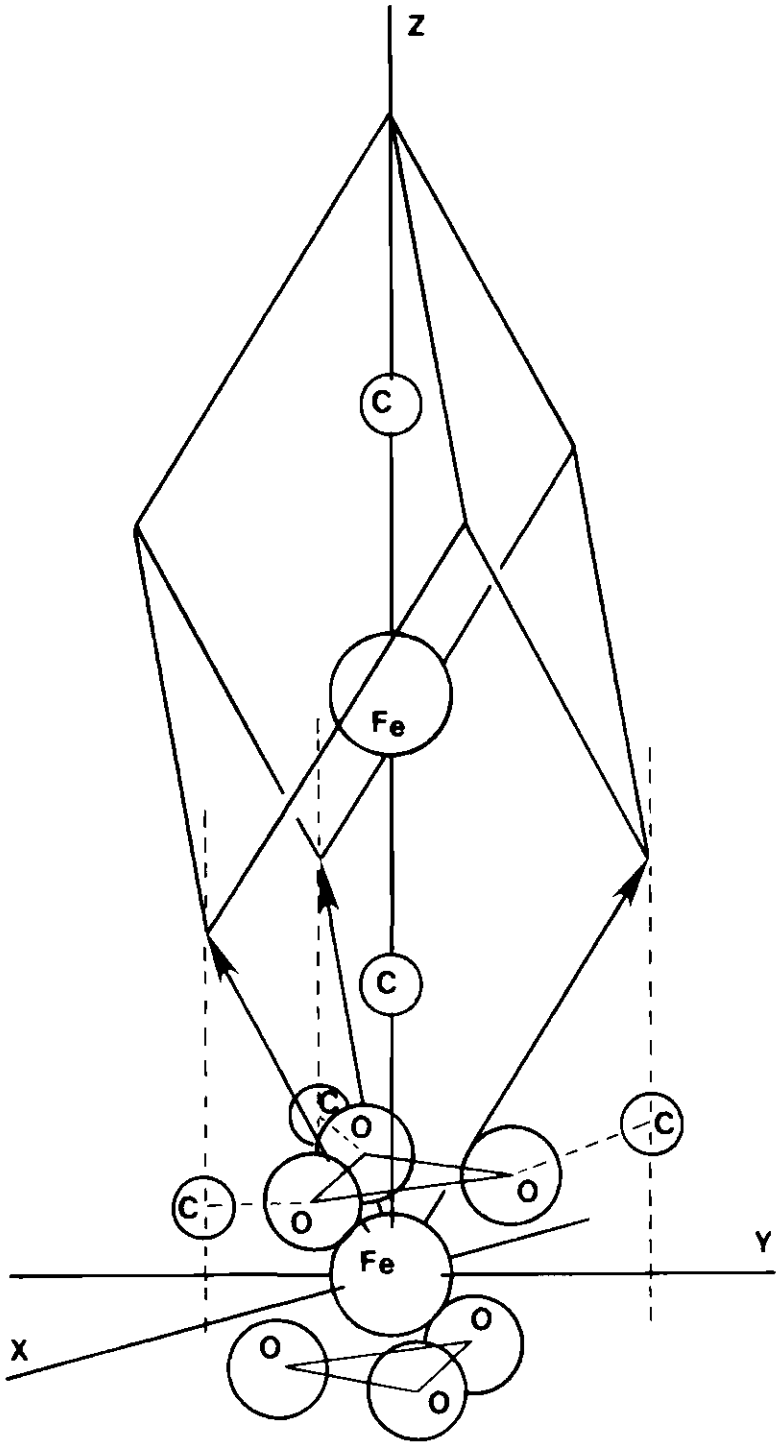

Figure 1. Rhombohedral Unit Cell of Iron Carbonate

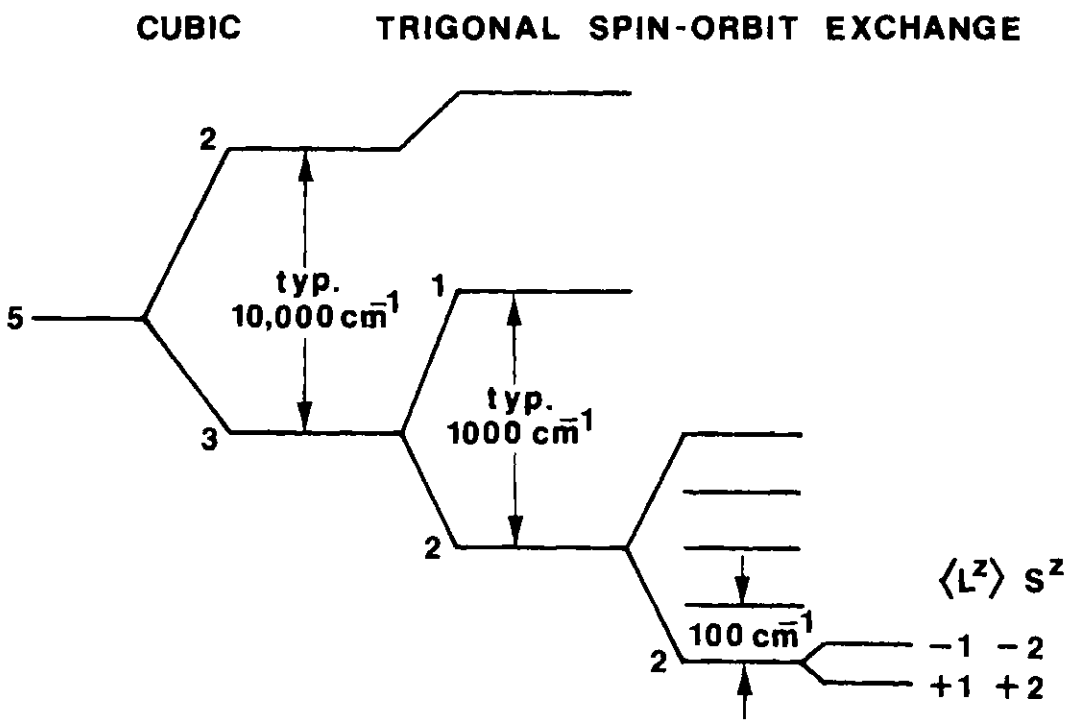

Figure 2. Kanamori's Crystal Field Splitting Scheme

$$\cos(\theta)\,|L=2,M_L=2> + \sin(\theta)\,|2,-1> \qquad (21)$$

$$\cos(\theta)\,|2,-2> - \sin(\theta)\,|2,1>$$

where θ is a mixing parameter that can be determined experimentally. When the spin part of the wave function is added, the lowest doublet has the form

$$\cos(\theta)\,|L=2,M_L=2,S=2,M_S=2> + \sin(\theta)\,|2,-1,2,2> \qquad (22)$$

$$\cos(\theta)\,|2,-2,2,-2> - \sin(\theta)\,|2,1,2,-2> .$$

Since L = 2 and S = 2 for all of these functions, it is convenient to shorten the form to

$$\cos(\theta)\,|M_L=2,M_S=2> + \sin(\theta)\,|-1,2> \qquad (23)$$

$$\cos(\theta)\,|-2,-2> - \sin(\theta)\,|1,-2> .$$

Finally, exchange splits this doublet as is indicated in Figure 2. The L^z value in Figure 2 is the value appropriate for a field of cubic symmetry.

The discussion so far has established the fact that the ground state is an exchange split doublet. The second point, the vanishing of the transverse components of angular momenta, can easily be established with the aid of the wave functions (23). Consider the x component of the orbital

angular momentum. This component can be expressed as

$$L^x = \frac{1}{2}\,(L^+ + L^-) \tag{24}$$

where L^+ and L^- are the usual raising and lowering operators. The expectation value of L^x for the first state of (23) is zero:

$$\sin(\theta) < 2,-1| + \cos(\theta) < 2,2|[\tfrac{1}{2}(L^+ + L^-)]\cos(\theta)|2,2 > \tag{25}$$

$$+ \sin(\theta)|-1,2> = \frac{1}{2}\,[\sin(\theta)\cos(\theta) < 2,-1|L^+|2,2 >$$

$$+ \sin(\theta)\cos(\theta) < 2,-1|L^-|2,2 > + \sin^2(\theta) < 2,-1|L^+|-1,2 >$$

$$+ \sin^2(\theta) < 2,-1|L^-|-1,2 > + \cos^2(\theta) < 2,2|L^+|2,2 >$$

$$+ \cos^2(\theta) < 2,2|L^-|2,2 > + \cos(\theta)\sin(\theta) < 2,2|L^+|-1,2 >$$

$$+ \cos(\theta)\sin(\theta) < 2,2|L^-|-1,2 > = 0\ ,$$

since, in this case, every term in (25) vanishes individually. Clearly, L^y, S^x, and S^y can all be shown to be zero in the same manner.

The third point to be considered, the splitting between the first and second doublet, depends on the size of the spin orbit coupling. Yamada[32] predicted that the transition from the ground doublet to the first excited doublet could be measured with neutrons, and this transition has since

been measured both above and below the ordering temperature.[14,30] The transition was also measured in an infrared study.[10] The results all agree and give a splitting of around 100 cm^{-1}. This value is in good agreement with Kanamori's[15] original prediction which was based on the size of the free ion spin orbit coupling constant. The Néel temperature for $FeCO_3$ is about 40 K, and so it is safe to assume that there is little thermal population of excited states at the temperatures considered in this work (100 $cm^{-1} \approx$ 144 K).

To this point, only Kanamori's results have been used. These results are based on the assumption that the trigonal field splitting is very much larger than the spin orbit coupling. Griffith dropped this restriction in his work. The Hamiltonian that he chose to diagonalize had the form

$$H = \lambda \vec{L}_i \cdot \vec{S}_i + \delta[(L_i^z)^2 - \frac{2}{3}] + \mu_\beta \vec{H} \cdot (-\vec{L}_i + 2\vec{S}_i) \qquad (26)$$

where

$\lambda \vec{L}_i \cdot \vec{S}_i$ = the spin orbit coupling interaction,

$\delta[(L_i^z)^2 - \frac{2}{3}]$ = the trigonal field energy,

$\mu_\beta \vec{H} \cdot (-\vec{L}_i + 2\vec{S}_i)$ = the coupling to an external field.

Griffith uses an isomorphism in the evaluation of the matrix elements that result. One peculiarity of this method is that the operator $\vec{L}$ must be replaced by $-\vec{L}$ to calculate expectation values. Fortunately, the fundamental properties of the ground state do not change when this more general approach

is taken although some of the excited states do change significantly. The ground state is still an exchange split doublet and has the form

$$|M_L = -1, M_S = 2> + \epsilon[|0,1> + |1,0>] \qquad (27)$$

$$|1,-2> + \epsilon[|0,-1> + |-1,0>] \ .$$

Again, the matrix elements of the transverse components of angular momentum are zero. For example

$$\epsilon <0,1| + \epsilon <1,0| + <2,-1|[-\tfrac{1}{2}(L^+ + L^-)]\,|-1,2> \qquad (28)$$

$$+ \epsilon|0,1> + \epsilon|1,0> = -\tfrac{1}{2}[\epsilon <0,1|L^+|-1,2> + \epsilon <0,1|L^-|-1,2>$$

$$+ \epsilon^2 <0,1|L^+|0,1> + \epsilon^2 <0,1|L^-|0,1> + \epsilon^2 <0,1|L^+|1,0>$$

$$+ \epsilon^2 <0,1|L^-|1,0> + \epsilon <1,0|L^+|-1,2> + \epsilon <1,0|L^-|-1,2>$$

$$+ \epsilon^2 <1,0|L^+|0,1> + \epsilon^2 <1,0|L^-|0,1> + \epsilon^2 <1,0|L^+|1,0>$$

$$+ \epsilon^2 <1,0|L^-|1,0> + <2,-1|L^+|-1,2> + <2,-1|L^-|-1,2>$$

$$+ \epsilon <2,1|L^+|0,1> + \epsilon <2,1|L^-|0,1> + \epsilon <2,-1|L^+|1,0>$$

$$+ \epsilon <2,-1|L^-|1,0> = 0 \ .$$

Examination shows that each term vanishes individually.

These results are enough to establish the Ising character of the ground state. Since the ground state is a simple exchange split doublet, clearly the Hamiltonian reduces from form (19) to form (20), not because the exchange integral $J(\vec{r}_i - \vec{r}_j)$ is anisotropic as form (1) suggests, but because the spin and orbital angular momenta are anisotropic.

Neutron Diffraction Magnetic Cross Section

The general formula for the neutron scattering cross section is a first order perturbation theory result and is usually called the first Born approximation. It has the form[33]

$$\frac{d^2\sigma}{d\Omega\, dE} = \frac{|K_f|}{|K_i|} \left(\frac{M}{2\pi\hbar^2}\right)^2 \sum_{\lambda,\vec{\sigma}} P_\lambda P_\sigma \sum_{\lambda',\vec{\sigma}'} |\langle \vec{K}_f \vec{\sigma}' \lambda' | \vec{V} | \vec{K}_i \vec{\sigma} \lambda \rangle|^2 \times \qquad (29)$$

$$\times\, \delta(\hbar\omega + E_\lambda - E_{\lambda'})$$

where

Ω = solid angle,

E = final neutron energy,

$\vec{K}_f$ = final neutron wavevector,

$\vec{K}_i$ = initial neutron wavevector,

m = neutron mass,

P_λ = probability of crystal being in initial state λ,

P_σ = probability of neutron having initial spin σ,

$\vec{\sigma}'$ = final neutron spin,

$\vec{\sigma}$ = initial neutron spin,

λ' = final crystal state,

λ = initial crystal state,

$\vec{V}$ = interaction potential,

$\omega = \frac{\hbar}{2m}(|\vec{K}_f|^2 - |\vec{K}_i|^2)$ = neutron energy change,

E_λ = energy of the initial crystal state,

$E_{\lambda'}$ = energy of the final crystal state.

For magnetic scattering of unpolarized neutrons, the scattering potential is

$$\vec{V} = \gamma\mu_n \left\{ 2\mu_B \vec{\sigma} \cdot \text{CURL} \left[\frac{\vec{s} \times \vec{r}}{|\vec{r}|^3} \right] - \frac{e}{m_e c} \vec{P}_e \cdot \frac{\vec{\sigma} \times \vec{r}}{|\vec{r}|^3} \right\} \tag{30}$$

where

$\gamma\mu_n$ = the magnetic moment of a neutron,

$\vec{s}$ = the spin operator for the electron,

$\vec{r}$ = the radius vector from the electron to the neutron,

$\vec{P}_e$ = the momentum of an electron.

Well known identities can be used to make the following reduction

$$< \vec{K}_f | \vec{\sigma} \cdot \text{CURL} \left[\frac{\vec{s} \times \vec{r}}{|\vec{r}|^3} \right] - \frac{1}{\hbar} \vec{P}_e \cdot \frac{\vec{\sigma} \times \vec{r}}{|\vec{r}|^3} | \vec{K}_i > \tag{31}$$

$$= \frac{4\pi}{|\vec{K}|^2} \vec{\sigma} \cdot \left\{ e^{i\vec{K}\cdot\vec{r}} \left[\vec{K} \times (\vec{s} \times \vec{K}) - \frac{1}{\hbar} \vec{K} \times \vec{P}_e \right] \right\}$$

where

$\vec{K} = \vec{K}_i - \vec{K}_f$,

$\vec{r}$ = radius vector for the electron.

The potential can now be summed over unpaired electrons and inserted into the cross section to give

$$\frac{d\sigma^2}{d\,\Omega\,dE} = \left(\frac{m}{2\pi\hbar^2}\right)(2\gamma\mu_n\mu_\beta)^2(4\pi)^2 \sum_{\lambda,\sigma} P_\lambda P_\sigma \sum_{\lambda',\sigma'} \frac{|\vec{K}_f|}{|\vec{K}_i|} \times \tag{32}$$

$$\times \left| < \lambda'\vec{\sigma}' | \vec{\sigma} \cdot \vec{Q}_\perp | \lambda\vec{\sigma} > \right|^2 \delta(\hbar\omega + E_\lambda - E_{\lambda'})$$

where

$$\vec{Q}_\perp \equiv \sum_i e^{i\vec{K}\cdot\vec{r}_i} \left[\vec{K} \times (\vec{S}_i \times \vec{K}) - \frac{1}{\hbar}\vec{K} \times \vec{P}_i\right] . \tag{33}$$

For unpolarized neutrons, the cross section further reduces to

$$\frac{d^2\sigma}{d\,\Omega\,dE} = \left(\frac{\gamma e^2}{m_e c^2}\right)\frac{|\vec{K}_f|}{|\vec{K}_i|} \sum_\lambda P_\lambda \sum_{\lambda'} < \lambda | \vec{Q}_\perp^\dagger | \lambda' > \cdot < \lambda' | \vec{Q}_\perp | \lambda > \delta(\hbar\omega + E_\lambda - E_{\lambda'}) \tag{34}$$

where the $\dagger$ stands for the adjoint of an operator.

To this point, the results are rather general. The cross section that is appropriate for $FeCO_3$ will now be developed. The electrons in $FeCO_3$ are well localized about the iron sites, and it is therefore possible to redefine $\vec{Q}_\perp$ by

$$\vec{Q}_\perp = \sum_{\vec{l},\vec{d}} \frac{e^{i\vec{K}\cdot[\vec{l}+\vec{d}+\vec{u}(\vec{l},\vec{d})]}}{|\vec{K}|^2} \vec{Q}_\perp(\vec{l},\vec{d}) \tag{35}$$

where

$\vec{l}$ = radius vector to the corner of a unit cell,

$\vec{d}$ = radius vector from $\vec{l}$ to the equilibrium position of an Fe atom within the unit cell,

$\vec{u}(\vec{l},\vec{d})$ = the vector from $\vec{d}$ to the center of an Fe ion,

and

$$\vec{Q}_{\perp}(\vec{l},\vec{d}) \equiv \sum_{j} e^{\vec{K}\cdot\vec{r}_j(\vec{l},\vec{d})} \left[\vec{K} \times (\vec{S}_j \times \vec{K}) - \frac{i}{\hbar} \vec{K} \times P_e\right] \tag{36}$$

where the sum j is taken over unpaired electrons at the site $\vec{l} + \vec{d}$. It can be shown[34] that $\vec{Q}_{\perp}(\vec{l},\vec{d})$ can be written as an integral over the magnetic moment density of the electrons at the site $\vec{l} + \vec{d}$ in the following form

$$\vec{Q}_{\perp}(\vec{l},\vec{d}) = -\frac{1}{2\mu_B} \int d\vec{r}\ e^{i\vec{K}\cdot\vec{r}}\ \vec{K} \times M(\vec{l},\vec{d},\vec{r}) \times \vec{K} \tag{37}$$

where $M(\vec{l},\vec{d},\vec{r})$ includes contributions from both spin and orbital angular momentum. Now define

$$\vec{Q}(\vec{l},\vec{d}) \equiv -\frac{1}{2\mu_B} \int d\vec{r}\ e^{i\vec{K}\cdot\vec{r}}\ M(\vec{l},\vec{d},\vec{r}) \tag{38}$$

and the cross section can be rewritten as

$$\frac{d^2\sigma}{d\Omega\, dE} = \left(\frac{\gamma e^2}{m_e c^2}\right) \frac{|\vec{K}_f|}{|\vec{K}_i|} \sum_{\lambda} P_{\lambda} \sum_{\lambda'} \sum_{\vec{l}'\vec{d}'} \sum_{\vec{l}\vec{d}} e^{-i\vec{K}\cdot(\vec{l}'+\vec{d}')}\ e^{i\vec{K}\cdot(\vec{l}+\vec{d})} \tag{39}$$

$$\times \langle\lambda| e^{-i\vec{K}\cdot\vec{u}(\vec{l}',\vec{d}')} \vec{k} \times \vec{Q}^{\dagger}(\vec{l}',\vec{d}') \times \vec{k} |\lambda'\rangle$$

$$\cdot \langle\lambda'| e^{i\vec{K}\cdot\vec{u}(\vec{l}\vec{d})} \vec{k} \times \vec{Q}(\vec{l},\vec{d}) \times \vec{k} |\lambda\rangle \times \delta(\hbar\omega + E_{\lambda} - E_{\lambda'})$$

where

$$\vec{k} = \frac{\vec{K}}{|\vec{K}|} \quad . \tag{40}$$

The cross products with $\vec{k}$ and the dot product between the expectation values can be reduced to give

$$\frac{d^2\sigma}{d\,\Omega\,dE} = \left(\frac{\gamma e^2}{m_e c^2}\right) \frac{|\vec{K}_f|}{|\vec{K}_i|} \sum_{\lambda} P_\lambda \sum_{\lambda'} \sum_{\vec{l}',\vec{d}'} \sum_{\vec{l},\vec{d}} e^{-i\vec{K}\cdot(\vec{l}'+\vec{d}')}\, e^{i\vec{K}\cdot(\vec{l}+\vec{d})} \times \tag{41}$$

$$\times \sum_{\alpha,\beta}' (\delta_{\alpha,\beta} - k_\alpha k_\beta) \times \langle \lambda | e^{-i\vec{K}\cdot\vec{u}(\vec{l}',\vec{d}')}\, Q_\alpha^\dagger(\vec{l}',\vec{d}') | \lambda' \rangle \times$$

$$\times \langle \lambda' | e^{i\vec{K}\cdot\vec{u}(\vec{l},\vec{d})} Q_\beta(\vec{l},\vec{d}) | \lambda \rangle \, \delta(\hbar\omega + E_\lambda - E_{\lambda'})$$

with $\alpha,\beta = x,y,z$. A formalism first introduced by Van Hove[35] will now be used. With the identity

$$\delta(\hbar\omega + E_\lambda - E_{\lambda'}) = \frac{1}{2\pi\hbar} \int_{-\infty}^{\infty} e^{-it\left(\frac{\hbar\omega + E_\lambda - E_{\lambda'}}{\hbar}\right)} \tag{42}$$

and the definition

$$\vec{A}(t) \equiv e^{i\frac{Ht}{\hbar}}\, \vec{A}\, e^{-i\frac{Ht}{\hbar}} \tag{43}$$

the product of the expectation values in the cross section can be written as

$$\frac{1}{2\pi\hbar}\int e^{-i\omega t} < \lambda | e^{-i\vec{K}\cdot\vec{u}(\vec{l}',\vec{d}',t)}\ Q_\alpha^\dagger(\vec{l}',\vec{d}',t) | \lambda' > \times \tag{44}$$

$$\times < \lambda' | e^{i\vec{K}\cdot\vec{u}(\vec{l},\vec{d},0)}\ Q_\beta(\vec{l},\vec{d},0) | \lambda > \ .$$

Again following Van Hove, the cross section can be split into an elastic and an inelastic part. The part of the cross section that is elastic in both the nuclear and the spin systems is obtained by taking the long time limit of the expectation values. This "quasi-elastic" limit is the only part of the cross section that will be considered in the rest of the discussion. This limit will be indicated by replacing t with ∞ in the arguments of the time dependent operators.

In the long time limit, the spin motions and the nuclear motions are, to a good approximation, independent. The expectation values can therefore be written as

$$\frac{1}{2\pi\hbar}\int e^{-i\omega t} \sum_{\lambda(u)}' P_\lambda(u) \sum_{\lambda'(u)}' < \lambda(u) | e^{-i\vec{K}\cdot\vec{u}(\vec{l}',\vec{d}',\infty)} | \lambda'(u) > \times \tag{45}$$

$$\times < \lambda'(u) | e^{i\vec{K}\cdot\vec{u}(\vec{l},\vec{d},0)} | \lambda(u) > \times \sum_{\lambda(s)}' P_\lambda(s) \sum_{\lambda(s)}' < \lambda(s)$$

$$| Q_\alpha^\dagger(\vec{l}',\vec{d}',\infty) | \lambda'(s) > \cdot < \lambda'(s) | Q_\beta(\vec{l},\vec{d},0) | \lambda(s) > \ .$$

The first product in this last expression can be replaced with the usual Debye-Waller factor $e^{-2W(\vec{K})}$. When these last substitutions are made, the cross section is

$$\frac{d^2\sigma}{d\,\Omega\,dE} = \left(\frac{\gamma e^2}{m_e c^2}\right) \frac{|\vec{K}_f|}{|\vec{K}_i|}^2 e^{-2W(\vec{K})} \sum_{\alpha,\beta}' (1 - k_\alpha k_\beta) \sum_{\vec{l}',\vec{d}'} \sum_{\vec{l},\vec{d}} e^{-i\vec{K}\cdot(\vec{l}'+\vec{d}')} \times \tag{46}$$

$$\times\, e^{i\vec{K}\cdot(\vec{l}+\vec{d})} \times \frac{1}{2\pi\hbar} \int dt\, e^{-i\omega t} \sum_{\lambda}' P_\lambda \sum_{\lambda'}' < \lambda | Q_\alpha^\dagger(\vec{l}',\vec{d}',\infty) | \lambda' > \times$$

$$\times < \lambda' | Q_\beta(\vec{l},\vec{d},0) | \lambda > .$$

The cross section will now be reduced to the form that is appropriate for an Ising system. In the long time limit, the only component of $\vec{Q}(\vec{l},\vec{d},\infty)$ that does not have a zero expectation value is the z component (M_z is a constant of the motion). The sum on α,β can therefore be reduced to give

$$\frac{d^2\sigma}{d\,\Omega\,dE} = \left(\frac{\gamma e^2}{m_e c^2}\right) \frac{|\vec{K}_f|}{|\vec{K}_i|} e^{-2W(\vec{K})} (1 - k_z^2) \sum_{\vec{l}',\vec{d}'}' \sum_{\vec{l},\vec{d}}' e^{-i\vec{K}\cdot(\vec{l}'+\vec{d}')} \times \tag{47}$$

$$\times\, e^{i\vec{K}\cdot(\vec{l}+\vec{d})} \times \frac{1}{2\pi\hbar} \int e^{-i\omega t} \sum_{\lambda}' P_\lambda \sum_{\lambda'}' < \lambda | Q_z^\dagger(\vec{l}',\vec{d}',\infty) | \lambda' > \times$$

$$\times < \lambda' | Q_z(\vec{l},\vec{d},0) | \lambda > .$$

Now since Q_z is a constant of the motion, $Q_z(\vec{l}',\vec{d}',\infty) = Q_z(\vec{l}',\vec{d}',0) = Q_z(\vec{l}',\vec{d}')$. So the cross section for an Ising system can be written as

$$\frac{d^2\sigma}{d\,\Omega\,dE} = \left(\frac{\gamma e^2}{m_e c^2}\right) \frac{|\vec{K}_f|}{|\vec{K}_i|} e^{-2W(\vec{K})} (1 - k_z^2) \sum_{\vec{l}',\vec{d}'}' \sum_{\vec{l},\vec{d}}' e^{-i\vec{K}\cdot(\vec{l}'+\vec{d}')} \times \tag{48}$$

$$\times\, e^{i\vec{K}\cdot(\vec{l}+\vec{d})} \times \sum_{\lambda}' P_\lambda < \lambda | Q_z^\dagger(\vec{l}',\vec{d}')\, Q_z(\vec{l},\vec{d}) | \lambda > \delta(\omega)$$

where closure has been used to perform the sum of final states λ', and the integral over t has also been performed to give $\delta(\omega)$.

Now for $FeCO_3$, $Q_z(\vec{l},\vec{d})$ is the same for every site $\vec{l}+\vec{d}$ except for a sign change along the z axis. This result follows from the fact that the magnetic moment density is the same at every site to within a sign change along z and a rotation about the z axis. The effect of the rotation will be ignored for now and justified later on the basis of the experimentally measured form factor. Under these circumstances, $Q_z(\vec{l},\vec{d})$ can be expressed as

$$Q_z(\vec{l},\vec{d}) = \sigma(\vec{l},\vec{d})\left| - \frac{1}{2\mu_\beta} \int d\vec{r}\ e^{i\vec{K}\cdot\vec{r}}\ M_z(\vec{r})\right| \tag{49}$$

where $\sigma(\vec{l},\vec{d}) = \pm 1$. The magnetic electron form factor is defined by

$$F(\vec{K}) \equiv - \frac{1}{2\mu_\beta} \int d\vec{r}\ e^{-i\vec{K}\cdot\vec{r}}\ M_z(\vec{r}) \ . \tag{50}$$

Define

$$< O > \equiv \sum_i{}' P_i < i|O|i > \tag{51}$$

and rewrite the cross section as

$$\frac{d^2\sigma}{d\,\Omega\,dE} = \left(\frac{\gamma e^2}{m_e c^2}\right) \frac{|\vec{K}_f|}{|\vec{K}_i|} (1 - k_z^2)\ e^{-2W(\vec{K})}\ |F(\vec{K})|^2 \times \tag{52}$$

$$\times \sum_{\vec{l}',\vec{d}'}{}' \sum_{\vec{l},\vec{d}}{}' e^{-\vec{K}\cdot(\vec{l}'+\vec{d}')}\ e^{\vec{K}\cdot(\vec{l}+\vec{d})} < \sigma(\vec{l}',\vec{d}')\sigma(\vec{l},\vec{d}) > \delta(\omega) \ .$$

The cross section can now be separated into a long range order part and a short range order part by using the identity

$$< \sigma(\vec{l}',\vec{d}')\sigma(\vec{l},\vec{d}) > = < \sigma(\vec{l}',\vec{d}') > < \sigma(\vec{l},\vec{d}) > \tag{53}$$

$$+ [< \sigma(\vec{l}',\vec{d}')\sigma(\vec{l},\vec{d}) > - < \sigma(\vec{l}',\vec{d}') > < \sigma(\vec{l},\vec{d}) >] .$$

The Cross Section for Magnetic Bragg Scattering

When (53) is substituted into (52), the first term of (53) gives the Bragg cross section. This cross section is

$$\frac{d\sigma}{d\Omega} = \left(\frac{\gamma e^2}{m_e c^2}\right) (1 - k_z^2)\, e^{-2W(\vec{K})}\, |F(\vec{K})|^2 \times \tag{54}$$

$$\times \sum_{\vec{l}',\vec{d}}{}' e^{-i\vec{K}\cdot(\vec{l}'+\vec{d}')} < \sigma(\vec{l}'+\vec{d}') > \sum_{\vec{l},\vec{d}}{}' e^{i\vec{K}\cdot(\vec{l}+\vec{d})} < \sigma(\vec{l}+\vec{d}) >$$

where the integral on E has been performed. Now the definition

$$f(\vec{K}) \equiv \sum_{\vec{d}}{}' e^{i\vec{K}\cdot\vec{d}} < \sigma(\vec{l},\vec{d}) > \tag{55}$$

can be made since $< \sigma(\vec{l},\vec{d}) >$ depends only on $\vec{d}$. Equation (55) defines the magnetic structure factor. Further, it can be shown that[36]

$$\sum_{\vec{l}'}{}' \sum_{\vec{l}}{}' e^{-i\vec{K}\cdot(\vec{l}'-\vec{l})} = \frac{N(2\pi)^3}{v_o} \sum_{\vec{\tau}} \delta(\vec{K} - \vec{\tau}) . \tag{56}$$

Substitution of (55) and (56) into (54) gives

$$\frac{d\sigma}{d\Omega} = \left[\frac{N(2\pi)^3 \gamma e^2}{v_o m_e c^2}\right] e^{-2W(\vec{K})} (1 - k_z^2)|F(\vec{K})|^2 |f(\vec{K})|^2 \sum_{\vec{\tau}}' \delta(\vec{K} - \vec{\tau}) < \sigma >^2. \quad (57)$$

This last form will be folded with the resolution function later to give the expression for the integrated intensity of a Bragg magnetic peak.

The Cross Section for Short Range Order

The bracketed term in (53) gives the short range order scattering. The cross section is

$$\frac{d\sigma^2}{d\Omega\, dE} = \left(\frac{\gamma e^2}{m_e c^2}\right) (1 - k_z^2)\, e^{-2W(\vec{K})}\, |F(\vec{K})|^2\, \delta(\omega) \times \quad (58)$$

$$\times \sum_{\vec{I}',\vec{d}}' \sum_{\vec{I},\vec{d}}' e^{-i\vec{K}\cdot(\vec{I}'+\vec{d}')} e^{i\vec{K}\cdot(\vec{I}+\vec{d})} [< \sigma(\vec{I}',\vec{d}')\sigma(\vec{I},\vec{d}) >$$

$$- < \sigma(\vec{I}',\vec{d}') > < \sigma(\vec{I},\vec{d}) >] .$$

It is convenient to delay performing the integration on E until this cross section is folded with the resolution function. The expectation values within the brackets is sometimes written as $< \delta\sigma(\vec{I}',\vec{d}')\delta\sigma(\vec{I},\vec{d}) >$ with

$$\delta\sigma(\vec{I},\vec{d}) \equiv \sigma(\vec{I},\vec{d}) - < \sigma(\vec{I},\vec{d}) > . \quad (59)$$

The cross section (58) can be expressed in terms of the wavevector dependent susceptibility which is defined by

$$\chi(\vec{K}) \equiv \sum_{\vec{r}}' e^{i\vec{K}\cdot\vec{r}} [< s(\vec{r})s(\vec{0}) > - < s(\vec{0}) >^2] . \quad (60)$$

The usual definition of the susceptibility χ (Equation 14) leads to the result

$$\chi = \frac{M^2}{kT} \sum_{\vec{r}}' [< s(\vec{r})s(\vec{0}) > - < s(\vec{0}) >^2] , \tag{61}$$

and it is clear that

$$\lim_{\vec{K} \to 0} \chi(\vec{K}) = \chi \ . \tag{62}$$

All of the diffuse data were taken above the ordering temperature where $< \sigma(\vec{l},\vec{d}) >$ is zero, so the last term in (58) will be dropped for the rest of this discussion. Two more facts are needed to reduce the diffuse cross section to a form that will be folded with the triple-axis resolution function. First, every iron site in $FeCO_3$ is an inversion center, and secondly, translational invariance can be assumed for a large crystal. Consequently, (58) can be reduced to

$$\frac{d^2\sigma}{d\,\Omega\,dE} = 2N \left(\frac{\gamma e^2}{m_e c^2}\right) e^{-2W(\vec{K})} \left|F(\vec{K})\right|^2 (1 - k_z^2)\, \delta(\omega) \times \tag{63}$$

$$\times \left\{ 1 + 2 \sum_{\vec{l}+\vec{d}\neq 0}^{*} \cos[\vec{K}\cdot(\vec{l}+\vec{d})] < \sigma(\vec{l},\vec{d})\sigma(\vec{0}) > \right\}$$

where N is the number of unit cells in the crystal and the (*) over the sum means that if $\vec{l}+\vec{d}$ is included in the sum, then $-(\vec{l}+\vec{d})$ will not be included.

The Monte Carlo Technique

The cross sections just developed contain two thermal expectation values, $< \sigma >$ and $< \sigma(r)\sigma(0) >$, that can be calculated using the Monte Carlo technique. The Monte Carlo calculation will first be described, and then an outline of a proof that it produces the desired averages will be presented.

The procedure starts with the development of a finite sized model for the system under study. Parameters for the Ising Hamiltonian are chosen, and a neighbor table is generated. An array must be created to store the spin state of each atom in the model. For a cubic spin 1/2 model that has L atoms on an edge, the spin array would have to have L^3 elements, and each element would have only two allowed values. If N neighbors are included in the Hamiltonian, then the neighbor table contains $N \cdot L^3$ elements.

An initial configuration is now chosen. For $FeCO_3$, the fully ordered antiferromagnetic state is a natural choice. The atom sites of the model are numbered sequentially. A series of model configurations is generated by performing the following operations at each atom site in turn.

1) The energy of the model is calculated for the present configuration and for the configuration with the spin of the atom overturned.

2) The energy difference $\Delta E = E_{present} - E_{over}$ is taken.

3) If the energy difference is positive (the initial configuration was a high energy configuration) the atom is turned over, and the calculation proceeds to the next atom site.

4) If ΔE is negative, $e^{\frac{\Delta E}{kT}}$ is calculated and a random number X between zero and one is generated.

5) If $e^{\frac{\Delta E}{kT}} > X$, the spin is turned over and the calculation proceeds to the next site.

6) If $e^{\frac{\Delta E}{kT}} < X$, the atom is left in its initial state, and the calculation proceeds to the next site.

At the end of each pass through the lattice, property values for the configuration just generated are calculated and stored. The starting configuration for each pass is the configuration generated by the last pass. It should be noted that only those atoms that are exchange coupled to a central atom must be considered in the energy difference calculation. At the end of M passes (where M is on the order of 300) the arithmetic average of the stored property values is taken.

What is the relation between the arithmetic average defined by

$$< F >_A \equiv \frac{1}{M} \sum_{L=1}^{M} F(u_L) \tag{64}$$

and the original thermodynamic average $< F >$? It can be shown that in the limit as M approaches ∞, the two averages are the same. A number of proofs have been given (see for instance Fosdick[37] and references therein). A complete proof will not be given here. Instead, an outline of the major steps will be given and a simple but instructive example will be presented in Appendix A.

The sequence that was just described is a Markov chain that has the following property. In the limit as M approaches ∞, the probability, P_u, of a particular configuration u appearing in the sequence is given by

$$P_u \propto e^{-\frac{Eu}{kT}} . \tag{65}$$

If this probability can be established, then the law of large numbers implies that

$$\underset{M \to \infty}{\text{LIMIT}} \frac{1}{M} \sum_{L=1}^{M} F(u_L) = \frac{\sum_{u}' F(u) e^{-\frac{Eu}{kT}}}{\sum_{u}' e^{-\frac{Eu}{kT}}} . \tag{66}$$

The proof that the probability (65) is correct relies on several definitions. First, define an integer variable t which is called time for convenience. This variable counts the steps in the Monte Carlo or Markov chain. Next, define a column vector $\vec{Y}$ with elements y_u that are the probability of the crystal model being in a particular configuration u at time t. For a spin 1/2 Ising system there are 2^N configurations so Y must have 2^N elements. Define a conditional transition probability matrix P such that, given that the probability vector is $\vec{Y}(t)$ at time t, then

$$y_u(t+1) = \sum_{u'}' P_{uu'} y_{u'}(t) . \tag{67}$$

These definitions are subject to the conditions,

$$\sum_{u}' y_u = 1; \; y_u \geq 0; \; \sum_{u} P_{uu'} = 1; \; P_{uu'} \geq 0 . \tag{68}$$

Examples of the vector $\vec{Y}$ are found in the example in Appendix A, and the transition matrix P is actually constructed for the example system. If the Monte Carlo process is started with the model in a particular

configuration u at time zero ($\vec{Y}[0]$ has a one for configuration u and zeros elsewhere), then the probability vector at time M is given by

$$\vec{Y}(M) = [P][P]. \; . \; .[P]\,\vec{Y}(0) \tag{69}$$

$$= [P]^{M}\vec{Y}(0) .$$

The elements of the product matrix $[P]^{M}$ are designated $P_{uu'}(M)$.

With these definitions, the major steps of the proof are as follows.

1) For some t, $P_{uu'}(t) > 0$ for all u,u'.

2) If (1) is true, then $\lim_{t\to\infty} \vec{Y}(t) \equiv \vec{Y}_L$ exists and is unique.

3) $\vec{Y}_E$ with elements

$$y_e(u) = e^{-\frac{Eu}{kT}} \Big/ \sum_{u'} e^{-\frac{Eu'}{kT}} \tag{70}$$

is an eigenvector of P with eigenvalue one.

4) If 2) and 3) are true, then

$$\vec{Y}_L = \vec{Y}_E .$$

5) All the other eigenvalues of P have modulus less than one.

This concludes the outline of the proof. All of these steps are illustrated for the example in Appendix A. It has been shown that, regardless of the chosen initial state, a sequence is generated in which the probability of configuration u appearing is given by $e^{-\frac{Eu}{kT}}$. But this is just the probability that was initially postulated in (65).

CHAPTER III

THE EXPERIMENT

The $FeCO_3$ Samples

Iron carbonate has a rhombohedral unit cell with symmetry properties of the space group $R\bar{3}_C$.[38] The unit cell contains two chemical formula units and is shown in Figure 3. This insulator undergoes a transition from a paramagnetic to an antiferromagnetic state at around 40 K.[1] The temperature at which this transition begins is called the ordering point or Néel temperature, T_N. In the fully ordered state, the magnetic moment vectors of the Fe^{2+} ions are parallel to the z axis (body diagonal of the unit cell) of Figure 3. The ions lie in sheets perpendicular to the z axis, and the magnetic moment of ions in alternating sheets point in opposite directions along the z axis.

It is difficult to grow single crystals of $FeCO_3$. The largest crystals grown so far are suitable only for powder experiments. The samples used in this study were natural single crystals from a Quebec deposit. The mosaic spreads of a number of samples were measured before the two samples for the study were selected. The smaller sample was ground into a sphere that was 0.21 inches in diameter for the Bragg experiments. The larger sample was ground until it was roughly spherical in shape with an average diameter of 0.5 inches. This sample was used in the diffuse work.

A spectrographic analysis was made on a chip from the Bragg sample.[39]

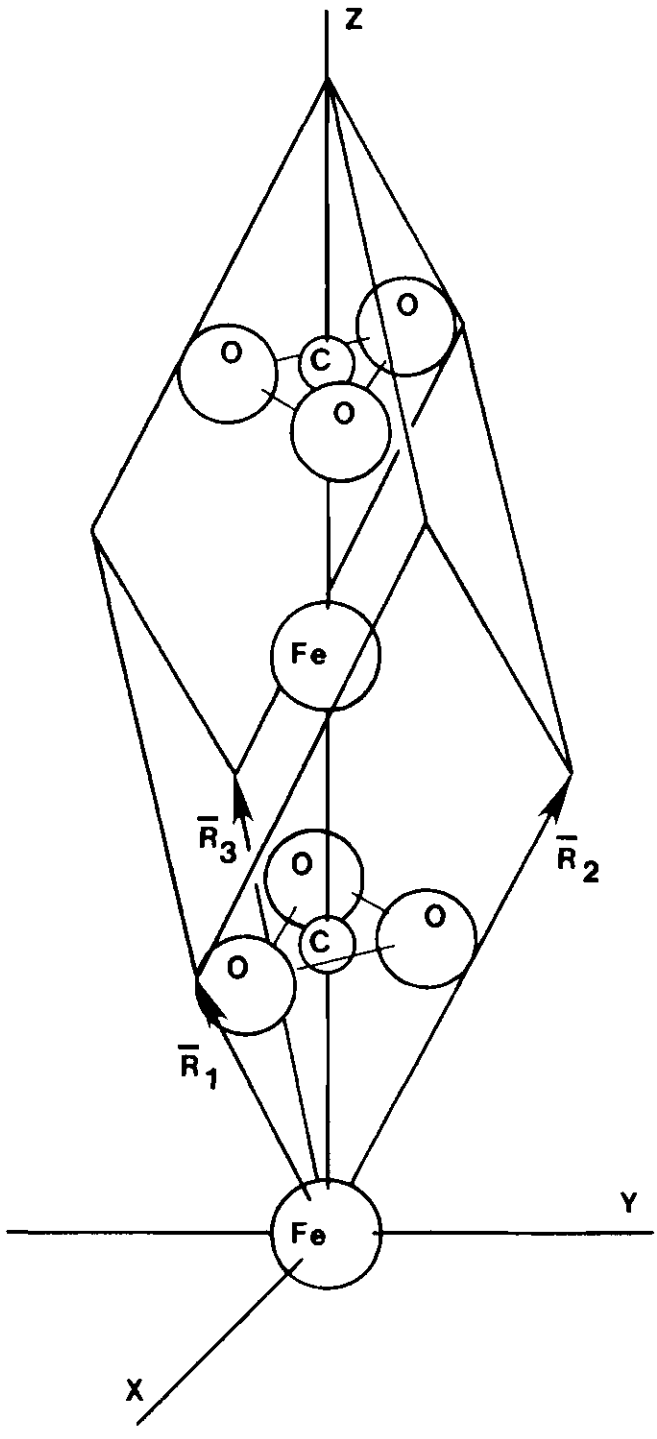

Figure 3. Unit Cell of $FeCO_3$

The major cation impurities were found to be magnesium and manganese. Magnesium was present in a concentration of two percent and manganese in a concentration of three percent by weight. These by-weight concentrations are equivalent to eight percent of the cation sites for magnesium and six percent for manganese. The effect of the impurity ions on the measured property values will be discussed in detail in the Results and Discussion Section.

The Neutron Diffractometer

The sublattice magnetization was determined by measurements of the Bragg diffraction intensity obtained with the use of a conventional double-axis diffractometer arrangement. Spin correlations above the Néel temperature were investigated through measurements of magnetic diffuse scattering. The diffuse scattering data were collected using a triple-axis diffractometer arrangement. In the diffuse experiment, the third axis, the energy analyzing axis was set to receive only those neutrons scattered from the sample with zero energy transfer. In both experiments a PDP-8 processor was used to control the diffractometer axes. The details of the computer control system are discussed elsewhere.[40] The triple-axis configuration is shown in Figure 4. In the Bragg arrangement, the analyzer crystal is replaced by the counter.

In both experiments, a fixed crystal was used to scatter a monochromatic neutron beam onto the sample. No attempt was made to provide collimation between the reactor source and the monochromating crystal. Soller slit collimators were used between the monochromating crystal and sample. In the measurements of Bragg intensities, the detector was placed

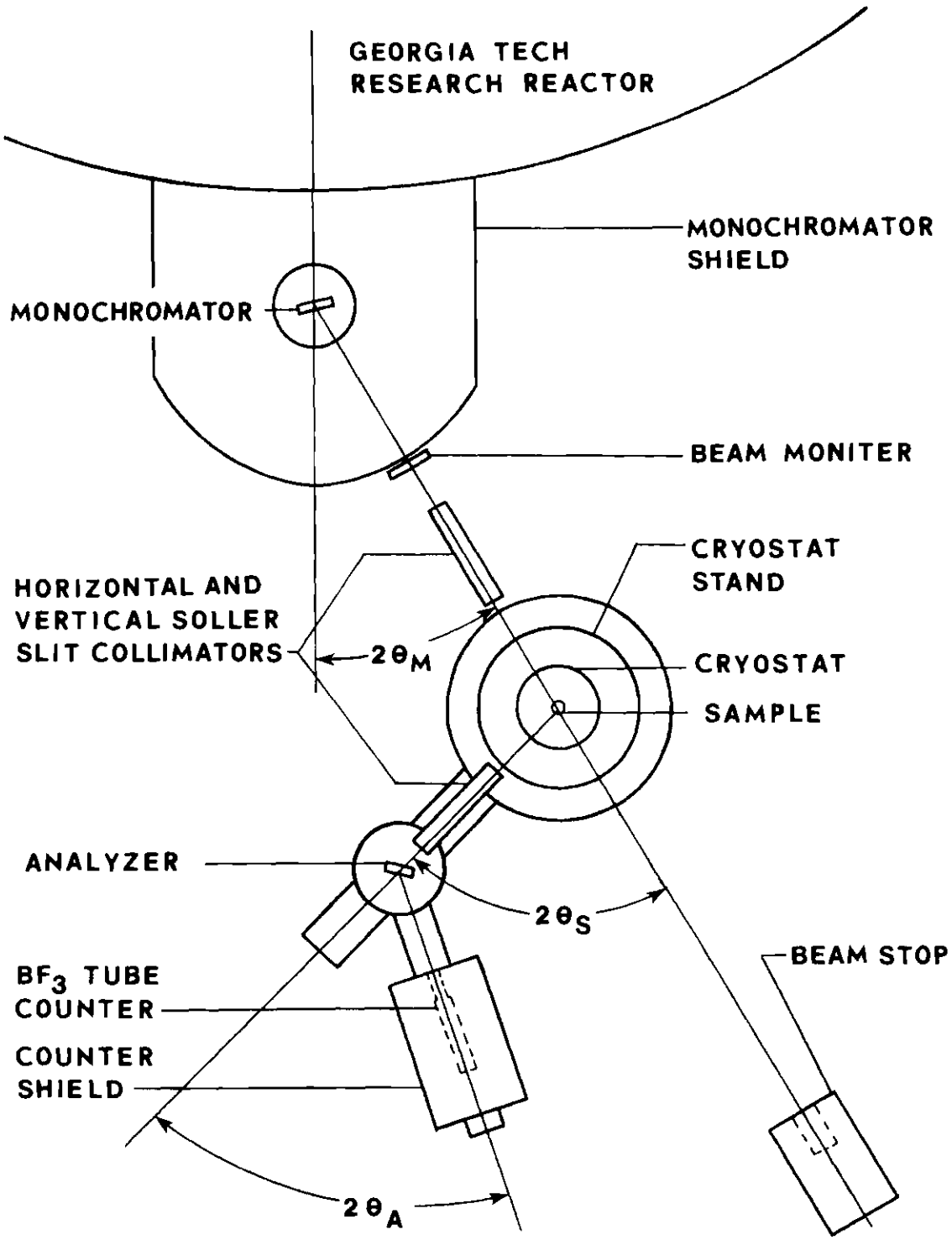

Figure 4. Triple Axis Diffractometer

close enough to the sample to receive all of the Bragg scattered neutrons. In the diffuse scattering work, both horizontal and vertical collimation was provided between the monochromator and the sample and between the sample and the analyzer. In this experiment, definition of the neutron direction and energy was necessary in order to minimize any inelastic scattering in the measured intensity. The analyzer was used to discriminate against inelastic scattering.

Both samples were mounted in a cryostat (see next section) and oriented at room temperature. The center of the samples was placed about 3/16 of an inch below the center of the neutron beam to allow for thermal contraction of the cryostat as it was cooled down. Sample orientation was checked again at liquid helium temperature, and these checks indicated that no significant shifts in sample orientation took place upon cooling except the raising of the sample to the center of the beam. Throughout both Bragg and diffuse experiments, nuclear Bragg peaks were monitored to check sample condition and orientation. These further checks revealed no additional changes in sample orientation.

The Temperature Control Equipment

Figure 5 shows the cryostat that was used to hold the samples during the experiments. The sample was mounted inside a thin walled aluminum container that was attached to a goniometer. The goniometer was in turn attached to a copper block on the end of the "cold finger" of a Janis D. T. Vari-Temp cold finger cryostat. The sample was glued to a short cadmium post inside the sample shield with General Electric 7031 varnish, and all of the metal joints were given a light coating of Apiezon J oil to improve

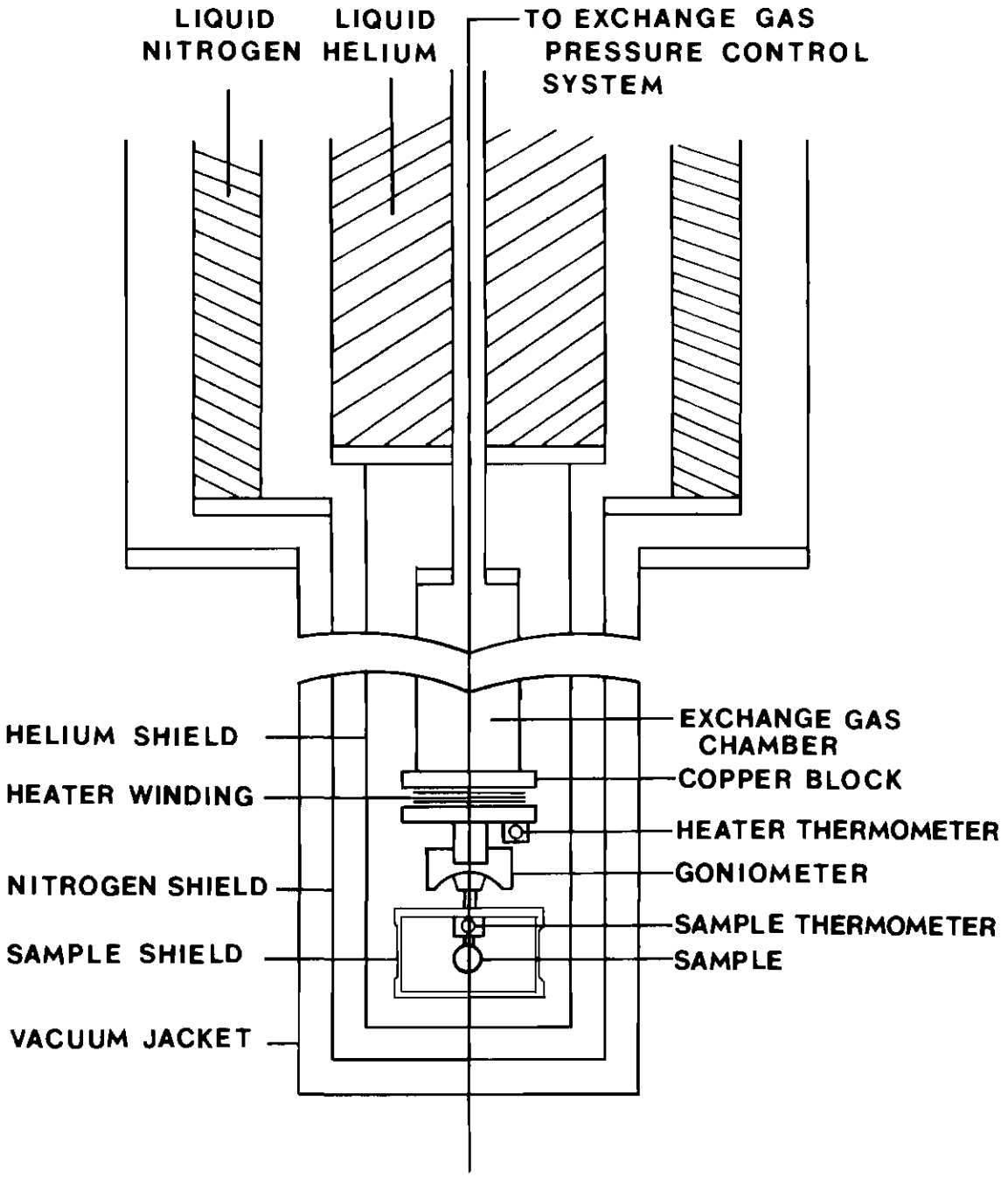

Figure 5. Helium Cryostat

thermal conductivity.

The temperature of the sample was controlled in the following manner. Helium gas was admitted to the exchange gas chamber. This chamber is in contact with the copper block that the goniometer is mounted on and also with the liquid helium reservoir. If no heat was supplied to the copper block, the block and the sample would reach a temperature of around 5 K. To raise the sample temperature above this point, heat was supplied to the copper block through a 7 mil manganun copper wire heater winding. The temperature of the copper block was monitored by measuring the resistance of an Allen Bradley carbon resistor. The resistance was determined by running a constant current through the resistor and measuring the voltage drop across it. This voltage was the input to a Leeds and Northrup temperature control unit that supplied the current to the heater winding.

The sample temperature was monitored using an independent system. A CryoCal germanium resistor, Model CR 2500H, was mounted inside the sample shield next to the sample mount. The resistor was calibrated by CryoCal to an accuracy of 0.04 K throughout the entire temperature range of the experiment. The same technique was used to measure the resistance of the germanium resistor that was used in the temperature control system. A constant current was supplied to the resistor by a Keithley Model 261 Picoampere source. The voltage drop across the resistor was measured using a Leeds and Northrup Model 8686 precision millivolt potentiometer. With this arrangement, the sample temperature could be determined to within 0.1 K. During the Bragg experiments, measurements were repeated until both the sample temperature and the integrated Bragg intensity showed no further drift in their values.

The Resolution Function

The neutrons that enter the counter during a diffraction experiment depend upon the characteristics of the diffractometer and the sample. The diffractometer can be described in terms of the transmission functions of the collimators and crystals that are used. These transmission functions can be folded together to give the resolution function of the diffractometer, which is the probability distribution of neutrons in wavevector-energy space. Cooper and Nathans[41,42] have treated the resolution function problem assuming that the transmission functions of the collimators and mosaic spreads of the crystals are all Gaussian. They conclude that the resolution function has surfaces of constant scattering probability that are four-dimensional ellipsoids in energy-momentum space.

Figure 6 shows the wavevectors associated with the double axis and triple axis set ups. In this figure, the α's represent the horizontal divergences of the collimators and crystals (assumed Gaussian), and the β's represent the vertical divergences of the collimators and crystals (again assumed Gaussian). Figure 7 is a vector diagram of a typical triple axis arrangement in wavevector space. This contains the vectors that are used in the definition of the resolution function. In this figure

$\vec{K}_o$ = the direction of the most probable $\vec{K}$ vector onto the monochromator (the center of the assumed Gaussian distribution),

$\vec{K}_i$ = the direction of the most probable $\vec{K}$ vector onto the sample,

$\vec{K}_f$ = the direction of the most probable $\vec{K}$ vector through the post sample collimator,

$$\omega = \frac{\hbar}{2m} |K_f|^2 - \frac{\hbar}{2m} |K_i|^2 . \qquad (71)$$

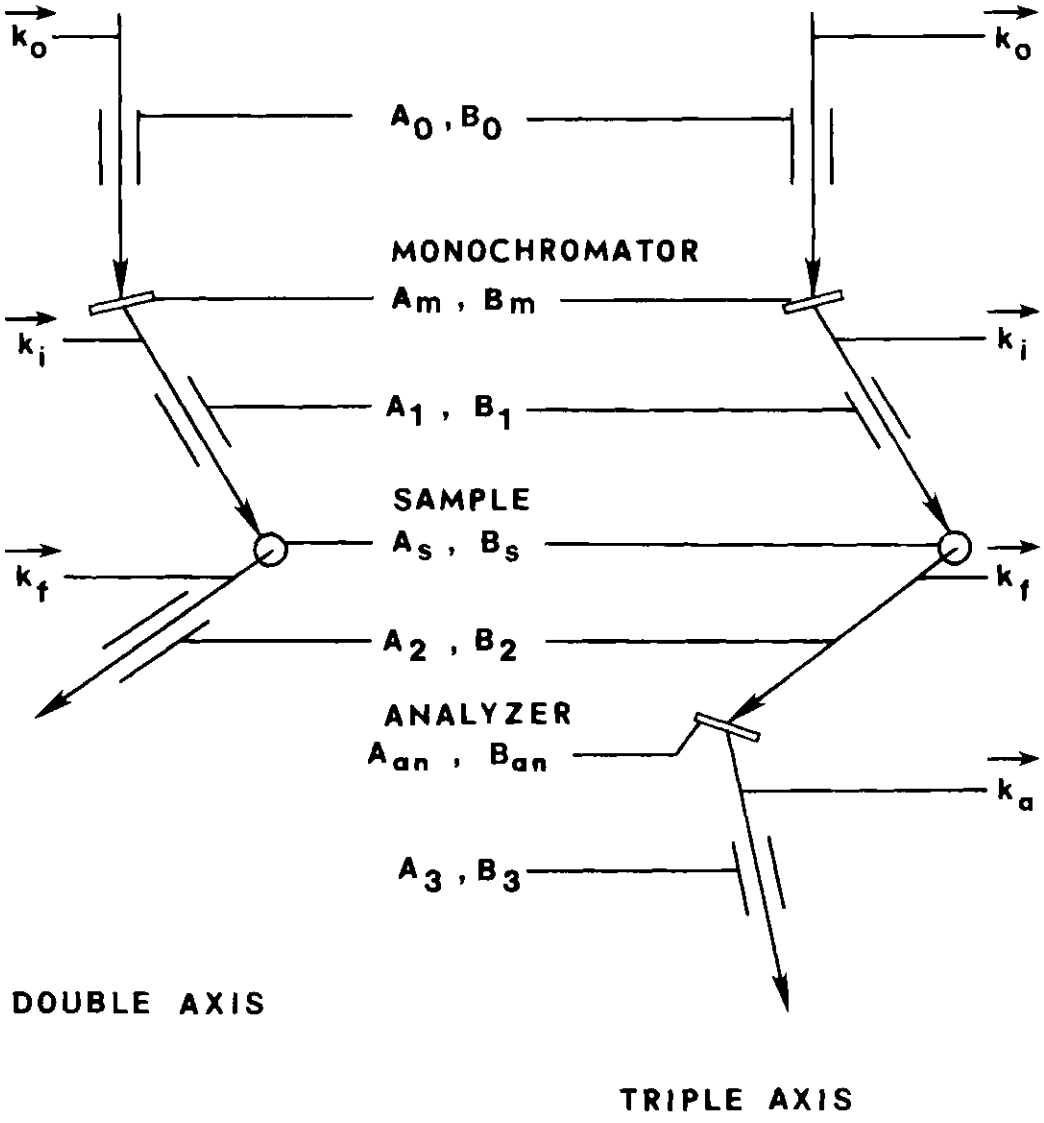

Figure 6. Resolution Function Parameters

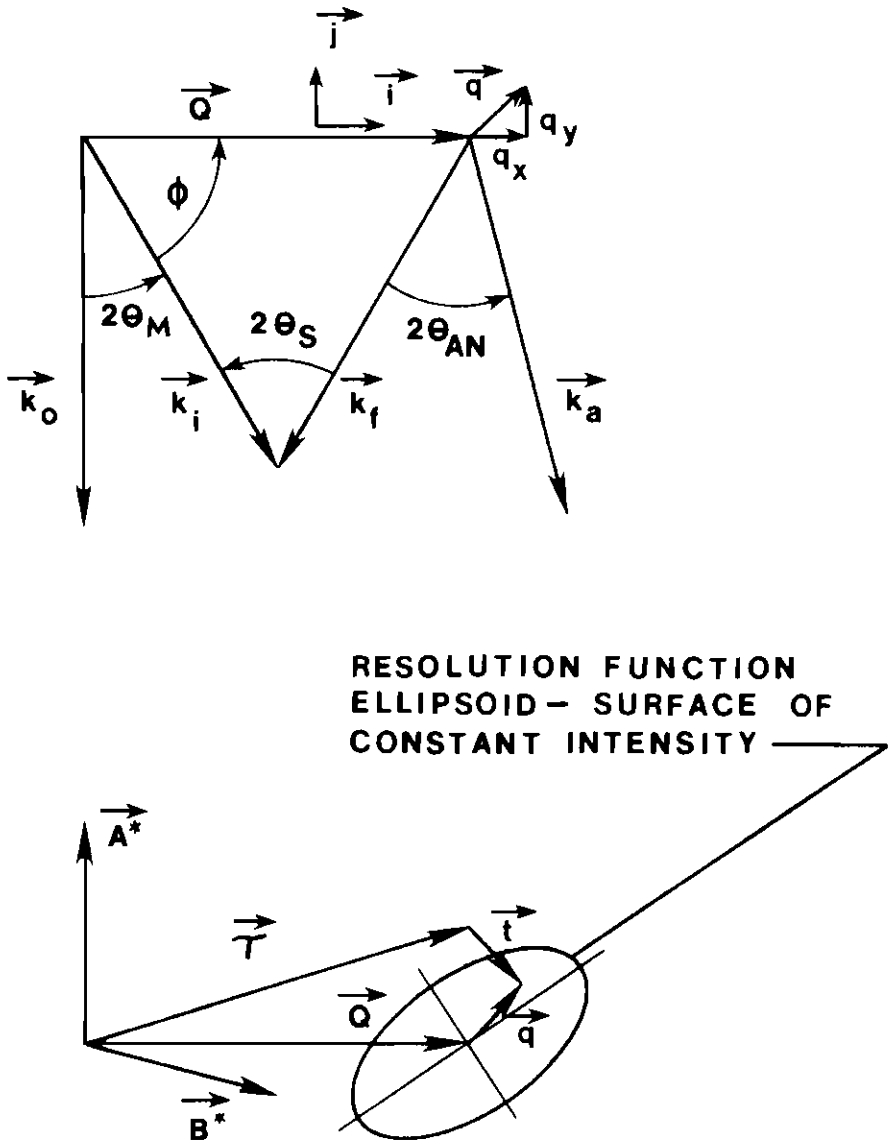

Figure 7. Resolution Function Vectors

The assumption is made that the monochromator, analyzer, and collimators are properly aligned so that the center lines of the collimators lie along the theta-2 theta directions of the crystals for Bragg scattering.

The vector $\vec{Q}$ is now defined by

$$\vec{Q} = \vec{K}_i - \vec{K}_f \ . \tag{72}$$

The vectors q_x, q_y, and q_z are the displacements away from $\vec{Q}$ in the directions $\vec{i}$, $\vec{j}$, and $\vec{k}$ as indicated in the figure. With these definitions, the double axis resolution function can be written in the form

$$R(\vec{Q},\vec{q}) \propto e^{-[XXq_x^2 + YYq_y^2 + XYq_xq_y + ZZq_z^2]} \tag{73}$$

and the resolution for a triple axis set up has the form

$$R(\vec{Q},\vec{q},\Delta\omega) \propto e^{-[XXq_x^2 + YYq_y^2 + EE\Delta\omega^2 + XYq_xq_y + EXq_x\Delta\omega + EYq_y\Delta\omega + ZZq_z^2]}. \tag{74}$$

The expressions for the constants XX, YY, etc. are given in Appendix B. These constants are different for the two different cases. Notice that $\Delta\omega$ is not the ω defined by Equation (71). The $\Delta\omega$ in the resolution function is a small deviation away from this mean energy difference value.

These resolution functions depend upon $\vec{Q}$ through the $\vec{K}_i$ and $\vec{K}_f$ dependence of the constants as well as the direction of the unit vectors $\vec{i}$, $\vec{j}$, and $\vec{k}$. The differential cross section can be written in the form

$$\sigma(\vec{\tau} + \vec{t},\ \omega + \Delta\omega) = \sigma(\vec{Q} + \vec{q},\ \omega + \Delta\omega) \tag{75}$$

since $\vec{\tau} + \vec{t} = \vec{Q} + \vec{q}$ (see second diagram in Figure 7). Therefore, the intensity into the counter is given by

$$I(\vec{Q},\vec{\tau}) = \int d\vec{q}\ d\Delta\omega R(\vec{Q},\vec{q},\Delta\omega)\sigma(\vec{Q} + \vec{q},\ \omega + \Delta\omega)\ . \tag{76}$$

The Folding Procedure

Consider the cross section for Bragg scattering as measured with a double axis arrangement. Recall

$$\frac{d\sigma}{d\Omega} = \frac{N(2\pi)^3}{\nu_o}\frac{\gamma e^2}{m_e c^2} e^{-2W(\vec{K})}(1 - k_z^2)\left|\mathbf{F}(\vec{K})\right|^2\left|f(\vec{K})\right|^2 \sum_{\vec{\tau}} \delta(\vec{K} - \vec{\tau}) < \sigma >^2\ . \tag{77}$$

A single crystal sample and the diffractometer are set so that the vector $\vec{Q}$ coincides with a particular reciprocal lattice vector of the sample $\vec{\tau}$. A theta-2theta scan is then made (a scan in the $\vec{i}$ direction) to measure the integrated intensity for the Bragg peak. To a good approximation, $e^{-2W(\vec{K})}(1 - k_z^2)\left|F(\vec{K})\right|^2\left|f(\vec{K})\right|^2$ is a constant for such a scan, and we can write

$$\frac{d\sigma}{d\Omega} = C \sum_{\vec{\tau}} \delta(\vec{K} - \vec{\tau}) < \sigma >^2\ . \tag{78}$$

The integrated intensity is given by

$$I_{MAG}^{BRAGG} = \sum_{Q_x} \int d\vec{q}\ C' \sum_{\vec{\tau}} \delta(\vec{K} - \vec{\tau}) < \sigma >^2 e^{-[XXq_x^2 + YYq_y^2 + XYq_xq_y + ZZq_z^2]} \tag{79}$$

$$= <\sigma>^2 C' \sum_{Q_x}' e^{-[XX(Q_x-\tau_x)^2 + YY(Q_y-\tau_y)^2 + XY(Q_x-\tau_x)(Q_y-\tau_y) + ZZ\tau_z^2]} .$$

For this experiment, the scan along $\vec{Q}$ is performed to make the resultant measured intensity insensitive to the difference $(Q_x-\tau_x)$. The collimation between the sample and the counter is relaxed and the vertical collimation is also relaxed. This relaxation makes the resolution function very insensitive to the difference $Q_y-\tau_y$ and τ_z. Under these circumstances, one can write that, as a function of temperature $I_{MAG}^{BRAGG}(T) = C'' <\sigma>^2$.

In the Bragg case, the collimation is chosen to make the data relatively insensitive to the exact crystal orientation. In the quasi-elastic case, just the opposite is true. The collimation is controlled carefully throughout the experiment so that the diffraction cross section can be measured as a function of $\vec{K}_i-\vec{K}_f$. For this case, the cross section is given by

$$\frac{d^2\sigma}{d\Omega\, dE} = 2N \frac{\gamma e^2}{m_e c^2} (1 - k_z)^2 e^{-2W(\vec{K})} |F(\vec{K})|^2 \delta(\omega) \times \tag{80}$$

$$\times \left\{ 1 + 2 \sum_{\vec{l},\vec{d}}^{*} \cos[\vec{K}\cdot(\vec{l} + \vec{d})] <\sigma(\vec{l},\vec{d})\sigma(\vec{0})> \right\} .$$

When this function is folded in with the resolution function and an integral on ω is performed, one gets that

$$I(\Omega) = 2N \frac{\gamma e^2}{m_e c^2} C'' \int d\vec{q}\, d\Delta\omega (1 - k_z^2) e^{-2W(\vec{K})} |F(\vec{K})|^2 \delta(\omega) \times \tag{81}$$

$$\times \left\{ 1 + 2 \sum_{\vec{I},\vec{d}}^{*} \cos[\vec{K}\cdot(\vec{I} + \vec{d})] < \sigma(\vec{I},\vec{d})\sigma(\vec{0}) > \right\} \times$$

$$\times e^{-[XXq_x^2 + YYq_y^2 + EE\Delta\omega^2 + XYq_xq_y + EXq_x\Delta\omega + EYq_y\Delta\omega + ZZq_z^2]}$$

$$= C''' \int d\vec{q} (1 - k_z^2) e^{-2W(\vec{K})} |F(\vec{K})|^2 \times$$

$$\times \left\{ 1 + 2 \sum_{\vec{I},\vec{d}}^{*} \cos[\vec{K}\cdot(\vec{I} + \vec{d})] < \sigma(\vec{I},\vec{d})\sigma(\vec{0}) > \right\} \times$$

$$\times e^{-[XXq_x^2 + YYq_y^2 + XYq_xq_y + ZZq_z^2]} .$$

Before proceeding further, it is necessary to briefly describe the magnetic Brillouin zone of $FeCO_3$. A careful examination of the expression for $I(\Omega)$ just given reveals that there is some ambiguity in the definition of the co-ordinate systems used. In this expression, k_z is the component of $\vec{K}$ (in this case $\vec{Q} + \vec{q}$) along the spin direction, and q_z is the component of $\vec{q}$ perpendicular to the scattering plane. After the description of the Brillouin zone, the expression for $I(\Omega)$ will be rewritten in a consistent form.

The Magnetic Brillouin Zone

Figure 8 shows the magnetic Brillouin zone. In this figure, the z axis is the spin direction and also the axis of three fold rotational

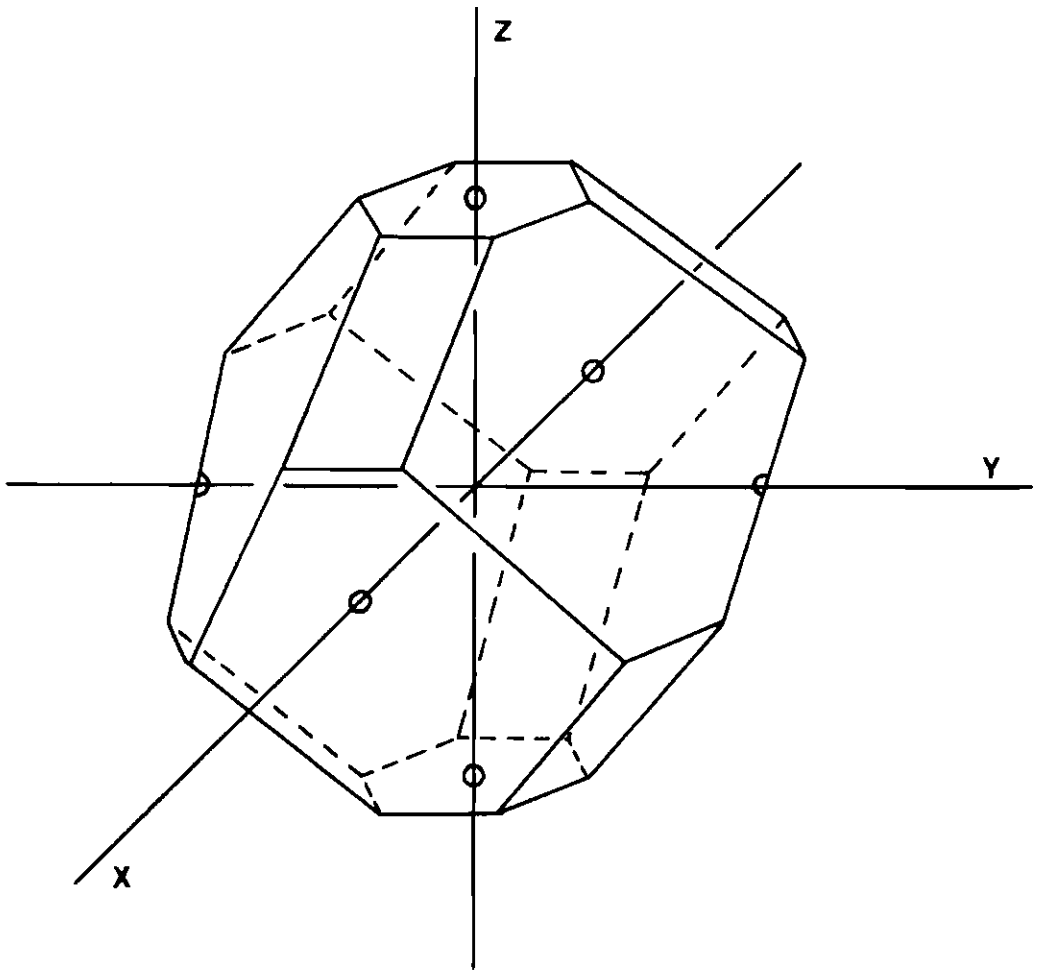

Figure 8. Magnetic Brillouin Zone of $FeCO_3$

symmetry. The y axis is an axis of two fold rotational symmetry (one of three), and the x-z plane is a mirror plane (also one of three). The diffuse data were taken in the x-z plane of Figure 8. This plane contains the spin direction and one of the three equivalent reciprocal lattice axes.

Figure 9 shows a section of several Brillouin zones in this plane. Notice that no magnetic Brillouin zone is centered around the origin of reciprocal lattice space. The two zones in Figure 9 are the zones in which the diffuse magnetic data were taken. These zones were chosen because they allow one to examine the anisotropy that should exist because the spins are locked along the z direction and because they contain the magnetically active reciprocal lattice points that lie closest to the origin of reciprocal lattice space. It was necessary to stay as close to the origin as possible, because the magnetic form factor $|F(\vec{K})|^2$ is essentially a function of the magnitude of $\vec{K}$ and falls off very rapidly as $|\vec{K}|$ increases.

Figure 10 defines the vectors that can be conveniently used to fold the cross section and resolution function together. The Brillouin zone in this figure is the one centered about the (1 0 0) reciprocal lattice vector. This figure shows a scan along the line SL that makes an angle SA with the (1 0 0) reciprocal lattice vector. The scan started at the tip of the (1 0 0) vector and is proceeding towards the edge of the Brillouin zone. The (1 0 0) vector makes an angle of 14.79° (labeled AN in the figure) with the x axis. The resolution ellipsoid is centered about the tip of the vector $\vec{Q}$, and we want to determine the contribution that the scattering from a small volume of space centered about the point labeled P at the tip of the $\vec{q}$ vector makes to $I(\Omega)$. I_x is a small deviation away

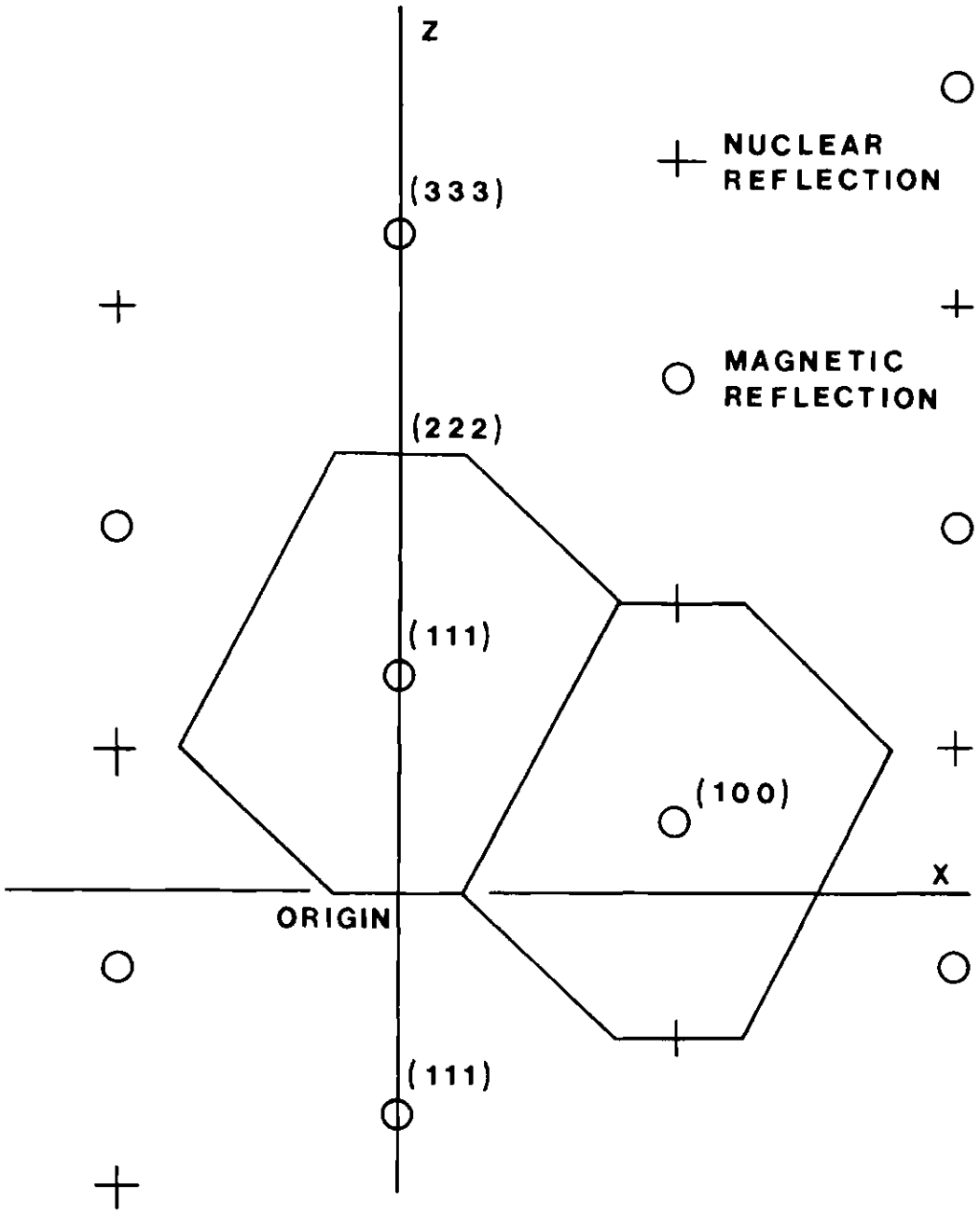

Figure 9. The X-Z Plane of the Brillouin Zone

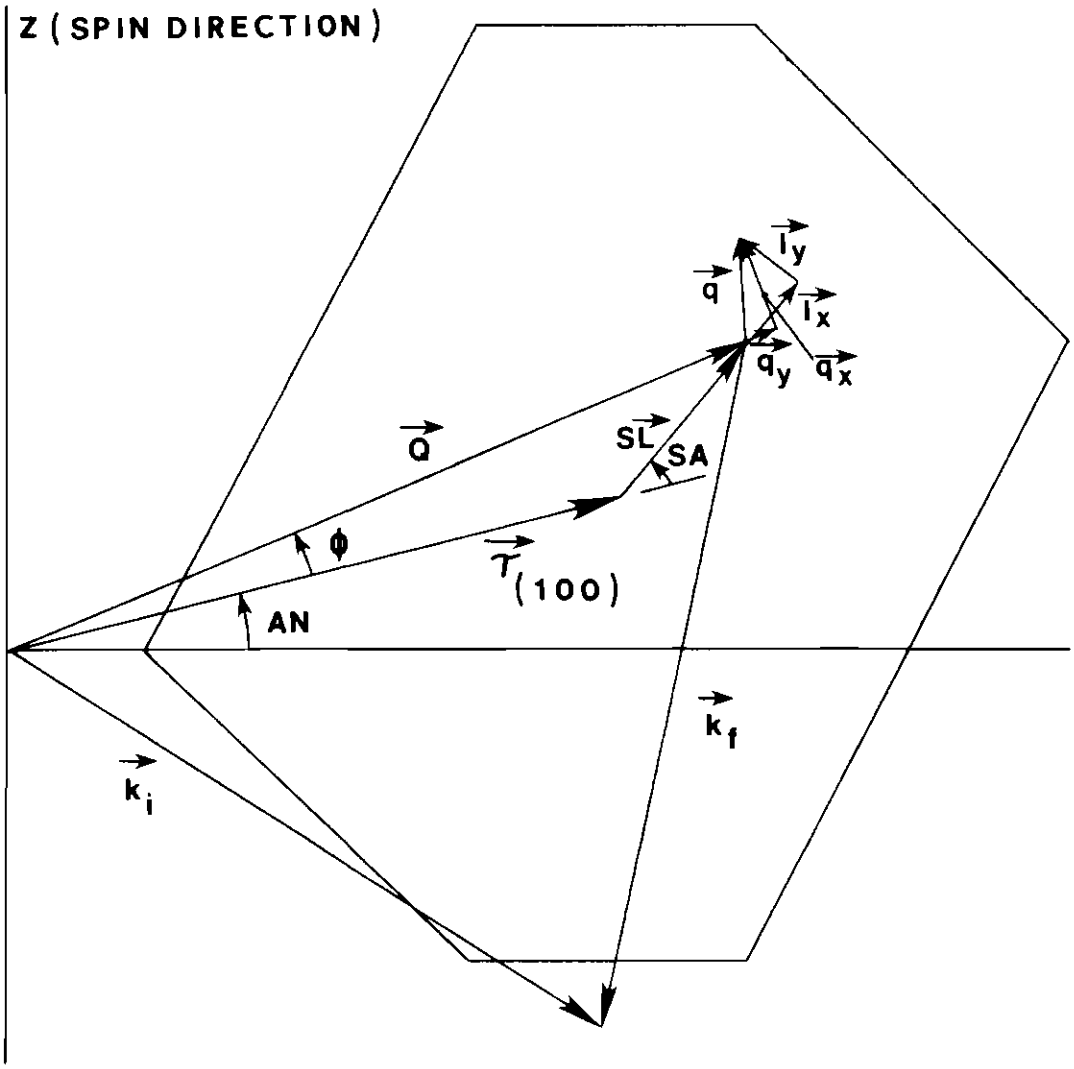

Figure 10. Definition of the Vectors Used in the Folding Procedure

from $\vec{q}$ in the $\vec{SL}$ direction and I_y is a small deviation away from $\vec{q}$ in the direction perpendicular to $\vec{SL}$ as shown in the figure. The relevant expressions are the following:

$$Q_x = \tau \cos(AN) + SL \cos(AN + SA) \tag{82}$$

$$Q_y = \tau \sin(AN) + SL \sin(AN + SA)$$

$$Q_z = 0$$

$$K_x = \tau \cos(AN) + SL \cos(AN + SA) + I_x \cos(AN + SA) - I_y \sin(AN + SA)$$

$$K_y = \tau \sin(AN) + SL \sin(AN + SA) + I_x \sin(AN + SA) + I_y \cos(AN + SA)$$

$$K_z = - I_z$$

$$q_x = I_x[\sin(AN + \emptyset)\sin(AN + SA) + \cos(AN + \emptyset)\cos(AN + SA)]$$

$$+ I_y[\sin(AN + \emptyset)\cos(AN + SA) - \cos(AN + \emptyset)\sin(AN + SA)]$$

$$q_y = I_x[\cos(AN + \emptyset)\sin(AN + SA) - \sin(AN + \emptyset)\cos(AN + SA)]$$

$$+ I_y[\cos(AN + \emptyset)\cos(AN + SA) + \sin(AN + \emptyset)\sin(AN + SA)]$$

$$q_z = I_z$$

The angle $\emptyset$ can be found unambiguously using the following relations:

$$|\vec{Q}|^2 = [\tau + SL\cos(SA)]^2 + [SL\sin(SA)]^2 \tag{83}$$

$$\sin(\emptyset) = SL\sin(SA)/|\vec{Q}|$$

$$\cos(\emptyset) = [\tau + SL\cos(SA)]/|\vec{Q}| \ .$$

Now all of the relevant quantities that are used in the calculation of $I(\Omega)$ are defined in terms of τ, AN, SL, SA, I_x, I_y, and I_z. With these definitions, the contribution from the point P to $I(\Omega)$ can be written as:

$$\Delta I(\Omega) \propto \left[1 - k_z^2(\vec{\tau} + \vec{SL} + \vec{I})\right] e^{-2W(\vec{\tau} + \vec{SL} + \vec{I})} |F(\vec{\tau} + \vec{SL} + \vec{I})|^2 \times \tag{84}$$

$$\times \left\{1 + 2 \sum_{\vec{I}+\vec{d}}^{*} \cos[(\vec{\tau} + \vec{SL} + \vec{I})\cdot(\vec{I} + \vec{d})] < \sigma(\vec{I},\vec{d})\sigma(\vec{0}) > \right\} \times$$

$$\times \ e^{-[XXq_x^2(\vec{I}) + YYq_y^2(\vec{I}) + XYq_x(\vec{I})q_y(\vec{I}) + ZZq_z^2(\vec{I})]} \ .$$

$I(\Omega)$ can now be calculated by performing a finite sum on I_x, I_y, I_z as follows

$$I(\Omega) = C''' \sum_{I_x}' \sum_{I_y}' \sum_{I_z}' \sigma(\vec{\tau} + \vec{SL} + \vec{I})R(\vec{\tau} + \vec{SL} + \vec{I}) \ . \tag{85}$$

The constant C''' depends on the step size chosen for I_x, I_y, and I_z.

The introduction of the I variables may appear to be an unnecessary

complication. But the use of vectors that lie along and perpendicular to the scan direction has this advantage. The cross section can be calculated for a three dimensional array of points along the entire scan direction. These cross section values can then be folded with the resolution function at various points along the scan direction to give $I(\Omega)$. The cross section values need to be calculated only once for the entire scan. If the q_x, q_y, and q_z variables are used instead, then a new array of cross section values must be calculated for each folding, because the q_x, q_y, and q_z vectors change direction as one proceeds along in a fixed scan direction.

CHAPTER IV

RESULTS AND DISCUSSION

Neutron Sublattice Magnetization Results

The integrated intensity of the (3 0 0) magnetic Bragg peak was measured from 6.6 K to 41.2 K. The expression for this integrated intensity has been shown to be proportional to the square of the sublattice magnetization (Equation 57). However, the derivation that leads to this result does not include corrections for critical scattering and extinction that must be applied to the data before an accurate temperature dependence for $< \sigma >$ can be obtained. The correction for critical scattering near T_N will be discussed in the following section. The secondary extinction correction will now be described. After these two corrections are explained, the sublattice magnetization curve determined from the neutron data will be presented.

As a neutron beam passes through a sample, its intensity is diminished by the diffraction that takes place. The first Born approximation assumes that the sample is bathed in a uniform beam. Therefore a correction must be made to the data from Bragg diffraction. Hamilton[43] has developed a method for making extinction corrections based on the sample geometry. However, the correction is very sensitive to sample shape, and it is best to minimize this correction if accurate results are desired.

Fortunately, at the positions for the magnetic Bragg peaks in $FeCO_3$,

all of the nuclear structure factors are zero, and this fact allows a simple estimate of extinction effects in the data to be made. At the Néel temperature, the intensities of the magnetic peaks fall to zero. As the sample temperature is lowered, the intensities should all rise at a rate that is proportional to $<\sigma>^2$. Extinction effects cause the strong Bragg peaks to rise more slowly. For a uniform, spherical sample, an approximate extinction correction of the form

$$I'(h,k,l) = I_o(h,k,l)e^{-\beta I_{cal}(h,k,l)} \tag{86}$$

can be used.[43] Here, $I'(h,k,l)$ is the measured integrated intensity, $I_o(h,k,l)$ is the intensity that would be measured if there were no extinction, and $I_{cal}(h,k,l)$ is the calculated intensity (Equation 57). It should be possible to find a single value for β that can be used in (86) to correct the data for extinction and bring all of the intensity versus temperature curves into coincidence.

Therefore the integrated intensities of three Bragg reflections, the (1 0 0), the (3 0 0), and the (1 4 4), were measured at eight temperatures. The ratio of the intensities of these reflections at 8 K was approximately 60:5:1, respectively. The data from this experiment are found in Table 3 of Appendix C. These data have been corrected for instrumental and sample background scattering.

The reduced intensity, $I_R(T)$, is defined by the ratio

$$I_R(T) \equiv I_{Mag}^{Bragg}(T)/I_{Mag}^{Bragg}(T=0) \tag{87}$$

and the corrected reduced intensity data are plotted in Figure 11 for all three reflections. The size of the statistical error in $I_R(T)$ for the (1 4 4) is indicated by error bars in Figure 12. The errors in the (1 0 0) and (3 0 0) $I_R(T)$ values are smaller than the symbol sizes. As expected, a single smooth curve will not fit all three sets of data. An extinction correction of the form in Equation (86) has been applied to the data in Figure 12. For this plot, a single smooth curve can be drawn that will fall within the error bars of the data. The maximum extinction correction in the (3 0 0) data is approximately two percent. This reflection is still strong enough, however, to allow intensity data with a small statistical error to be gathered in a reasonable period of time. These are the reasons the (3 0 0) reflection was chosen for the rest of the Bragg diffraction work.

In this preliminary experiment, only the temperature control unit was used. The sample temperature was not measured independently, and the temperature values are therefore only approximate. The sample was held at each temperature until there was no change in the measured Bragg integrated intensities. This procedure was used to make sure that all three Bragg intensities were measured at the same temperature.

During the next experiment, the Bragg integrated intensity of the (3 0 0) was measured at 27 temperatures from 6.5 K to 41.3 K. The independent system described in Chapter III was used to measure the sample temperature. Intensity measurements at five temperatures were repeated to check for reproducibility. The repeated measurements were always within statistics. To minimize any systematic errors, the temperatures were not

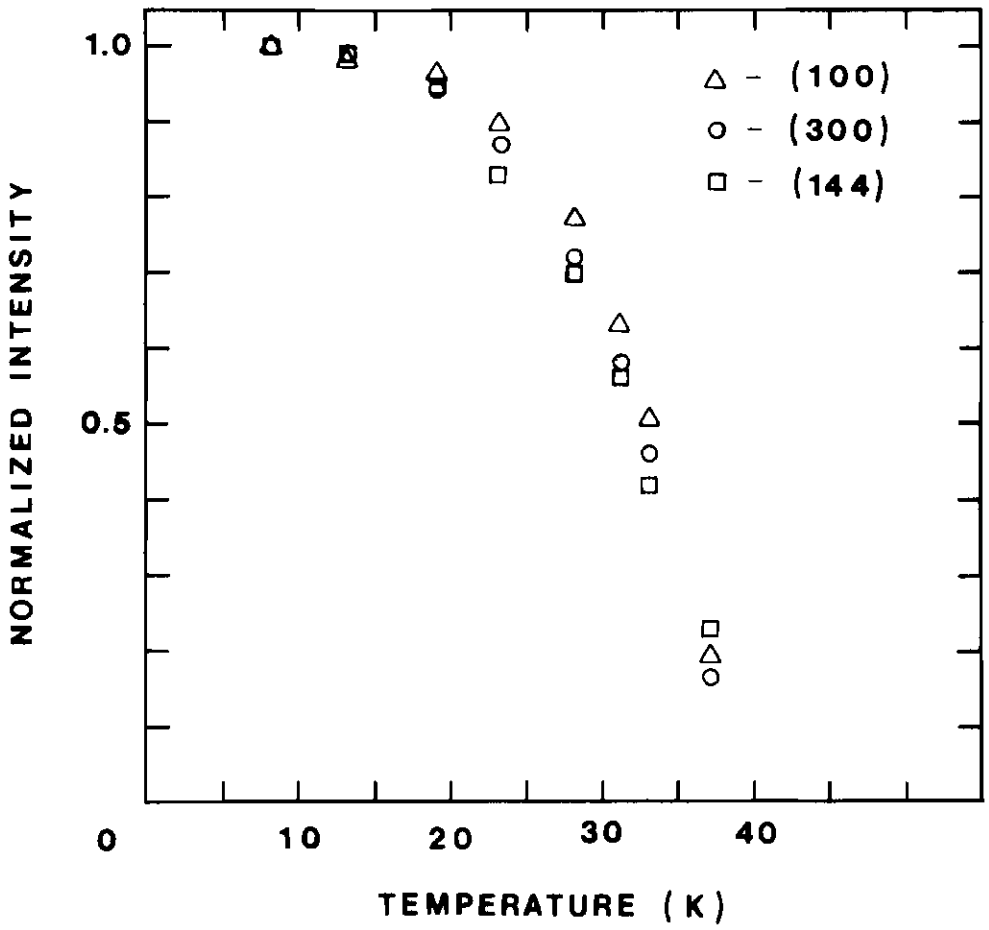

Figure 11. Plot of Neutron Data with no Extinction Correction

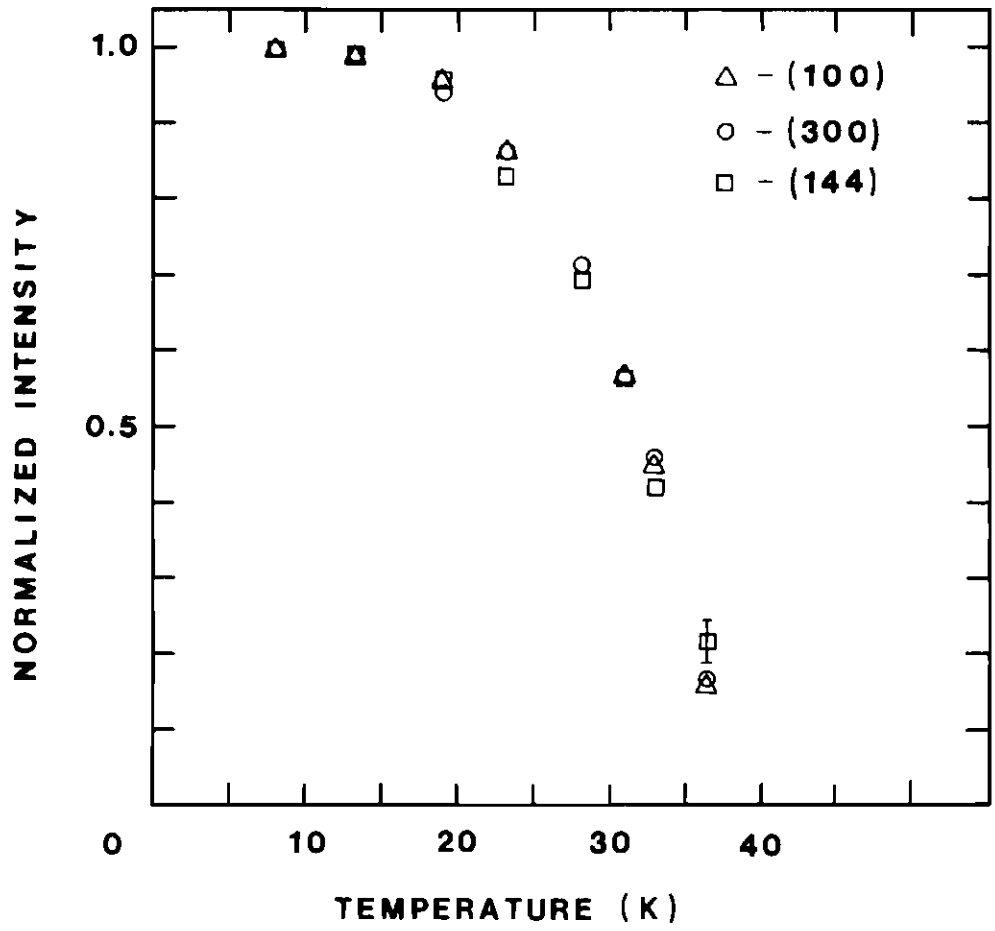

Figure 12. Plot of Neutron Data with Extinction Correction

taken sequentially. Each day, data were gathered at temperatures throughout the temperature range.

The results from this experiment are tabulated in Table 4, Appendix C. The order in which the intensities were measured is indicated in the table. The data in the table have again been corrected for instrumental and sample background scattering. The extinction correction just described has also been applied.

An estimate of the critical scattering in the data near T_N was based on the Mössbauer results of Koon.[11] His results indicate that, near T_N, the reduced sublattice magnetization defined by

$$< \sigma(T) >_R \equiv < \sigma(T) > / < \sigma(T=0) > \tag{88}$$

is accurately described by the power law

$$< \sigma(T) >_R = C(1 - T/T_N)^{0.312}. \tag{89}$$

Since $I_{Mag}^{Bragg}(T)$ has been shown to be proportional to $< \sigma(T) >^2$, Equation (89) can be manipulated into the form

$$\left[I_{Mag}^{Bragg}(T) \right]^{1/0.624} = A(1 - T/T_N) . \tag{90}$$

This expression is linear in the temperature T, and clearly goes to zero at $T = T_N$.

The graph in Figure 13 is a plot of the corrected Bragg intensities

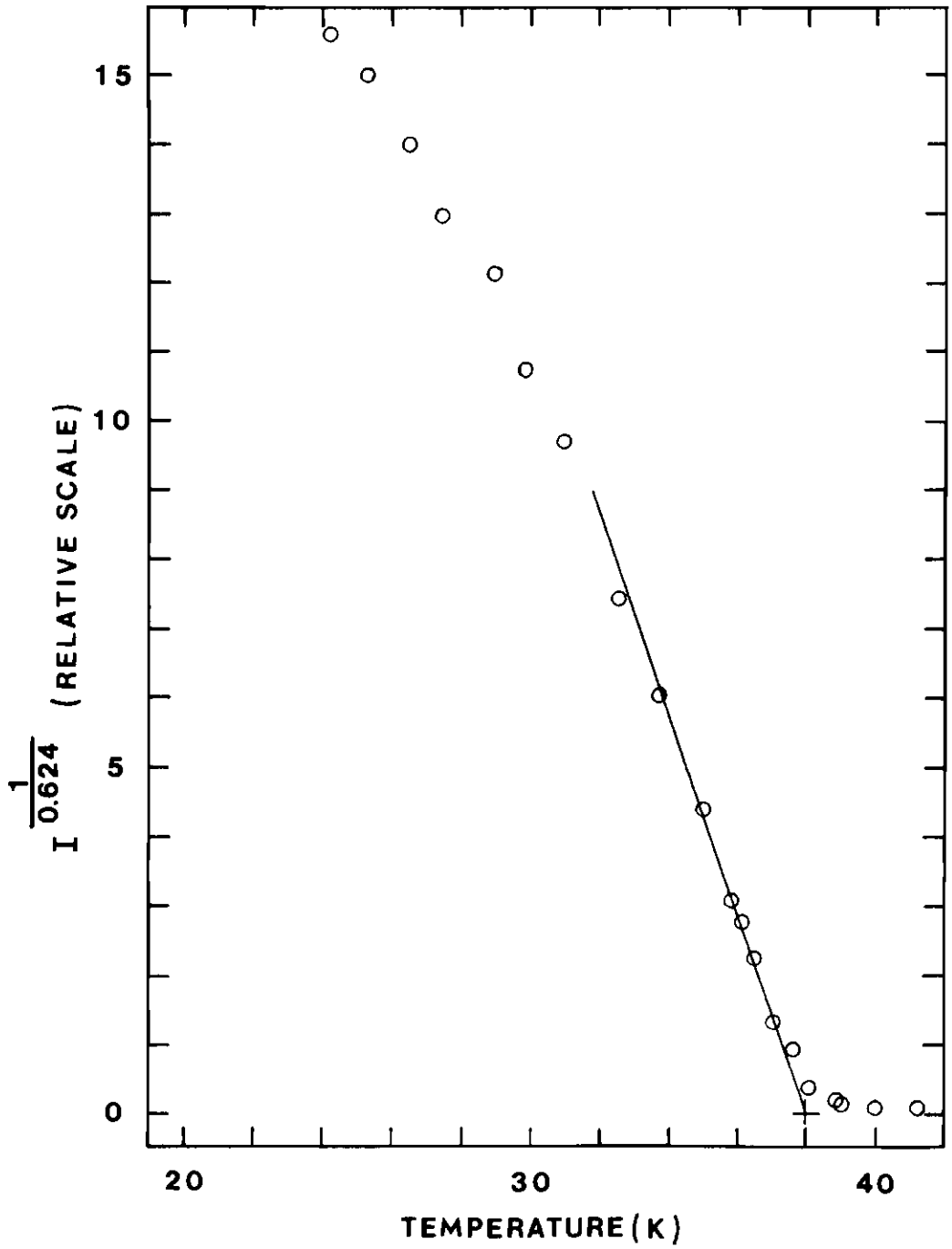

Figure 13. Critical Scattering Graph

to the power (1/0.624) versus temperature. The straight line on the graph is the result of a least squares fitting procedure for the five points from T = 35.0 K to T = 37.0 K. These points were chosen because they are close enough to T_N to follow the power law, but not close enough to be greatly affected by critical scattering. The least squares procedure gave $T_N = 38.0 \pm 0.2$ K. Including a few more or less points in the fitting procedure did not change the calculated value of T_N more than the quoted error limits.

The plot in Figure 13 shows that only a few intensities taken just below T_N need be corrected for critical scattering. Specifically, the points at T = 37.6 K and T = 38.0 K were corrected to the value indicated by the straight line in the graph. After these corrections were made, the reduced sublattice magnetization $< \sigma(T) >_R$ (see Equation (88)) was calculated by taking the square root of the reduced intensity (see Equation (87)). $I_{Mag}^{Bragg}(T=0)$ was calculated by taking the average of corrected intensity values for temperatures between T = 6.5 K to T = 12.5 K. The reduced temperature, T_R, defined by

$$T_R \equiv T/T_N \tag{91}$$

was calculated with $T_N = 38.0$ K.

The plot of $< \sigma(T) >_R$ versus T_R is presented in Figure 14. This plot will be used for comparison with the Monte Carlo results for $< \sigma(T) >_R$. The errors for the data points are smaller than the circle size. The data for the plot are listed in Table 5, Appendix C. The dashed line in Figure

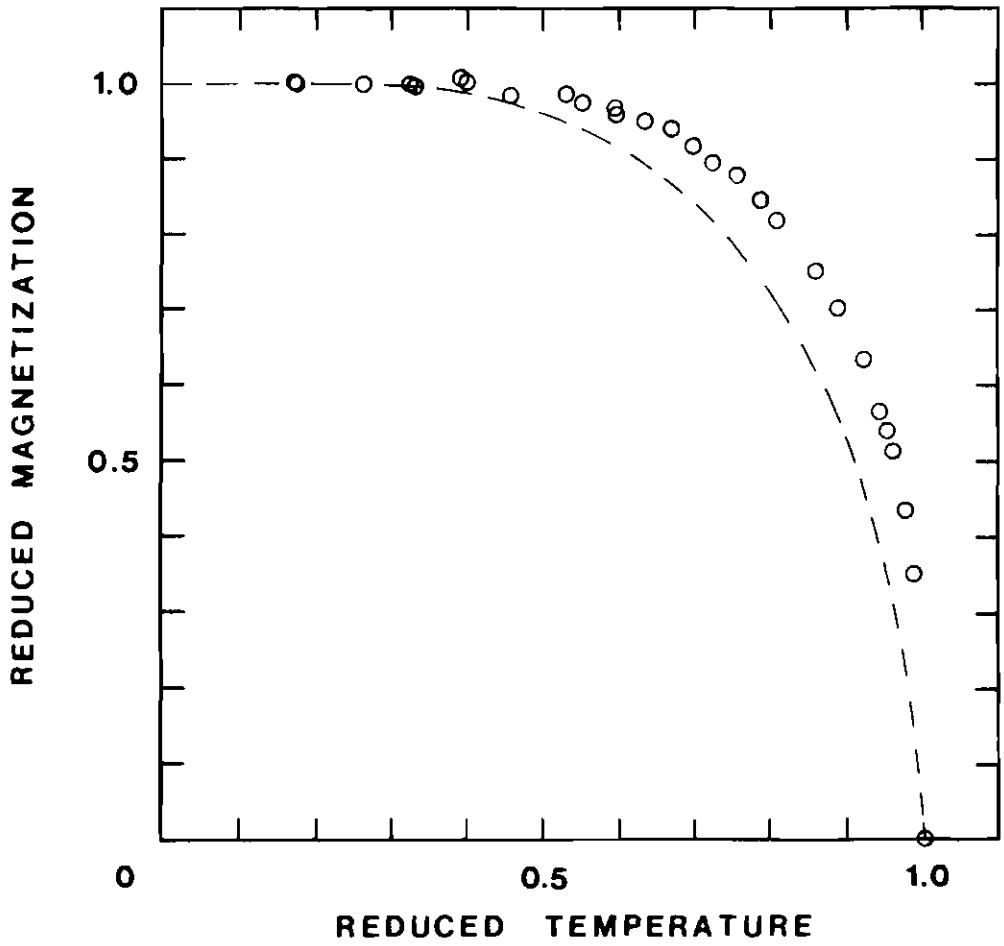

Figure 14. The Measured Reduced Sublattice Magnetization Versus T/T_N

14 is the magnetization curve that is obtained from the Weiss molecular field approximation for a spin 1/2 system with nearest neighbor interactions only. The spin 1/2 curve was chosen for comparison because the ground state of the Fe^{2+} ion is an exchange split doublet. The lack of agreement is apparent. The spontaneous magnetization calculated using the Monte Carlo technique will be discussed in the following section.

Monte Carlo Sublattice Magnetization Results

Before the Monte Carlo magnetization results are presented, the Hamiltonian parameters used in the calculation will be discussed. The Hamiltonian that was used in the Monte Carlo study had the form

$$H = K_{NN} \sum_{i,j}{}' \sigma_i \sigma_j + K_{NNN} \sum_{i,k}{}' \sigma_i \sigma_k \qquad (92)$$

where K_{NN} is the nearest neighbor exchange constant, K_{NNN} is the next nearest neighbor exchange constant, and $\sigma = \pm 1$. The sum i,j is taken over pairs of nearest neighbors and the sum i,k over pairs of next nearest neighbors. Figure 15 shows an outline of the unit cell of $FeCO_3$ along with the first two shells of neighbors for the iron atom at the corner of the unit cell. In the fully ordered ground state, the first shell of neighbors is antiferromagnetically aligned with the central atom. This shell is split into two groups of three atoms each. One group lies in a plane perpendicular to the spin axis and above the central atom. The other group lies in a plane below the central atom. The second shell, which also contains six atoms, lies in the same plane as the central atom and is ferromagnetically aligned with it.

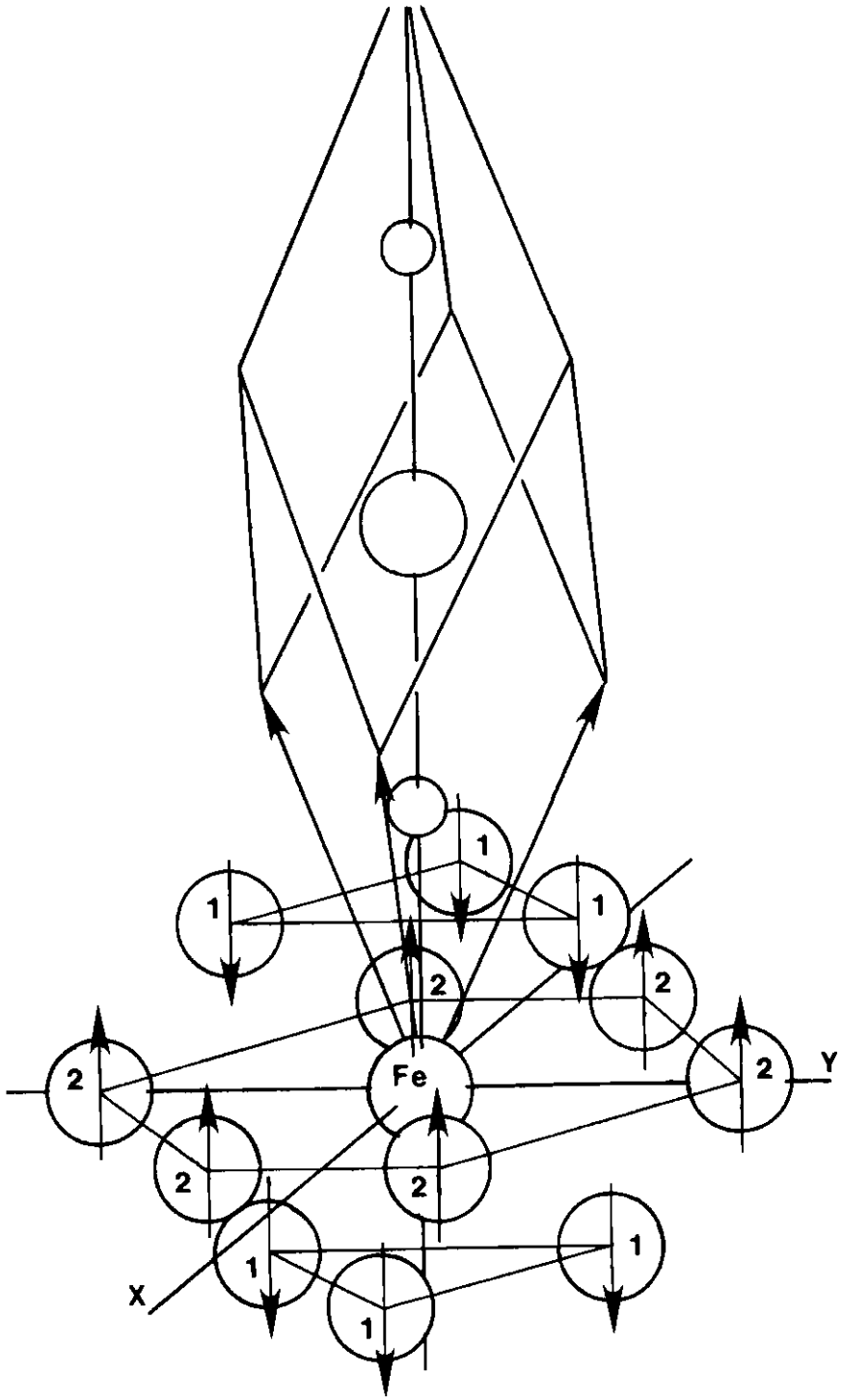

Figure 15. First and Second Neighbor Shells in Iron Carbonate

This structure allows K_{NN} to be determined independently of K_{NNN}. If an external magnetic field is applied along the spin direction, only the first neighbor interaction must be overcome to produce a metamagnetic transition (since the second neighbors will still be ferromagnetically aligned after the transition). Jacobs[5] has measured both the critical magnetic field and the magnetization of $FeCO_3$ at 4.2 K. His values are 145 KOe for the critical field, and 4.6 $\mu\beta$ for the magnetization per Fe^{2+} ion. The equation

$$6\ K_{NN} = \frac{1}{2} \times 0.1337 \times H_o \times M\ , \tag{93}$$

where H_o is the applied magnetic field in KOe, M is the magnetic moment of the ions in Bohr magnetons, and 0.1337 is the energy in (K) that it takes to turn one Bohr magneton over in an external field of one KOe, can be used to calculate K_{NN}. It gives the value

$$K_{NN} = 7.4 \pm 0.5\ K\ .$$

The value of K_{NNN} can be determined from the Monte Carlo results and the ordering temperature of $FeCO_3$. The calculation can be made with K_{NN} fixed at 7.4 K and with different K_{NNN} values until the correct ordering point is obtained. In actual fact, the procedure just described was not used. The following set of calculations, from which the same information could be obtained, had already been performed.

The Monte Carlo calculation was run for the pairs of K_{NN} and K_{NNN} values listed in Table 1. The calculation for each pair of K values was

Table 1. T_N Data from the Monte Carlo Calculation

K_{NN}(K)	K_{NNN}(K)	(K_{NNN}/K_{NN})	T_N(K)	T_N(K) Scaled for K_{NN} = 7.4 K
5.86	- 2.35	- 0.40	38.5 ± .8	48.5 ± .8
6.84	- 1.37	- 0.20	37.5 ± .8	40.5 ± .8
8.20	0.0	0.0	36.0 ± .8	32.5 ± .8
10.28	2.05	+ 0.20	32.5 ± .8	23.4 ± .8

run for three lattice sizes; (4 x 4 x 12), (6 x 6 x 18), and (8 x 8 x 24). The data from these calculations are found in Table 6, Appendix C. In these calculations, and in all of the Monte Carlo calculations described in this thesis, edge effects were eliminated from the data by applying periodic boundary conditions. Five lattice properties were calculated at every temperature during each run. The properties were the energy, E, the sublattice magnetization, the magnetic specific heat, and the first and second neighbor correlations. The specific heat, C_H (at constant external magnetic field), was calculated using the well known result[44]

$$C_H = \frac{1}{kT^2}\left[< E^2 > - < E >^2 \right] . \qquad (94)$$

The spin correlations will be discussed in detail later.

The specific heat was calculated for use in determining T_N by locating the maximum in the C_H versus temperature curve. However, the statistical

error in these data was too large to allow an accurate determination of the ordering temperature. Instead, T_N was determined by the location of the inflection point in the energy versus temperature curve. Figures 16 through 19 show a plot of the energy data for all four (K_{NNN}/K_{NN}) ratios. Only the data points for the two larger lattices are plotted in these figures. The finite size effects in the energy data are small, and no extrapolation procedure was used in this graphical determination of ordering temperatures. A smooth curve has been drawn through the data points. The inflection points, which were determined by inspection, are indicated on the graphs. The T_N values so determined are tabulated in Table 1.

The ordering temperatures just determined can now be scaled to give T_N for each ratio and $K_{NN} = 7.4$ K. The reason that T_N can be scaled is the following. The sublattice magnetization for a specific configuration of a specific model is not an explicit function of K_{NN} or K_{NNN}. Now consider the expression for the thermal equilibrium value for the sublattice magnetization (see Equation (5)),

$$< \sigma(T) > = \sum_u \sigma_u e^{-Eu/kT} / \sum_u e^{-Eu/kT} , \qquad (95)$$

along with the Hamiltonian of Equation (92). Since this thermal expectation value is a function of the ratio Eu/kT only, it is clear that the energy and the temperature can both be multiplied by a constant without changing the value of the expectation value. Now if the sublattice magnetization scales in the sense just described, then the ordering temperature must also scale.

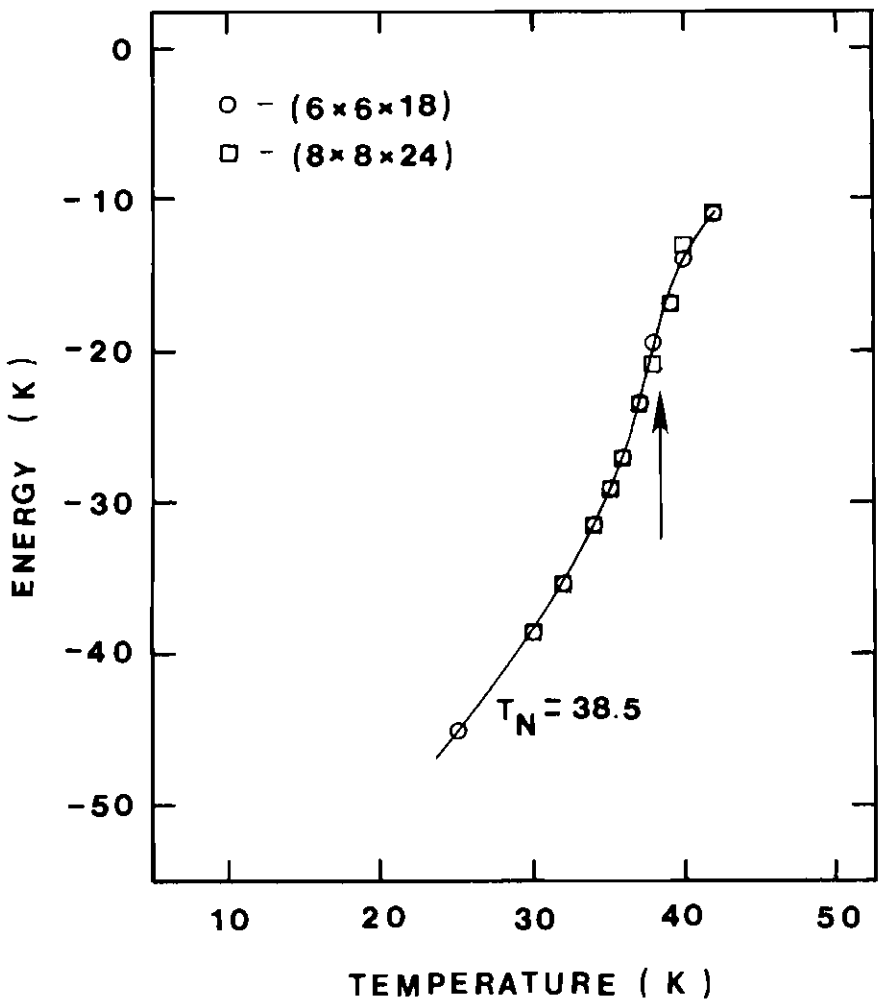

Figure 16. Energy Versus Temperature Curve from Monte Carlo Data for K_{NN}=5.86 and K_{NNN}=-2.35

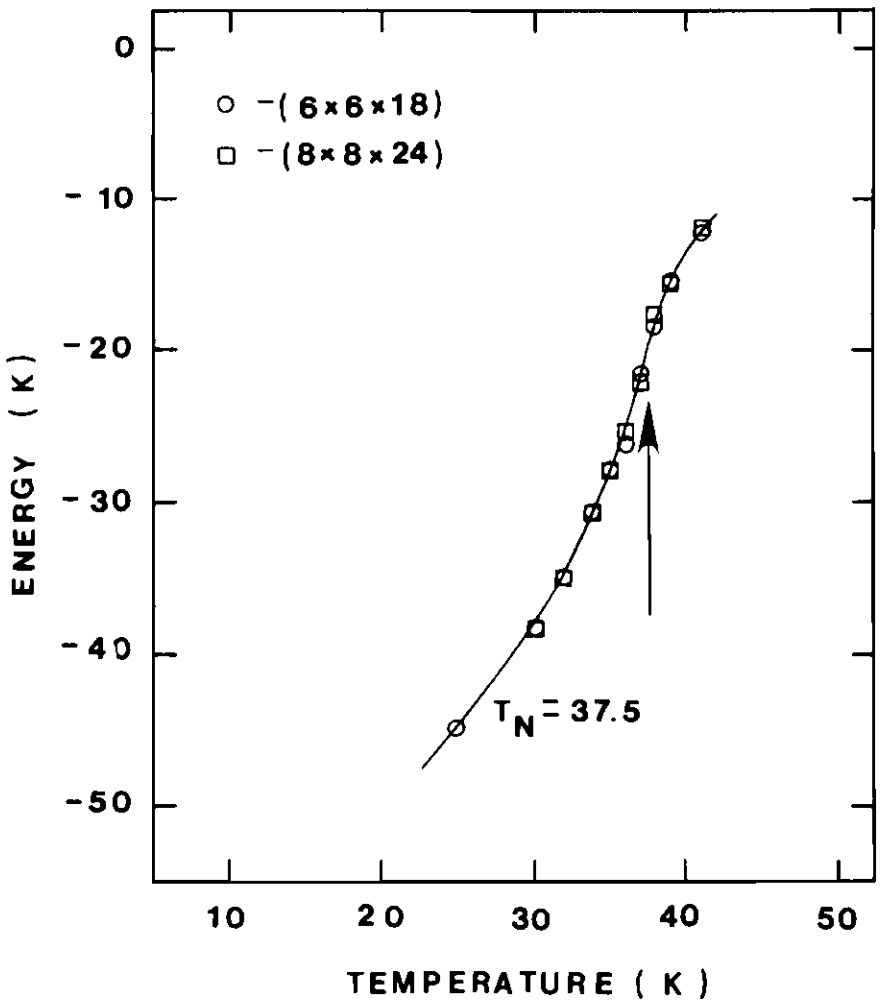

Figure 17. Energy Versus Temperature Curve from Monte Carlo Data for K_{NN}=6.84 and K_{NNN}=-1.37

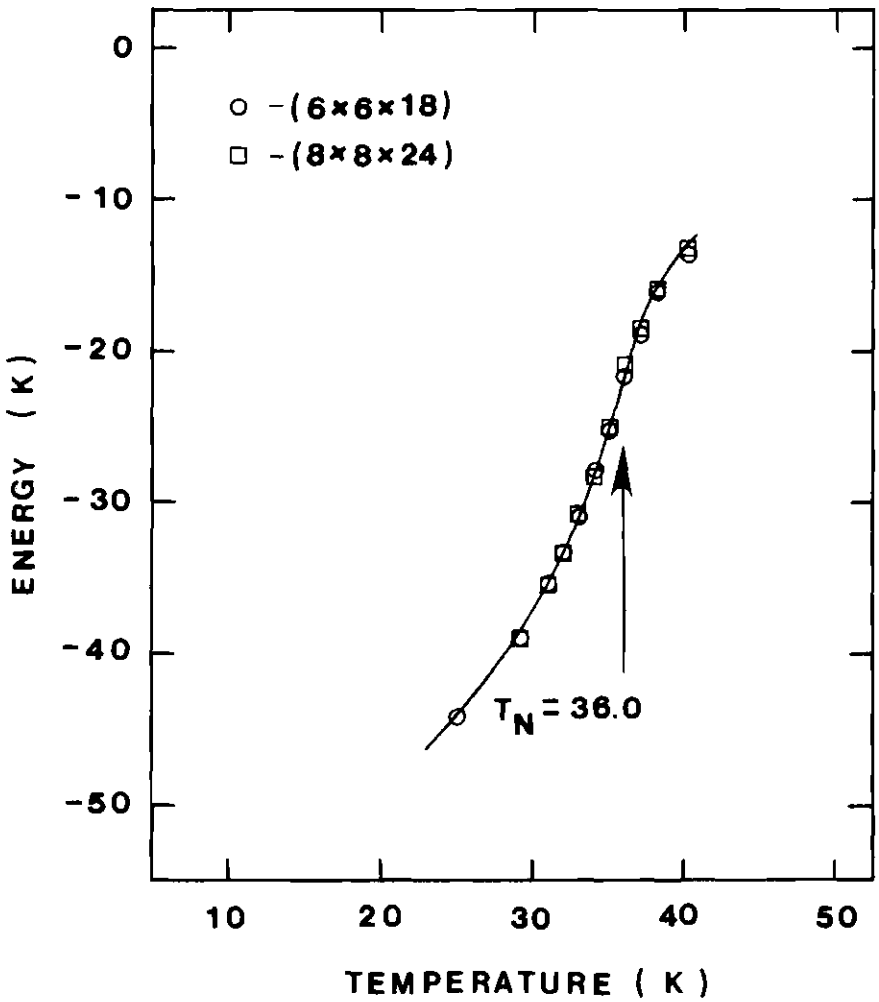

Figure 18. Energy Versus Temperature Curve from Monte Carlo Data for K_{NN}=8.20 and K_{NNN}=0

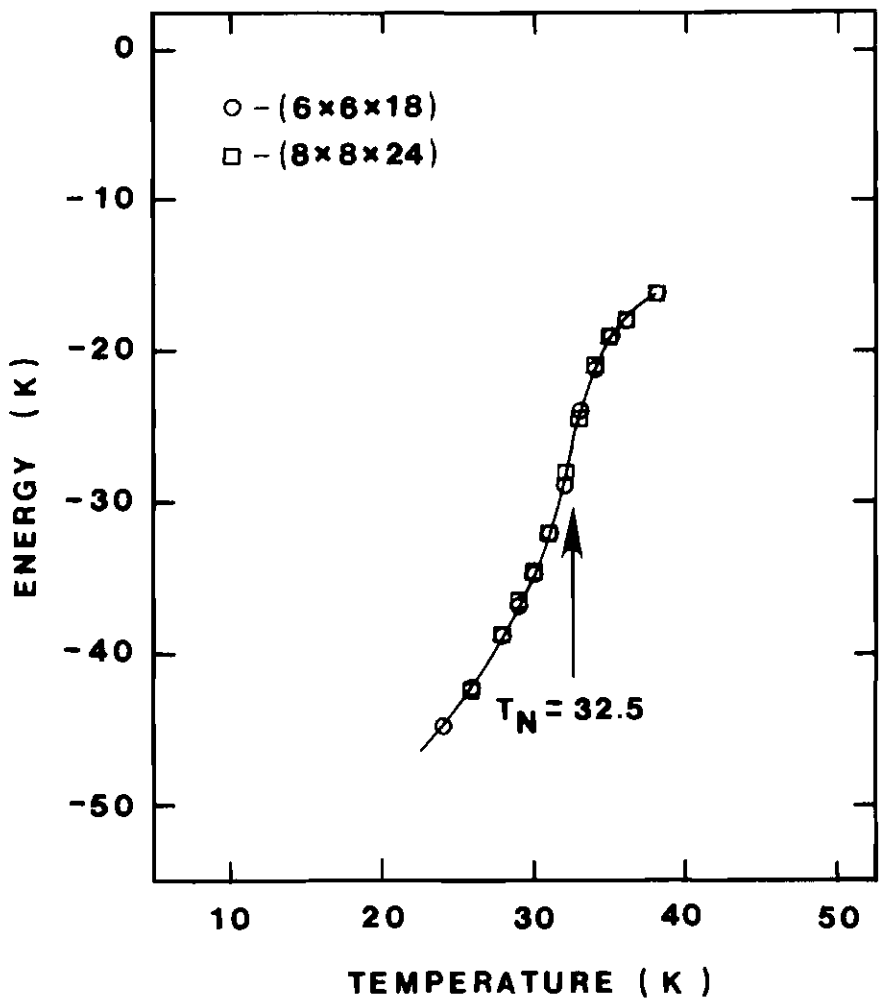

Figure 19. Energy Versus Temperature Curve from Monte Carlo Data for K_{NN}=10.28 and K_{NNN}=2.05

The last column in Table 1 gives the values for T_N scaled for K_{NN} = 7.4 K. These temperatures are plotted in Figure 20 as a function of the ratio (K_{NNN}/K_{NN}). The ordering temperature of the $FeCO_3$ sample used in the neutron study is indicated on the graph. To give the correct ordering temperature, (K_{NNN}/K_{NN}) must be chosen equal to -0.17 or K_{NNN} must equal -1.26. Now to obtain the sublattice magnetization versus temperature curve, the Monte Carlo program could be run again with the appropriate Hamiltonian constants. However, the shape of this curve turned out to be relatively insensitive to the ratio (K_{NNN}/K_{NN}) for negative ratio values.

The reduced sublattice magnetization versus the reduced temperature is plotted in Figures 21 and 22 for all four ratios. The data points on the graphs were obtained by plotting the sublattice magnetization values for each of the three lattice sizes against the reciprocal of the linear lattice dimension and extending a straight line through these points back to zero (infinite lattice size). This procedure has been used in other Monte Carlo studies[45] of two dimensional crystals. This procedure should probably be modified for the three dimensional case, however, the extrapolation produced negligible change in the magnetization values for all temperatures except the last two temperatures before T_N and thus does not have an appreciable effect on the shape of the curves (recall T_N was determined independently).

Since the shapes of the magnetization curves change very little for negative (K_{NNN}/K_{NN}) ratios, the curve for the ratio (K_{NNN}/K_{NN}) = -0.2 was used for comparison with the neutron data. The comparisons are made in Figure 23. The solid line in this figure is a reproduction of the line

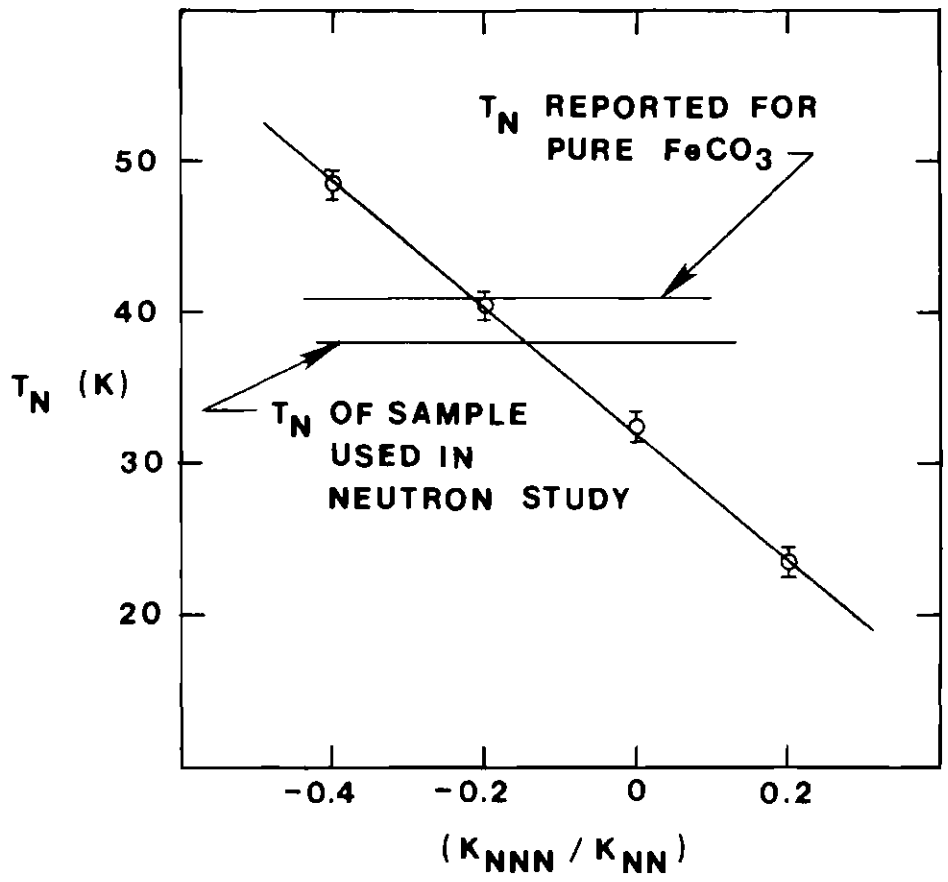

Figure 20. Ordering Temperature Versus the Ratio of Next Nearest to Nearest Exchange Constants with K_{NN}=7.4 K

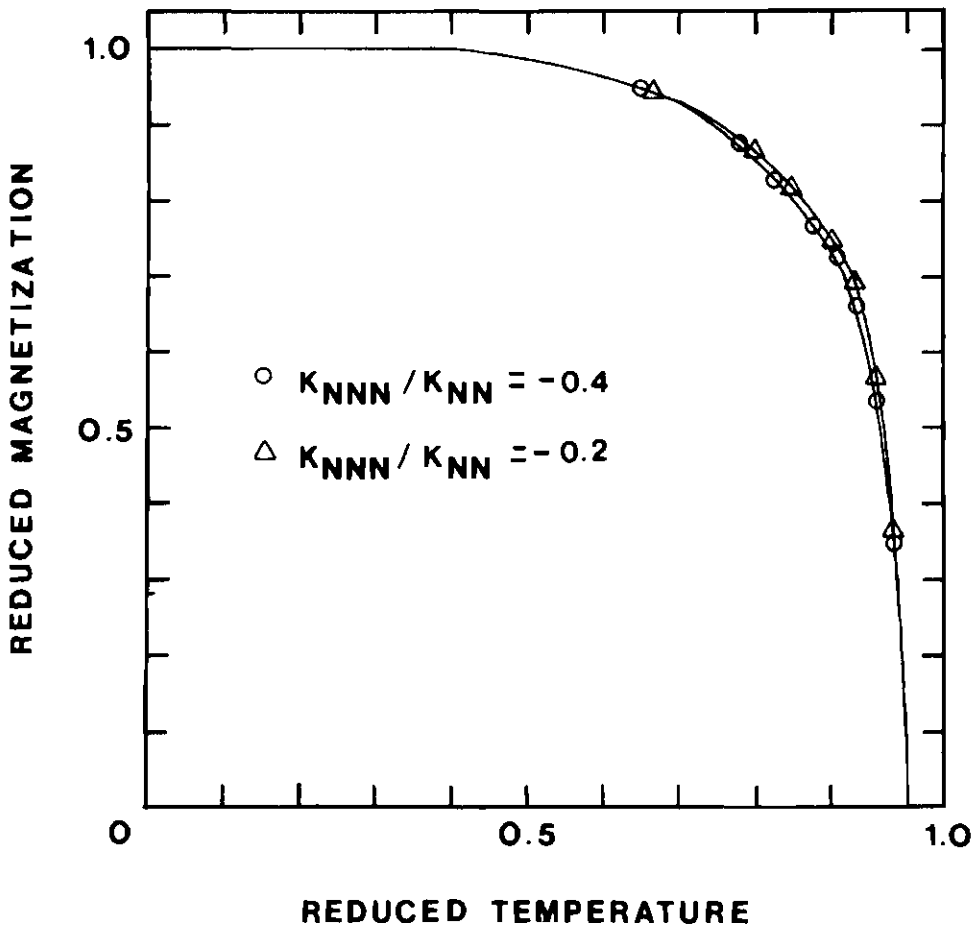

Figure 21. Monte Carlo Magnetization Results for Negative K_{NNN}/K_{NN} Ratios

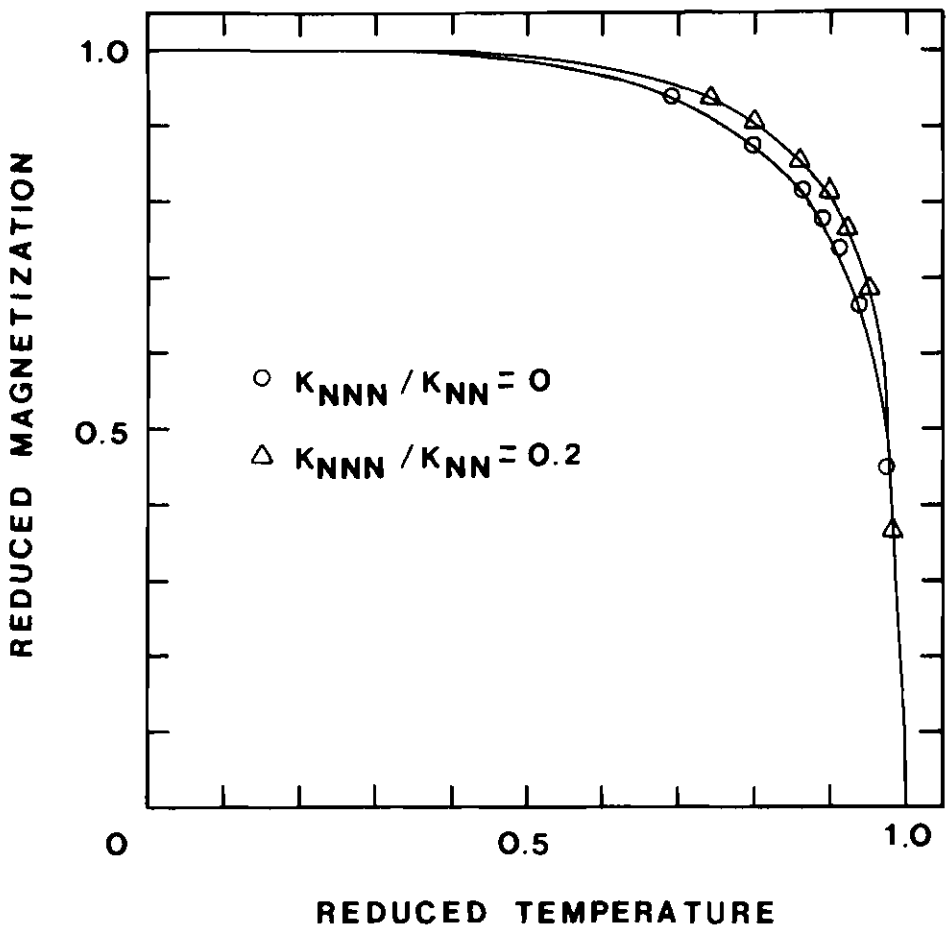

Figure 22. Monte Carlo Magnetization Results for Positive K_{NNN}/K_{NN} Ratios

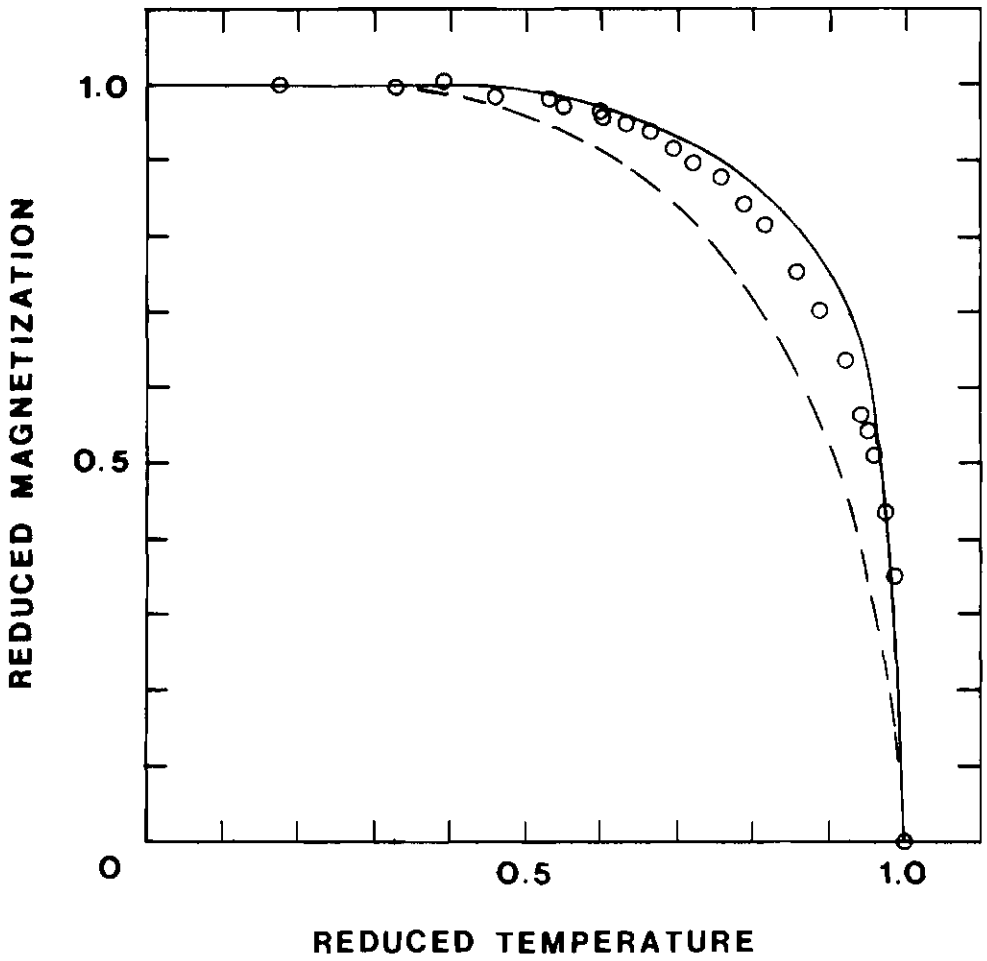

Figure 23. Comparison of Neutron Data with Monte Carlo Curve

through the Monte Carlo data points in Figure 21. The molecular field curve in Figure 14 is repeated in Figure 23 for comparison. The Monte Carlo curve is in better agreement with the neutron data. However, a discrepancy between the neutron results and the Monte Carlo curve still exists and this systematic discrepancy is too large to be explained purely on the basis of statistics.

In an attempt to find the origin of the disagreement, an excited state was included in the calculations. The energy splitting between the ground state and this excited state was set at 115 K in agreement with the measured splitting between these states (see Crystal Field Theory Section). The excited state was assumed to be a singlet. This assumption should overemphasize the effect of the excited state on the results since the first excited state in $FeCO_3$ has a nonzero magnetic moment that can contribute to the net sample magnetization, whereas, a singlet with no magnetic moment makes no contribution. A preliminary run of the Monte Carlo calculation with this singlet excited state produced no measurable effects of any of the calculated property values, however, and this possibility was pursued no further.

A second attempt did produce an improvement in the agreement between the neutron and Monte Carlo results. This time, the impurity content of the sample was taken into account. The two principal cation impurities, magnesium and manganese, were both included in the Monte Carlo model in the concentrations indicated by the spectrographic analysis mentioned earlier. Manganese carbonate, magnesium carbonate, and iron carbonate all have rhombohedral unit cells that are roughly the same in size

and shape, so the assumption was made that the impurity ions substituted for iron ions in the crystal lattice. In fact, the magnetization and susceptibility of iron doped manganese carbonate crystals have been measured,[46] and this study establishes the fact that Fe^{2+} and Mn^{2+} ions do substitute freely in the doped crystals.

The Fe^{2+} ground state was again treated as an exchange split doublet with a magnetic moment along the axis of quantization of $\pm$ 5 (arbitrary units). The ground state electron configuration of the free Mn^{2+} ion is $^6S_{5/2}$[47] (spin = 5/2, orbital angular momentum = 0). The allowed values of the magnetization along the axis of quantization for the exchange split Mn^{2+} ion states were -5, -3, -1, 1, 3, 5. In a detailed study[48] of the magnetic moment distribution in $MnCO_3$, the total magnetic moment of the Mn^{2+} ion was found to be about ten percent less than the free ion value. It was stated earlier that the magnetic moment of the Fe^{2+} ion in $FeCO_3$ has been measured to be 4.6 μ_B. In any event, setting the ground state magnetic moment of the Fe^{2+} ion and the Mn^{2+} ion equal should introduce little error into the calculated results. The ground state electron configuration of the free Mg^{2+} ion is $^1S_0$[46] (spin = 0, orbital angular momentum = 0), and this state was treated as a singlet with no magnetic moment and no exchange interactions.

The Hamiltonian for this study had the same form as the one for the first calculations (Equation (91)), but the allowed values for the σ's were changed and more exchange interactions had to be introduced. The σ's were set equal to the magnetic moments of the states just described. The exchange interactions that were used are listed in Table 2.

Table 2. Exchange Interaction Constants in (K) Used in the Impurity Monte Carlo Calculation

Neighbor Atom	Central Atom Shell	Fe	Mn
Fe	1st	7.40/25	3.00/5
	2nd	1.60/25	0
Mn	1st	3.00/5	0.60
	2nd	0	0

The Fe-Fe first neighbor exchange constant was still 7.4 K (divided by 25 to compensate for the new σ values). The Fe-Fe second neighbor constant was raised slightly to 1.60 K. Jacobs measured the ordering temperature of a synthetic $FeCO_3$ sample to be approximately 41 K, and so the second neighbor constant was raised to take the higher ordering temperature into account (see Figure 20).

Only a nearest neighbor Fe-Mn interaction was used. The exchange constant was determined from inelastic neutron scattering data.[30] In this experiment on a natural $FeCO_3$ crystal, an excitation with an energy of approximately 0.0031 eV (36 K) was measured at 4.2 K. This excitation was not observed above the ordering temperature and was missing from measurements on a pure synthetic $FeCO_3$ powder. So it was assumed that the origin of the excitation was a Mn^{2+} ion surrounded by six iron neighbors. This assumption together with the Hamiltonian of Equation (91) gives the exchange value listed in Table 2. The Mn-Fe exchange interaction was chosen to be antiferromagnetic because iron atoms were found to stabilize a

uniaxial antiferromagnetic spin structure in the Fe^{2+} doped $MnCO_3$ crystals.

Only a first neighbor Mn-Mn interaction was assumed. Its magnitude was chosen to give the observed antiferromagnetic ordering temperature of 34.5 K[46] for pure manganese carbonate. The constant coupling effective field approximation result[19]

$$J = T_N/28.2 \tag{96}$$

gives J = 1.22 K. The Hamiltonian for which the result given by Equation (96) is valid has the form

$$H = 2J \sum_{i,j}' S_i^z S_j^z \tag{97}$$

where the sum i,j is again over pairs of nearest neighbors. So the J calculated using Equation (96) must be divided by two to be used with Hamiltonian of Equation (92).

The impurity version of the Monte Carlo calculation was performed for the same three lattice sizes used in the first calculation. At the beginning of each calculation, impurity ion sites were chosen randomly throughout the lattice in the percents determined in the spectrographic analysis described in Chapter III. The first and second moments of the impurity lattice sites were calculated and compared with the moments of a uniform distribution. These checks indicated that there was no abnormal clustering of impurity sites in the distributions used in the calculations. In addition, the Monte Carlo program was run with different impurity ion site configurations, and the results were always within statistics.

Table 7, Appendix C contains the average property values obtained from the impurity version of the Monte Carlo program. The energies for the (6 x 6 x 18) and (8 x 8 x 24) lattices are plotted in the graph of Figure 24. The ordering temperature was determined from this plot to be 38.5 ± 1.0 K. The reduced sublattice magnetization from the impurity version of the Monte Carlo calculation is plotted in Figure 25. This curve was constructed in the same manner that the earlier reduced sublattice magnetization curves were. The graph in Figure 26 shows the sublattice magnetization curve from the previous Monte Carlo calculation (curve for K_{NNN}/K_{NN} = -0.2 in Figure 21) as a dashed line. The smooth curve drawn through the impurity Monte Carlo results in Figure 25 is reproduced in Figure 26. The data points are again the neutron diffraction results from Figure 14. The agreement between the neutron data and the impurity Monte Carlo results is quite good. The graph in Figure 27 shows both the impurity Monte Carlo data points and the neutron diffraction data points. The symbol size for the data points is approximately equal to the statistical error for both sets of data. This last plot indicates that the Monte Carlo results and the neutron results are now within statistics of each other. This improved fit to the neutron data is good evidence that the impurity ions, magnesium and manganese, in the natural $FeCO_3$ sample were responsible for the original disagreement and not a deviation of the ground state of $FeCO_3$ away from Ising-like behavior.

Neutron Diffraction Diffuse Results

The diffuse magnetic data were taken using the larger of the two $FeCO_3$ samples described in the experiment section. The integrated intensity

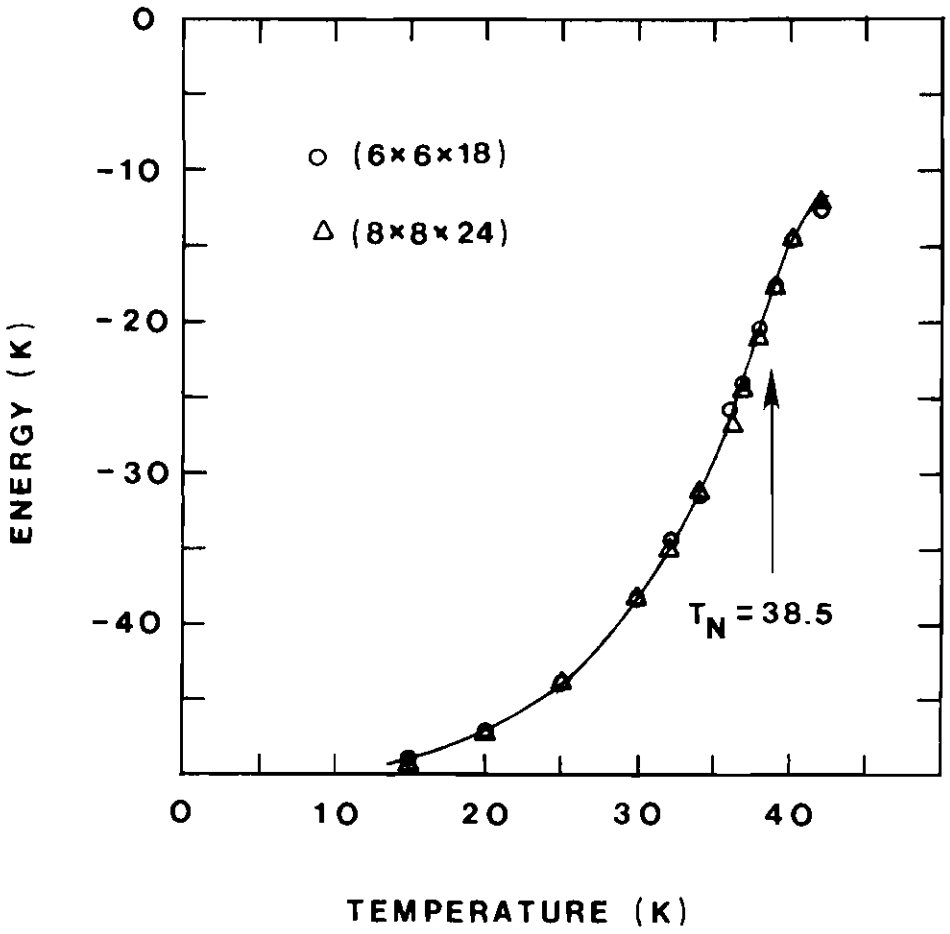

Figure 24. Energy Versus Temperature Curve for Impurity Monte Carlo Data

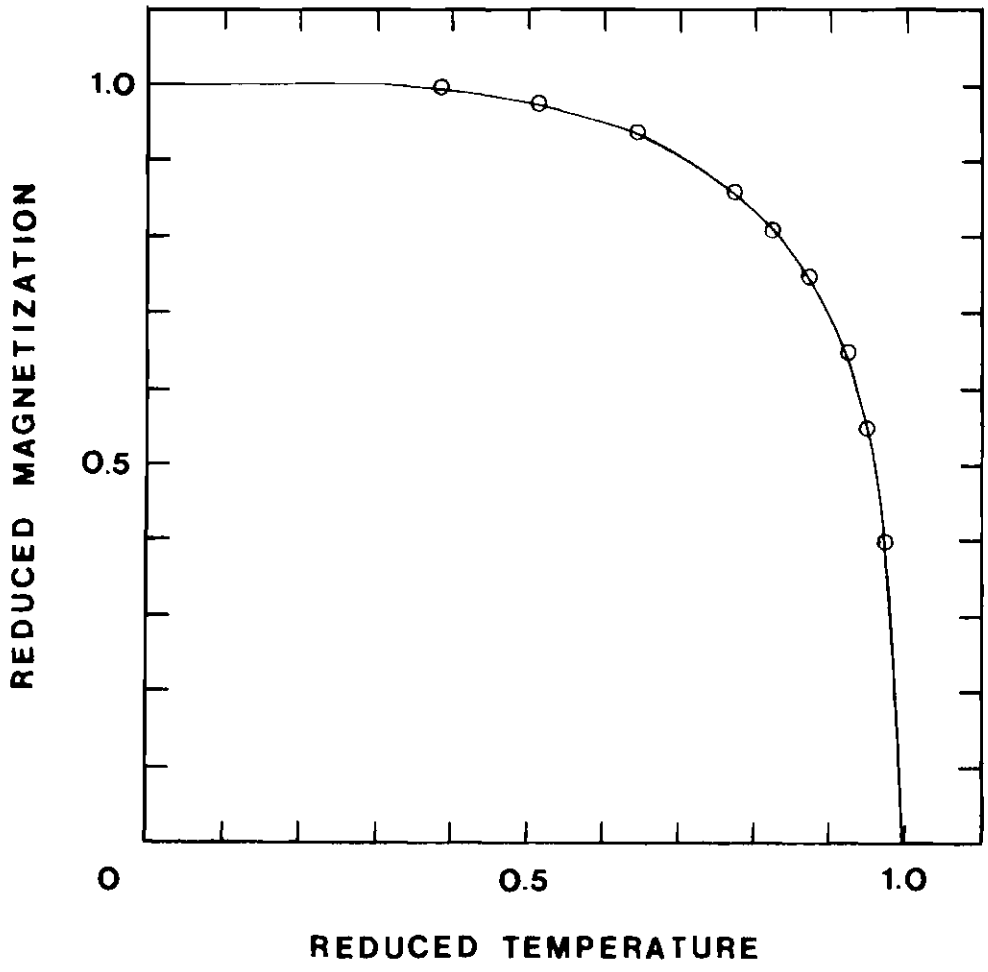

Figure 25. Reduced Sublattice Magnetization Versus Reduced Temperature from Impurity Monte Carlo Program

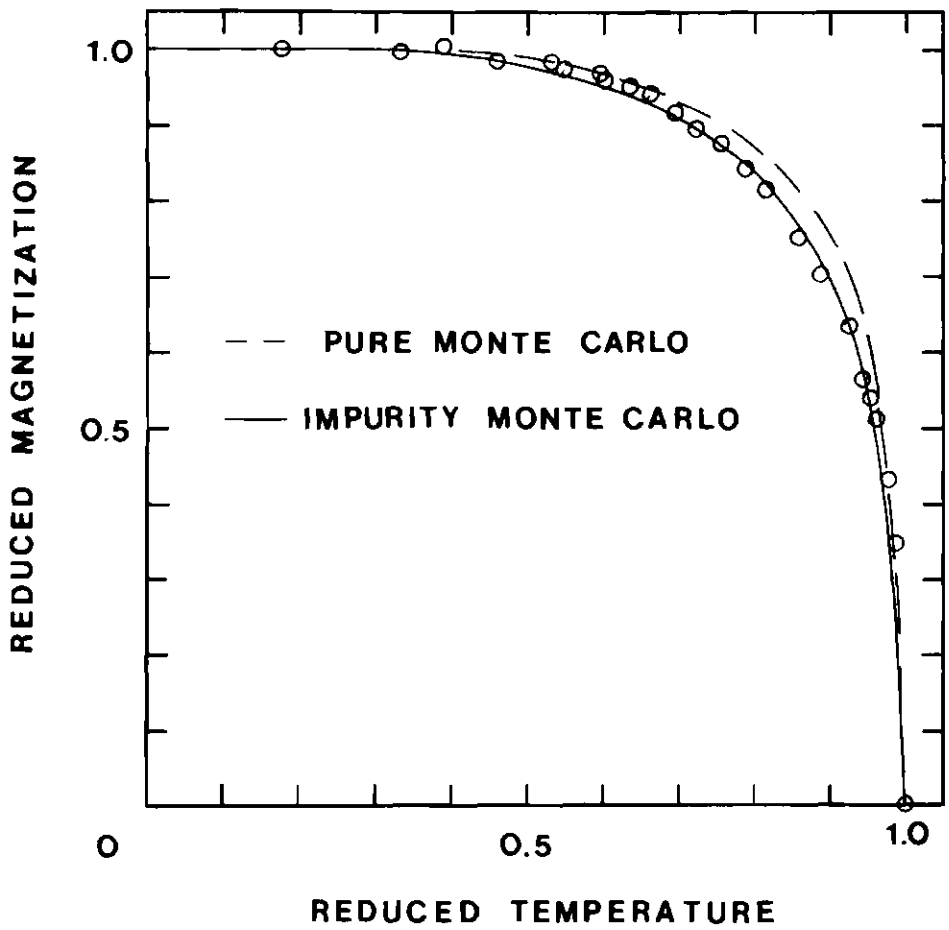

Figure 26. Comparison of Neutron and Monte Carlo Results

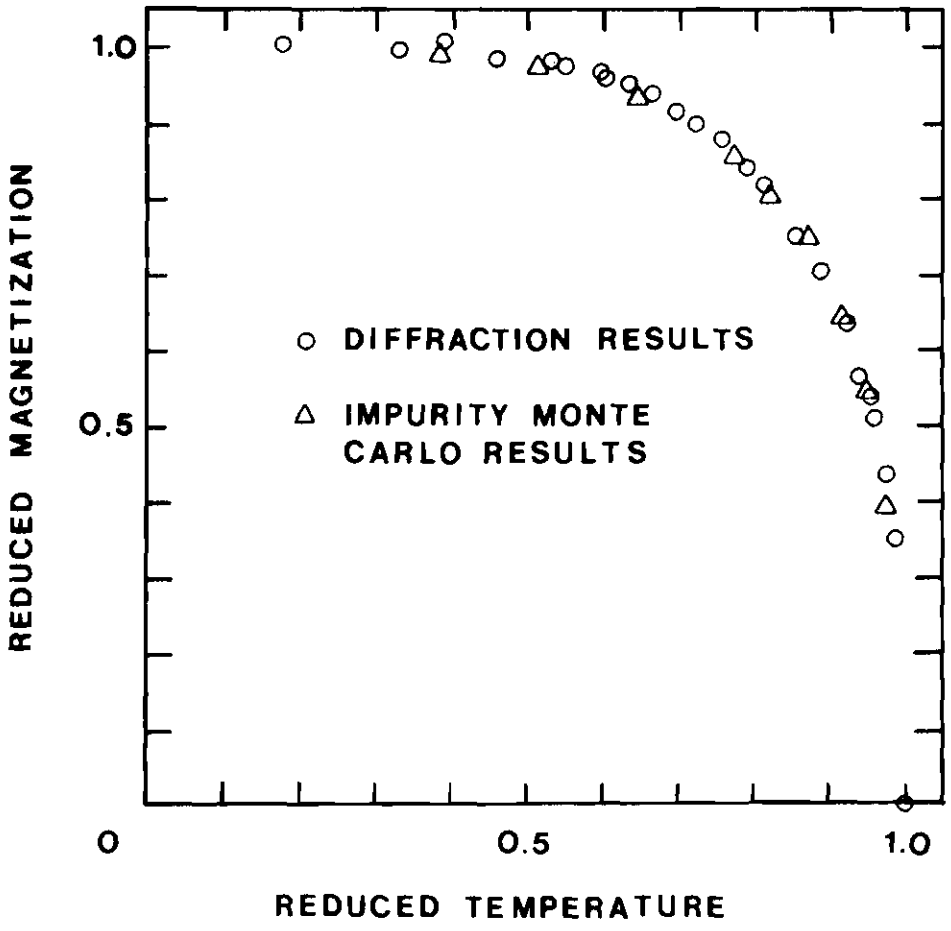

Figure 27. Final Comparison of Neutron and Monte Carlo Results

of the (1 0 0) Bragg magnetic peak was measured at 20 different temperatures. A plot of $I^{1/0.624}$ versus temperature was made for these data (see Figure 13). This plot gave an ordering temperature of 37.2 ± 0.2 K, slightly lower than the ordering temperature, T_N, measured for the smaller Bragg sample. This difference in the ordering temperatures of the two samples was probably due to their different impurity contents.

Diffuse data were taken at 38.8 K, 41.2 K, and 77 K in the Brillouin zone centered about the (1 0 0) reciprocal lattice vector. Data were taken at 37.5 K, 41.1 K, and 77 K in the Brillouin zone centered about the (1 1 1) reciprocal lattice vector. In the (1 0 0) Brillouin zone, data were taken along straight lines in two different directions. One line was approximately parallel to the spin direction, and the other line was perpendicular to the spin direction. In the (1 1 1) Brillouin zone, data were gathered along a line that was approximately parallel to the spin direction. These directions are further defined in Figure 28. Data were also taken at 5.5 K for all three scans.

Some of the reasons for choosing these scans have already been discussed in the Magnetic Brillouin Zone Section. These scans were also chosen to avoid λ/n Bragg scattering (n an integer) in the diffuse data. This scattering is small compared to the scattering of neutrons with wave length λ from the same peak. However, it is comparable in intensity to the diffuse magnetic scattering in the (1 0 0) Brillouin zone. Analysis of the λ/n scattering in the (1 0 0) Brillouin zone indicated that there would be little nuclear scattering in the two chosen scan directions. There was no evidence of λ/n scattering in the background scans at 5.5 K confirming this analysis.

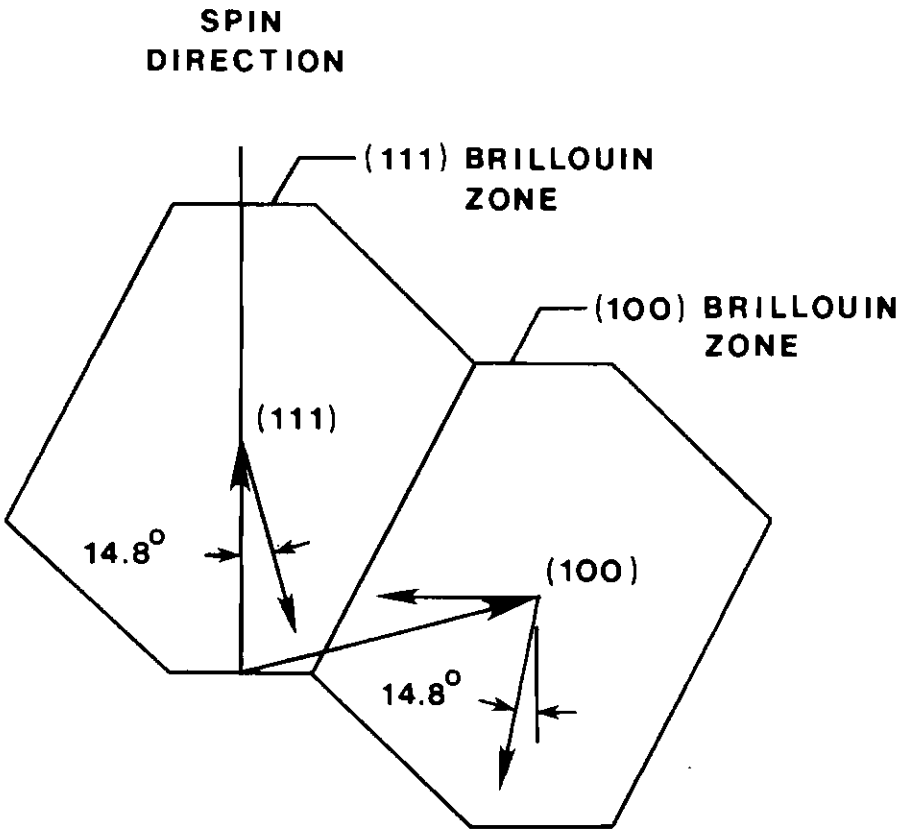

Figure 28. Vectors in Reciprocal Space Which Define Directions of Diffraction Scans

Figures 29 and 30 are plots of the data taken in the (1 0 0) Brillouin zone. Figure 29 shows the data taken in the direction that is approximately parallel to the spin direction, and Figure 30 shows the data taken in the direction perpendicular to the spin direction. The distance away from the tip of the (1 0 0) reciprocal lattice vector is plotted along the horizontal axis in both graphs. The average counting time for each point was 25 minutes above T_N and 10 minutes below T_N. The points on the graphs were obtained by subtracting the counts measured above T_N from the counts measured below T_N after both of these numbers were normalized to a ten minute counting time. These two sets of neutron scattering data are compared with a calculated cross section based in part on spin correlation coefficients calculated using the Monte Carlo technique described earlier.

The useful portion of these straight line scans was limited. Bragg scattering at the reciprocal lattice point prevented the measurement of diffuse scattering for very small distances away from the tip of the (1 0 0) lattice vector. This Bragg scattering has two origins. The theoretical structure factor for the (1 0 0) nuclear Bragg peak is zero, but the perfect order assumed in the structure factor calculation is never present in a natural crystal. In addition to this nuclear scattering from the (1 0 0) Bragg peak, λ/n scattering from the (2 0 0), (3 0 0), etc. peaks also occurs at the (1 0 0) lattice vector site. These second order effects were easily corrected for in the sublattice magnetization measurements since they are relatively small. However, the Bragg scattering proved to be too large to permit a reliable correction in the diffuse data close to the origin of the (1 0 0) Brillouin zone. The diffuse counting rate decreases

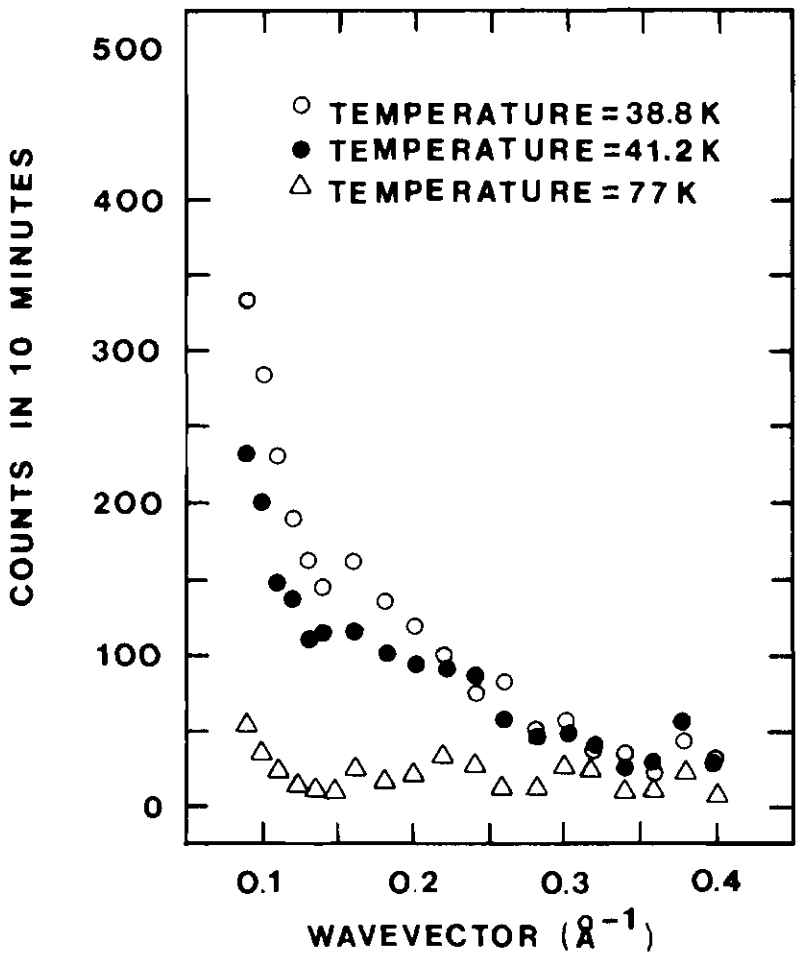

Figure 29. Diffuse Magnetic Scattering Data in the Direction Approximately Parallel to the Spin Direction

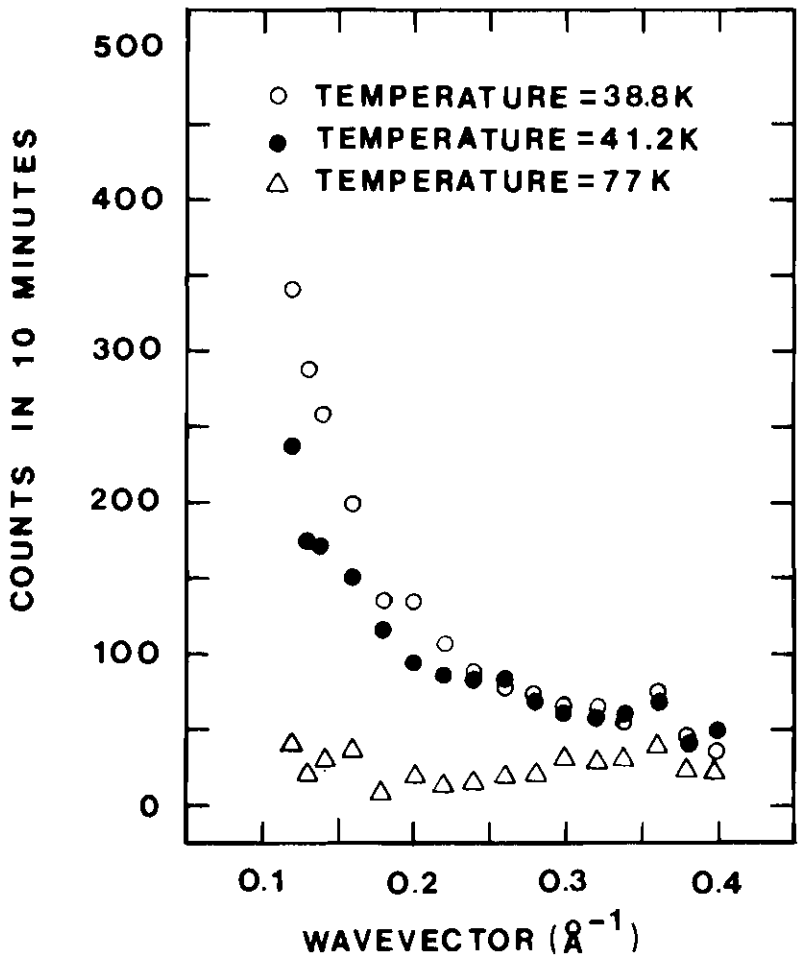

Figure 30. Diffuse Magnetic Scattering in the Direction Perpendicular to the Spin Direction

as the distance from the center of the Brillouin zone increases, and poor statistics in the data far from the zone center limited their usefulness.

Figure 31 is a plot of the data taken in the (1 1 1) Brillouin zone. These data points were again obtained by subtracting the neutron counts measured below T_N from the counts measured above T_N. The counting time for all of the points was 10 minutes both above and below T_N. The average counting rate (corrected for background scattering) along this line in reciprocal space was - 2.5 ± 3 counts in ten minutes for data taken at 37.5 K, + 3.0 ± 3 counts in ten minutes for the 41.1 K data, and + 2.5 ± 3 counts in ten minutes for the 77 K data. In contrast, the average corrected counting rate for a similar scan in the (1 0 0) Brillouin Zone at 41.2 K was 115 ± 11 counts in ten minutes. This anisotropy is expected in the diffuse scattering from a magnetic Ising system and therefore provides further evidence that $FeCO_3$ is a three dimensional magnetic Ising system. The data from these experiments are listed in Table 8, Appendix C.

Monte Carlo Spin Correlation Results

The cross section for diffuse magnetic scattering above the ordering temperature for an Ising system was developed in Chapter III. It is repeated here for convenience.

$$\frac{d^2\sigma}{d\Omega\, dE} = 2N\left(\frac{\gamma e^2}{m_e c^2}\right)^2 e^{-2W(\vec{K})}\left|F(\vec{K})\right|^2 (1 - K_z^2)\,\delta(\omega) \times \tag{98}$$

$$\times \left(1 + \frac{1}{N}\sum_{\vec{l}\neq\vec{d}\neq 0}^{*} \cos\left[\vec{K}\cdot(\vec{l} + \vec{d})\right] \cdot \sigma(\vec{l},\vec{d})\sigma(\vec{0})\right) >$$

An experimentally determined effective form factor, $e^{-2W(\vec{K})}\left|F(\vec{K})\right|^2$, will

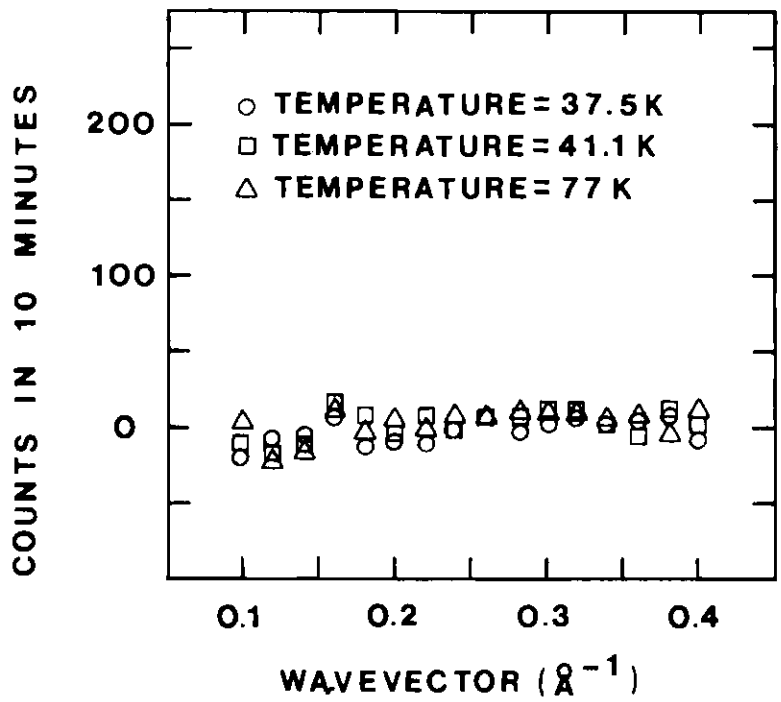

Figure 31. Diffuse Magnetic Data Taken in the (1 1 1) Brillouin Zone

be described in the next section. The Monte Carlo results for the spin correction coefficients $< \sigma(\vec{l},\vec{d})\sigma(\vec{0}) >$ are discussed in this section. The cross section in Equation (98) is then calculated, folded with an experimentally measured resolution function and compared with the neutron results.

Spin correlation coefficients were generated at four temperatures using the Monte Carlo technique described earlier. The model used in this part of the study was the impurity version that gave good agreement with the neutron sublattice magnetization results. The ordering temperature for this model was determined to be 38.5 ± 1.0 K, so the Monte Carlo program was run for 41 K, 42 K, 43 K, and 45 K. These temperatures are in the same range in which the neutron diffuse scattering data were gathered.

Finite size effects are present in the spin correlation coefficients, just as they are in the sublattice magnetization results. Again, they are most important close to the ordering temperature. There is, however, an additional finite size effect in the spin correlation numbers. As the distance away from the central atom increases, the finite size effects become more prominent.

The temperatures used in this study, however, lie outside the range where finite size effects are important for very large models. This conclusion is based on two observations. Size effects were large in the sublattice magnetization data only for temperatures within a few degrees of T_N. It is reasonable to expect finite size effects to be important in the spin correlation numbers in roughly the same temperature range above T_N. Secondly, when the Monte Carlo spin correlation coefficients are compared with various analytical forms, the coefficients generated at all of the temperatures except 41 K yield consistent results. This comparison is

presented later in this section.

To allow the evaluation of Equation (98), and to allow a meaningful comparison with other spin correlation results, it was necessary to increase the size of the Monte Carlo models. Two model sizes were used. They were 8 X 8 X 24 and 20 X 20 X 30 which contain 1,536 and 12,000 atoms, respectively. The second size was so large that the neighbor table (see Chapter II) had to be dropped from the Monte Carlo program in order to fit the program into the available computer core. This modified Monte Carlo program was slower and more expensive to run, but it did yield reliable spin correlation coefficients for a much larger range of neighbors than the smaller models.

Figure 32 is a plot of the spin correlation coefficients generated at 42 K using the 20 X 20 X 30 lattice model. The coefficients for the first 18 shells of neighbors are shown. The distance $|\vec{l} + \vec{d}|$ in angstroms away from a central atom is plotted along the horizontal axis. The vectors $\vec{l}$ and $\vec{d}$ were defined in Equation (35). The coefficients are normalized so that $| < \sigma(\vec{l} + \vec{d})\sigma(\vec{0}) > | = +1$ in the fully ordered state. Several features that characterize the Monte Carlo results in general are apparent in these data. It is evident that the correlation coefficients fall off very quickly as the distance $|\vec{l} + \vec{d}|$ increases. There is also a small, but unmistakable anisotropy in the coefficients. A single smooth curve cannot be drawn through all of the data points. This anisotropy is small in an absolute sense, but it cannot be neglected when the Monte Carlo results are compared with the temperature series and Ornstein-Zernike forms. Finally, the magnitude of correlation coefficients is very small for all of the neighbor shells except the first few. This small size makes it

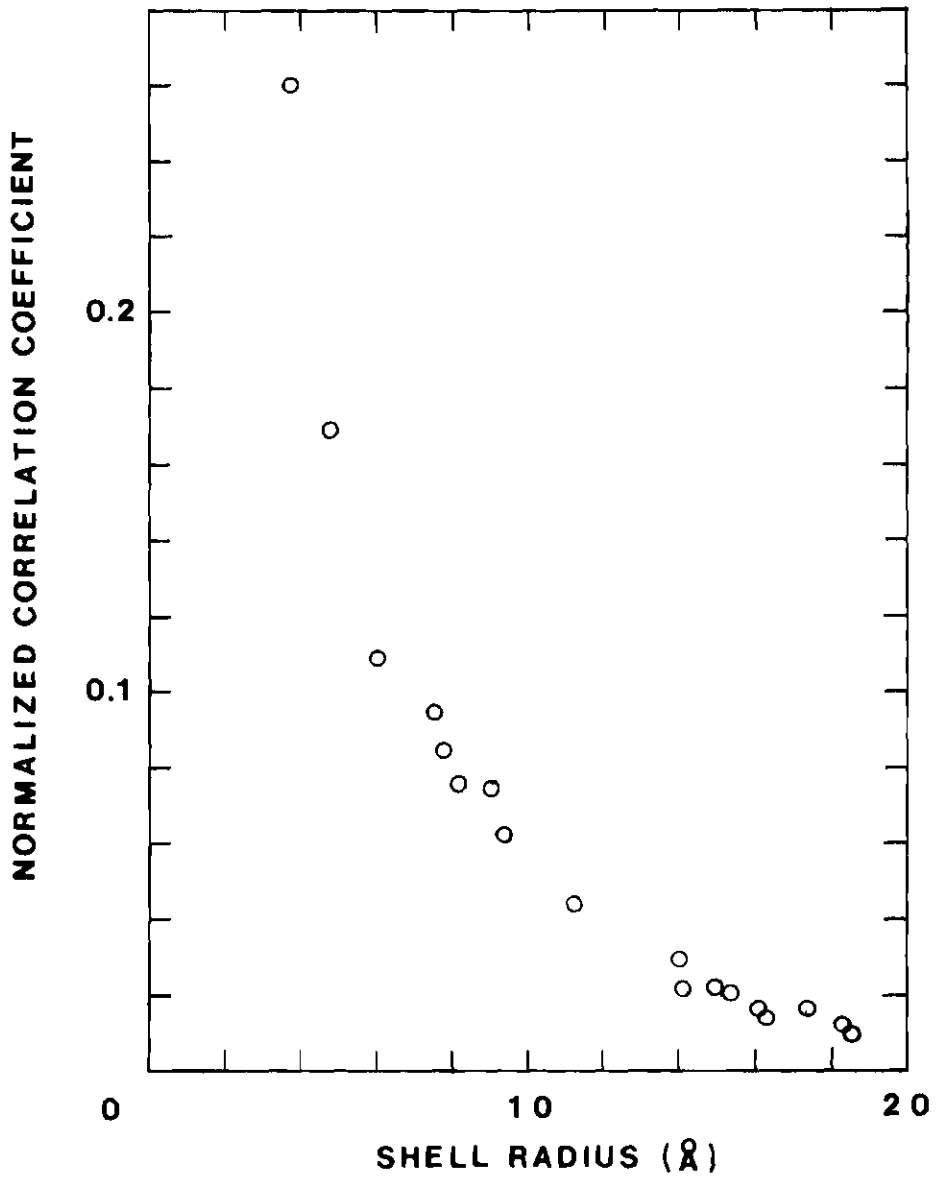

Figure 32. Monte Carlo Spin Correlation Coefficients for the First 18 Shells of Neighbors at 42 K

difficult to obtain accurate coefficients for the more distant neighbors.

Comparison of the Monte Carlo results will now be made with two forms. The first is the Ornstein-Zernike form (where $r = |\vec{l} + \vec{d}|$)

$$| < \sigma(\vec{r})\sigma(\vec{0}) > | = C \frac{e^{-\kappa r}}{r} . \tag{99}$$

The second is the modified Ornstein-Zernike form (see Equation (16)),

$$| < \sigma(\vec{r})\sigma(\vec{0}) > | = C \frac{e^{-\kappa r}}{r^{1+\eta}} . \tag{100}$$

Strictly speaking, the simple comparison which follows is not correct. Both of the forms (99) and (100) apply only in certain limiting cases[26,49] that were not treated in this Monte Carlo study. For instance, the Ornstein-Zernike form was originally derived only for r approaching infinity. The modified form (100) was derived for fixed κr and for temperatures very close to the critical temperature. This fact means the true value of η in the modified form cannot really be determined using the present Monte Carlo results. Although the comparison is not a rigorous test of these forms, it is still very useful. This comparison makes possible a quantitative estimate of the rate at which the spin correlations fall off with increasing r, and it also allows the anisotropy in the Monte Carlo data to be quantitatively characterized. And finally, it should be pointed out that both forms fit the Monte Carlo data rather well. There is little difference in the two forms in three dimensions since η is small for this case.[26]

Spin correlation coefficients for neighbors that lie along various

radial directions passing through the central atom were generated. Four such directions were studied. The first direction was along the spin direction (Z-axis in Figure 15). This direction passes through atoms in the seventh neighbor shell, 36th shell, and 98th shell. The second direction considered was in the direction of a nearest neighbor. This line passes through atoms in the first, fifth, 16th, 33rd, and 58th shells, and makes an angle of 46.6° with the spin direction. The spin correlations of atoms along two lines in the plane perpendicular to the spin direction were studied. The first of these lines passed through an atom in the second nearest neighbor shell and also atoms in the 11th, 27th, 60th, and 104th shells. The other line passed through atoms in the eighth, 42nd, and 115th shells.

The first question that was investigated was the rate at which spin correlations fall off with increasing radius in a particular direction. The spin correlations for atoms in the direction of the nearest neighbors were used for this study because this was the direction in which the most data points could be accurately generated. Plots were made of $\ln[< \sigma(r)\sigma(0) > r^{1+\eta}]$ versus r (see Equations (99) and (100)) for $\eta = 0$ and $\eta = 0.056$. Figure 33 is the plot for $\eta = 0$ and Figure 34 is the plot for $\eta = 0.056$. Both forms fit the data reasonably well. An attempt was made to find the value of η that best fit the data. A least squares fit of a straight line to the data at 42 K and 43 K was performed for different values of η. The results indicated that η values in the range from -0.1 to $+0.1$ all fit the data about equally well. Again, this is not a definitive test of the value of η, but it is safe to conclude that even in this temperature and radius range, the deviation of spin correlations

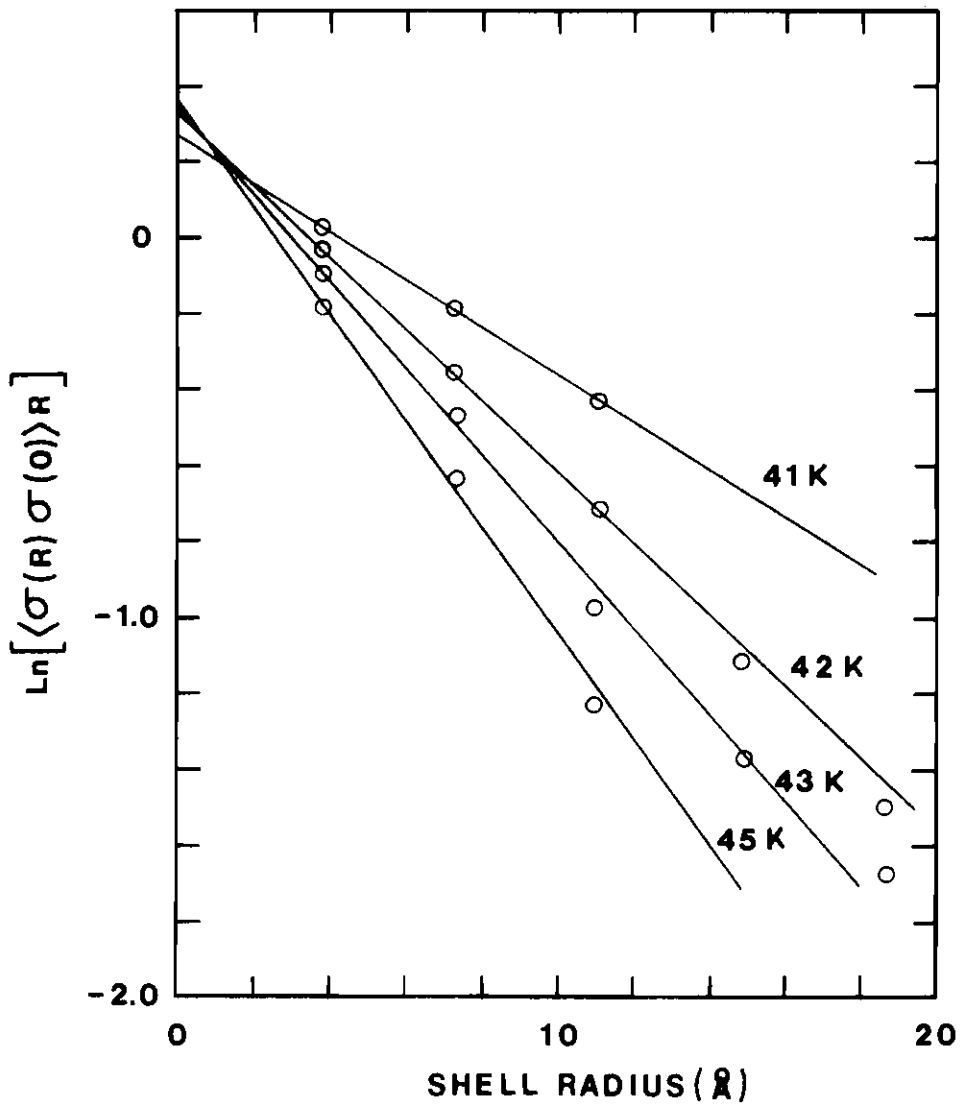

Figure 33. Plot of the Monte Carlo Results in the Nearest Neighbor Direction for η =0

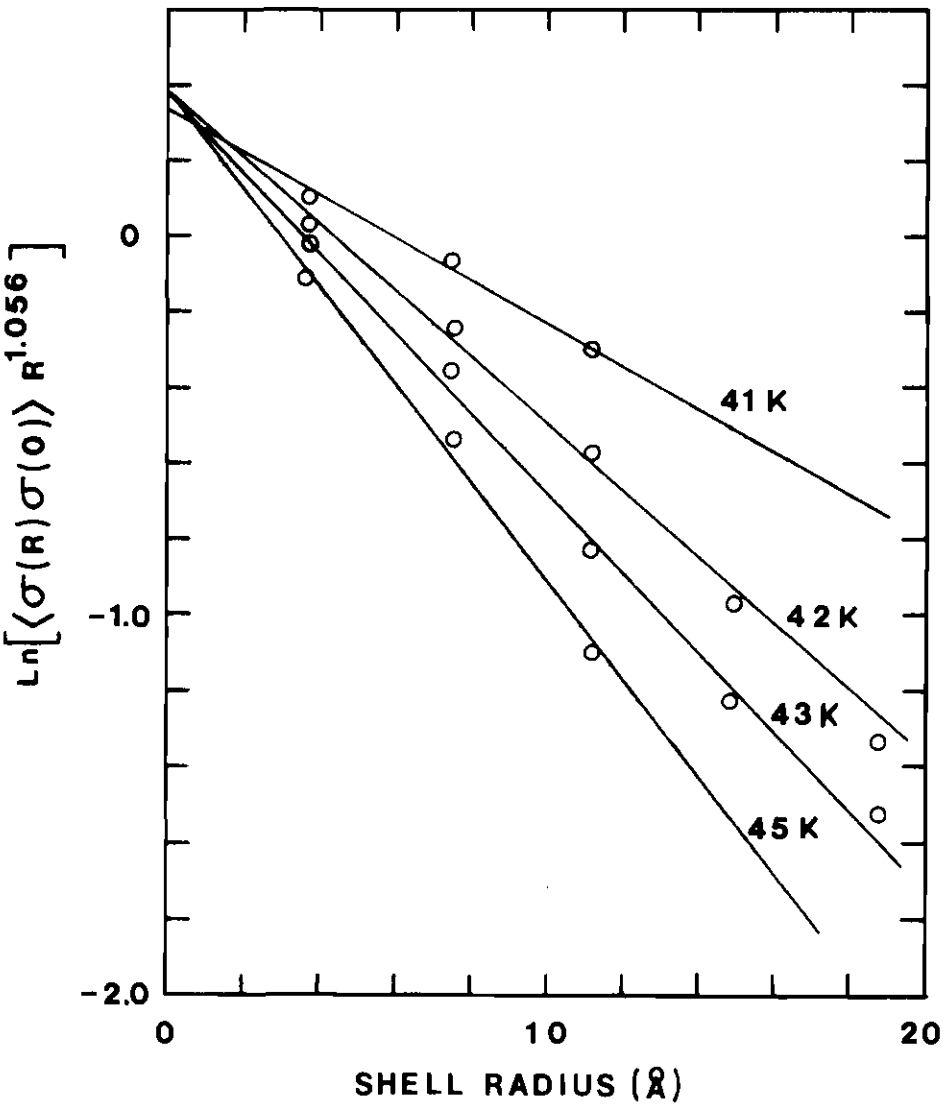

Figure 34. Plot of the Monte Carlo Results in the Nearest Neighbor Direction for η =0.056

away from the Ornstein-Zernike form is relatively small.

Next, the anisotropy in the Monte Carlo results was investigated. Figures 35 and 36 show the spin correlations at 42 K and 43 K for all four neighbor directions. The straight lines for the correlations in the nearest neighbor direction are the same lines that appear in Figure 34. Only two data points along the spin direction were calculated, and a straight line has been drawn through the center of these points. The third straight line resulted from a least squares fit of all of the data points in the plane perpendicular to the spin direction. All three lines have virtually the same slope in each graph, but their intercepts at r = 0 differ. The equation of the lines in these graphs is

$$< \sigma(r)\sigma(0) > = C \frac{e^{-\kappa r}}{r^{1.056}} , \qquad (101)$$

or

$$\ln(< \sigma(r)\sigma(0) > r^{1.056}) = \ln(C) - \kappa r . \qquad (102)$$

In general, the inverse range parameter, κ, is expected to be isotropic only at the ordering temperature.[26] However, since κ is equal to the slope of the lines in Figures 35 and 36, there is little evidence that κ is anisotropic at the temperatures considered in this Monte Carlo study.

The intercept, C, does have a definite directional dependence, but it has little temperature dependence. This lack of temperature dependence is evident in Figures 33 and 34 for the correlations in the nearest neighbor direction. Only the line fit to the 41 K data has a T = 0 intercept

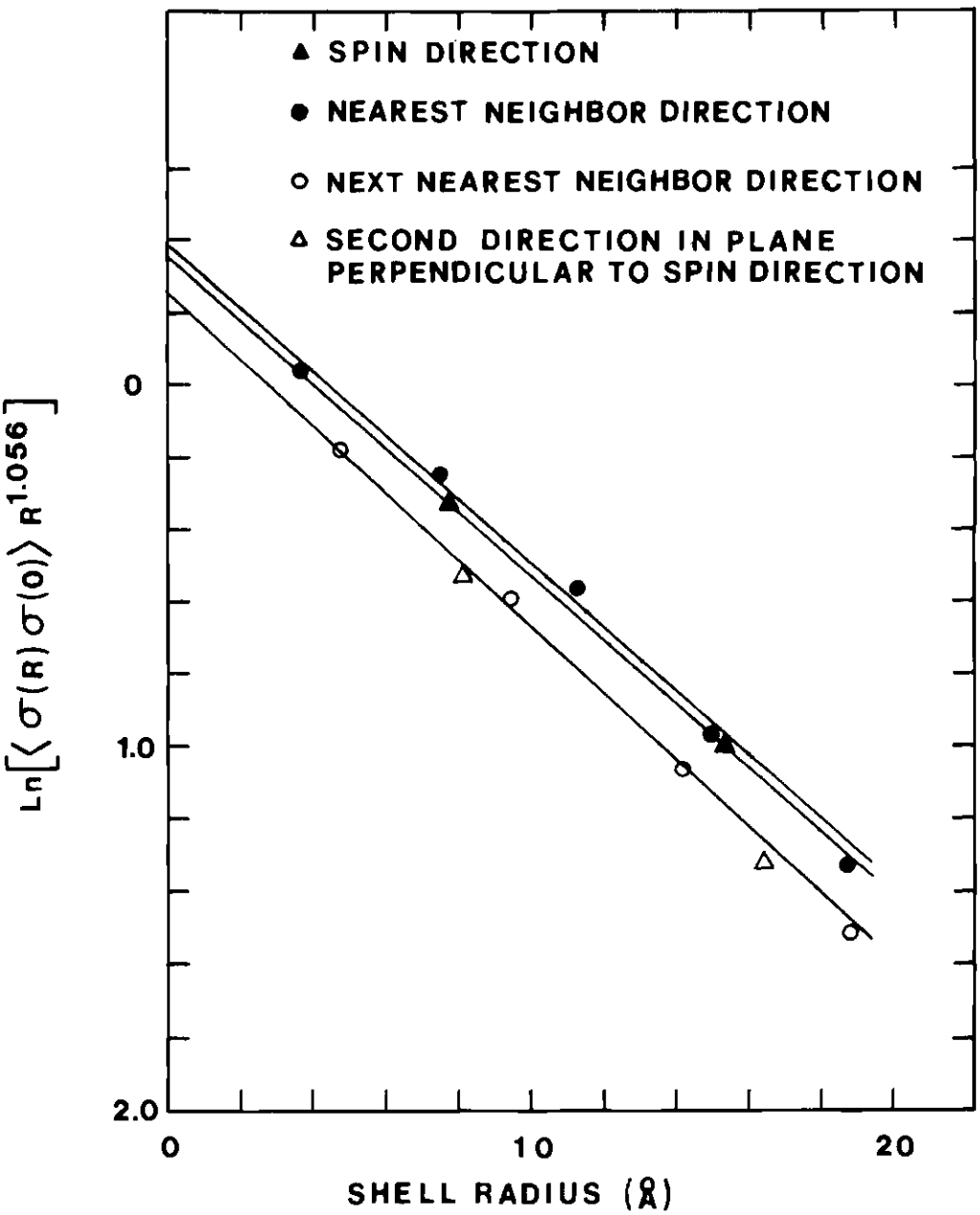

Figure 35. Monte Carlo Spin Correlation Coefficients at 42 K

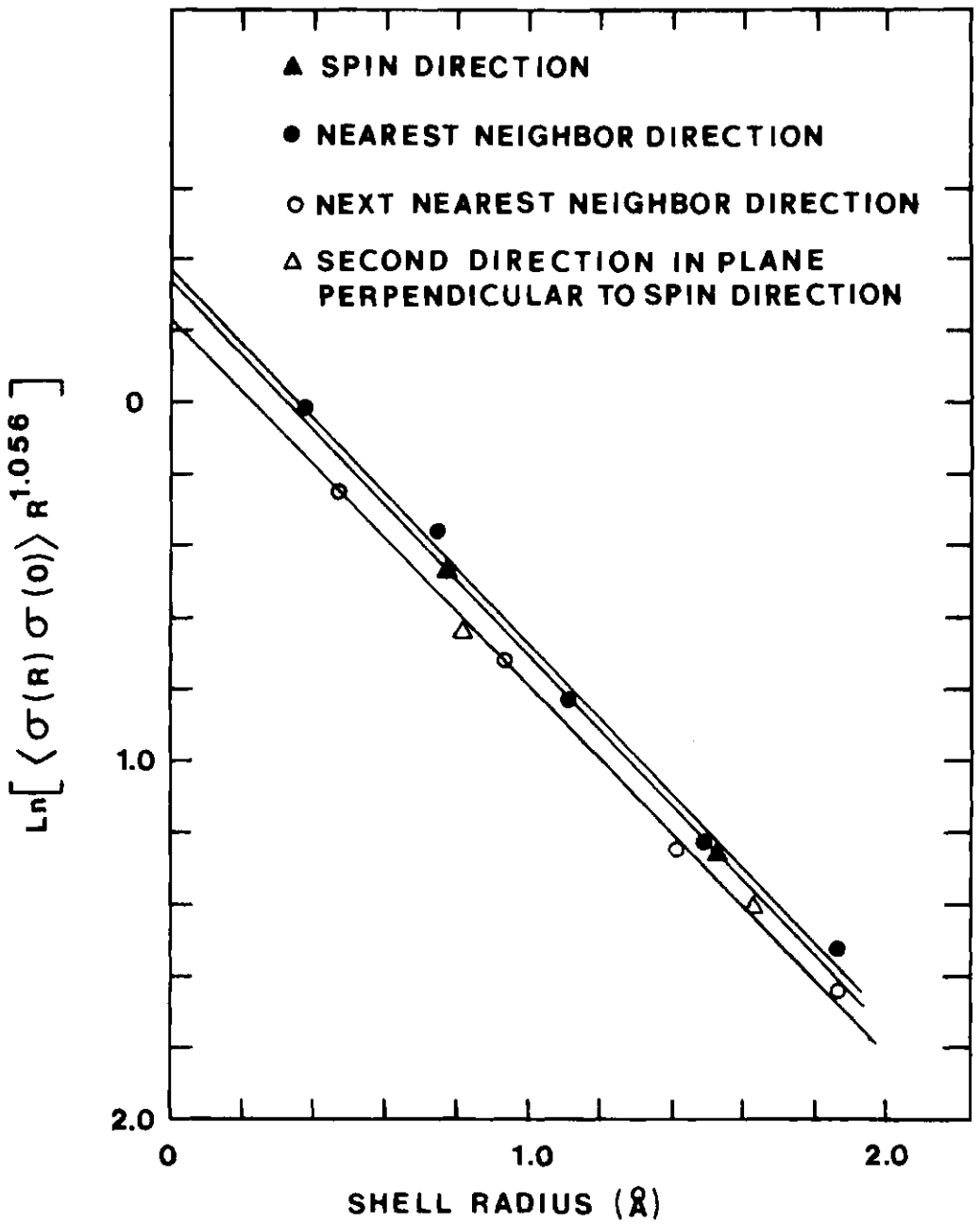

Figure 36. Monte Carlo Spin Correlation Coefficients at 43 K

that is appreciably different from the others. This difference could be due to the finite size effects in the data mentioned earlier. It is also possible that at 41 K the Ornstein-Zernike form no longer applies for small values of r, since κ is relatively small at this temperature. If the 41 K data are not used, the average value of C is 1.40 ± 0.04 from Figure 33 and 1.43 ± 0.03 from Figure 34. In contrast, the average value of C for spin correlations in the plane perpendicular to the spin direction was 1.27 ± 0.03.

The temperature dependence of κ was also investigated. It was stated in the introduction that κ is expected to vary as $(T/T_N - 1)^{\nu}$ with $\nu = 0.643$ (see Equation (17)). Figure 37 is a plot of

$$B = \kappa / \left(\frac{T - T_N}{T_N}\right)^{0.643} , \qquad (103)$$

where clearly B is the constant of proportionality in the power law. Again the Monte Carlo data fit the predicted form rather well if allowance is made for the fact that there are significant finite size effects in the data generated at 41 K. The average value of the constant B for the data at the other temperatures is 0.42 ± 0.02. The results described in this section will be used in a later section to calculate the diffuse neutron scattering cross section. The coefficients from the Monte Carlo calculations are listed in Table 9, Appendix C.

Form Factor Results

The neutron magnetic form factor of the Fe^{2+} ion in $FeCO_3$ had not been calculated. However, Watson and Freeman[50] have calculated atomic

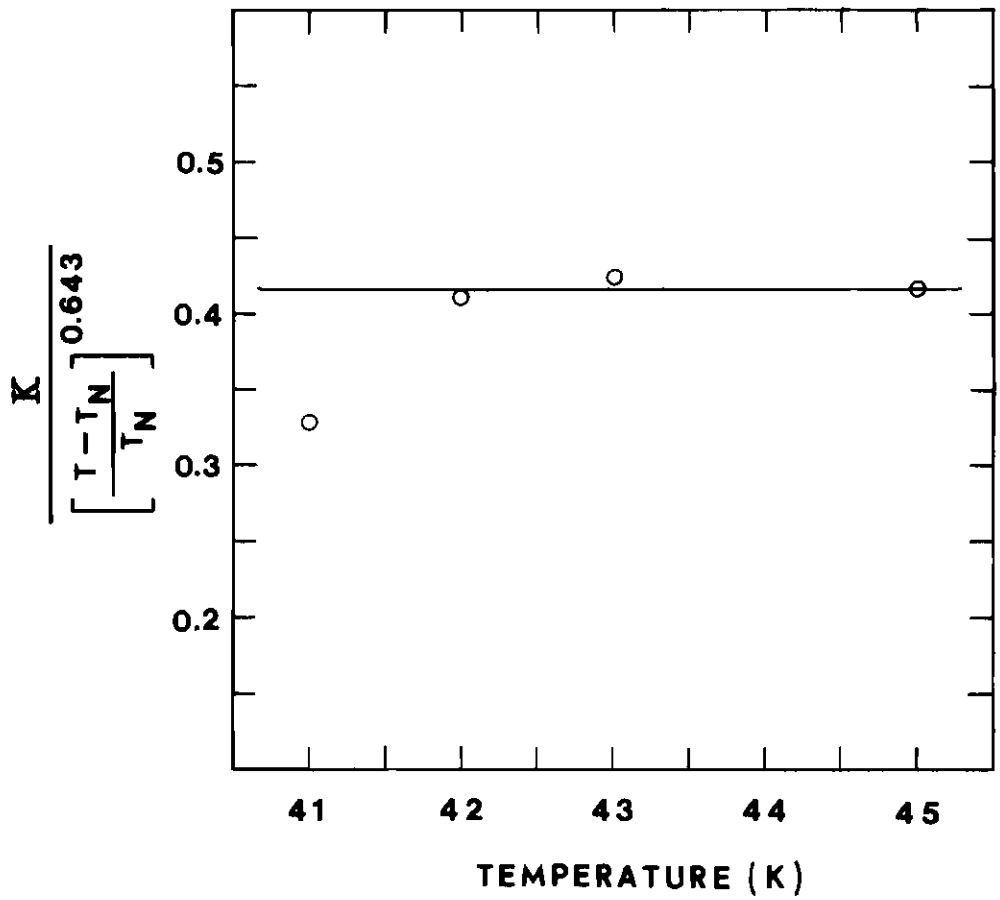

Figure 37. Temperature Dependence of the Inverse Range Parameter

scattering factors using Hartree-Fock self-consistent field wave functions for the free Fe^{2+} ion. These free ion scattering factors can be used to approximate the form factor of Fe^{2+} ions in crystals. A spherically symmetric approximation called the dipole approximation[51] has the form

$$F(K) = A[j_o(K) + Dj_2(K)] \tag{104}$$

where the j's are the scattering factors tabulated by Watson and Freeman.

To check the adequacy of this form in the $FeCO_3$ case, the integrated Bragg intensities of 15 magnetic peaks were measured at 5.5 K. These measurements were made using the small $FeCO_3$ sample used in the sublattice magnetization experiments. The data were corrected for extinction, and a plot of the form factor versus $\sin(\theta)/\lambda$ or $|\vec{K}|$ was made. The extinction correction used in this analysis is the same correction used in the sublattice magnetization analysis.

In the comparison of the dipole approximation with the neutron data, analytical forms for j_o and j_2 were used. The forms are

$$j_o(x) = Ae^{-ax^2} + Be^{-bx^2} + C$$

and

$$j_2(x) = (Ae^{-ax^2} + Be^{-bx^2} + C)x^2 \tag{105}$$

where $x = \frac{\sin(\theta)}{\lambda}$. Lisher and Forsyth[52] have shown that these forms are excellent representations of the tabulated scattering factors of Watson

and Freeman, and they have calculated constant values appropriate for the Fe^{2+} case.

The circles in Figure 38 are the form factor values obtained from the neutron data. The statistical errors in the data are smaller than the symbol size. The solid line in this figure is the calculated form factor, Equation (104). The constants in Equation (104) were determined by a least squares fitting procedure. The agreement between the calculated and measured form factor is good in an absolute sense. There are deviations away from this isotropic form that are too large to be entirely accounted for by statistics. These deviations are small, however, and the isotropic form will be used in the neutron diffraction cross section. The data from the neutron diffraction experiment are listed in Table 10, Appendix C.

The Resolution Function

A number of experimental arrangements were tried before the diffuse magnetic data were taken. The object of these changes was to find an optimum combination of crystals and collimators that would produce a high counting rate and minimize λ/N and inelastic scattering in the data. The (1 1 1) Bragg reflection of a germanium crystal was used to monochromate the neutron beam. The (2 2 2) reflection in germanium has a zero structure factor, and there is little $\lambda/2$ contamination in a beam monochromated with the (1 1 1) reflection. The (2 0 0) reflection of a copper crystal was used to analyze the energy of the scattered neutrons because it gave a better combination of intensity and energy resolution than a second germanium crystal. The horizontal mosaic spread of both of these crystals

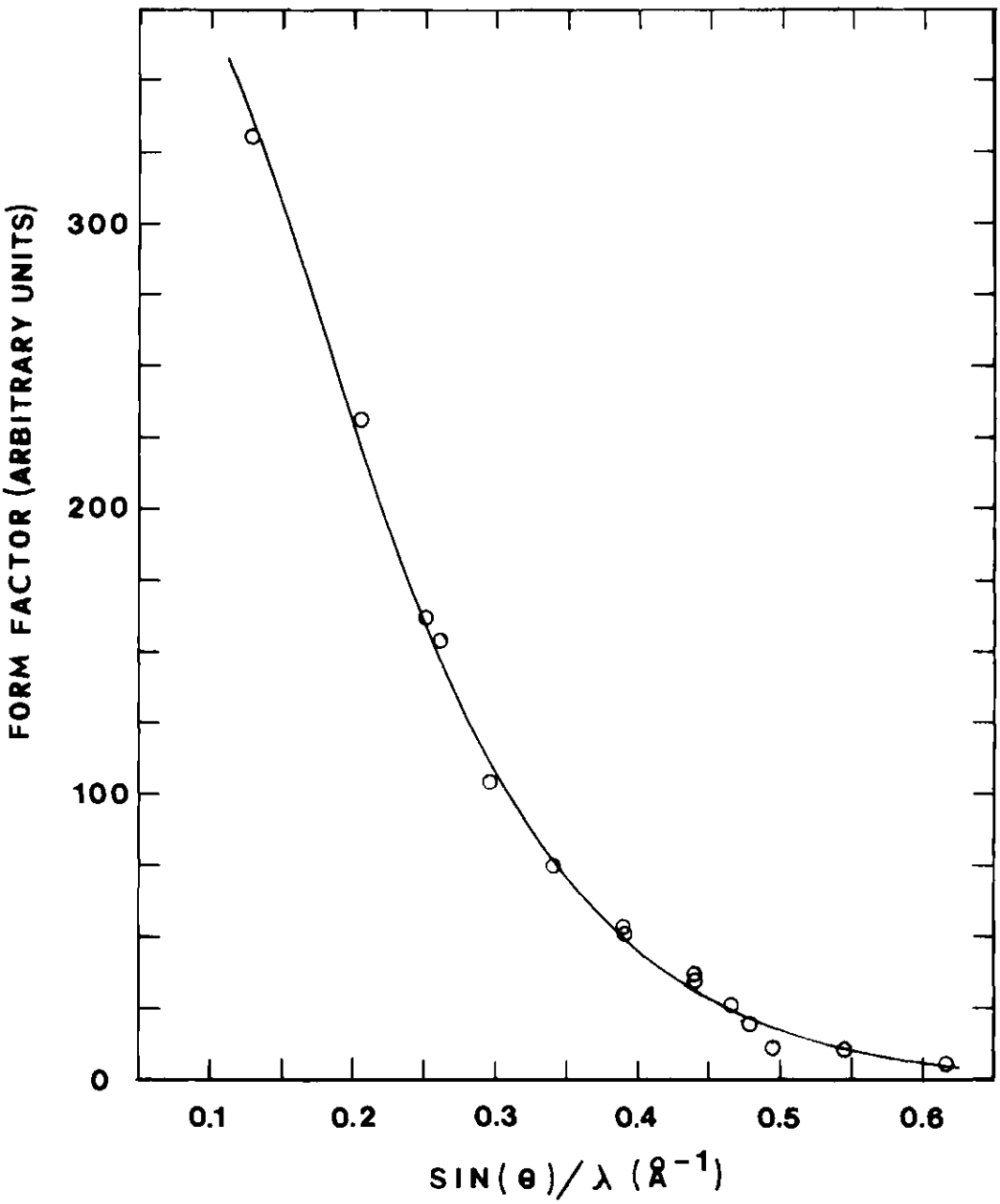

Figure 38. The Magnetic Form Factor of the Fe^{2+} Ion in $FeCO_3$

was so narrow that no horizontal collimators were required for adequate resolution. Two vertical collimators were needed to provide sufficient vertical collimation. A collimator with a total cross-fire angle of 39' was used before the sample, and one with a cross-fire angle of 49' was used after the sample.

The resolution function of this final arrangement was measured at 5.5 K using the (1 0 0) magnetic Bragg peak of the diffuse $FeCO_3$ sample. Figure 39 is a plot of measured constant intensity contours in reciprocal space. These data points were taken with the energy analyzing axis set for elastic scattering. The 1/4, 1/2, and 3/4 maximum intensity contours are shown. The solid line curves in the figure are ellipsoids of the form in Equation (73). The constants in Equation (73) were determined by a least squares procedure. These constants are listed in Table 12, Appendix C.

In addition to measuring the elastic ellipsoid in the scattering plane, ellipsoids were measured with the (1 0 0) reciprocal lattice vector of the $FeCO_3$ crystal tilted out of the scattering plane. The vertical ellipsoid parameter, ZZ, was determined from these data and is also listed in Table 12. Finally, the energy resolution of the diffractometer was measured. The full-width, half maximum of the ellipsoid in the energy direction was 0.45×10^{12} CPS. The parameters listed in Table 12 were used in the folding procedure described in Chapter III to yield the final calculated intensity for comparison with the diffuse neutron data. This comparison is presented in the next section.

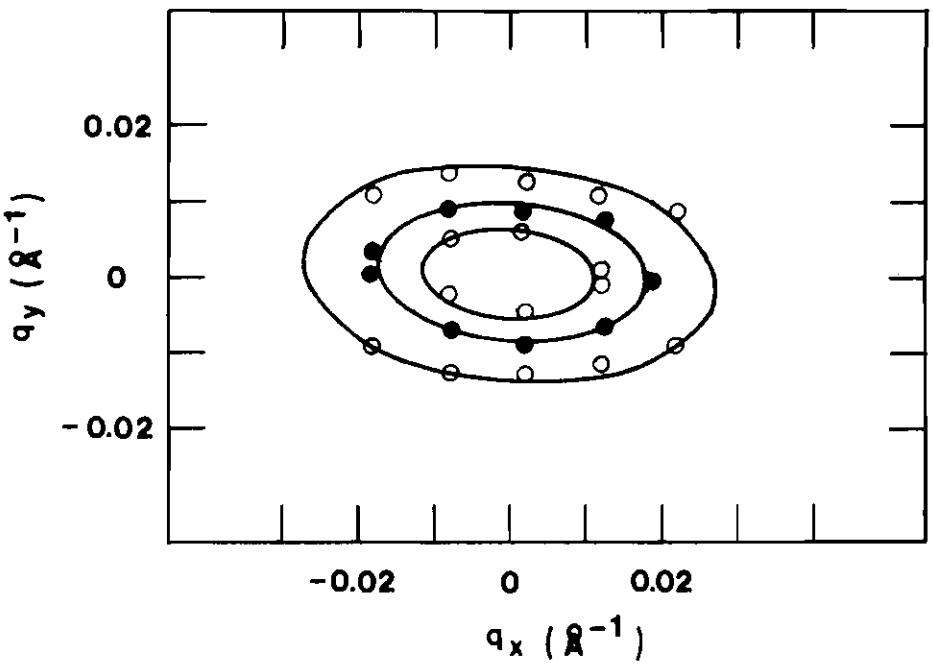

Figure 39. Resolution Function of Experimental Arrangement Used to Collect the Diffuse Data

Comparison with the Diffuse Results

For comparison with the neutron diffuse measurements, the neutron diffraction cross section was calculated using several different functional forms for the spin correlation (see Equation (98)). In every case, the Fourier inversion of the spin correlation coefficients was carried out for radial distances large enough to give a truncation error of less than five percent in the calculated cross section. The truncation error analysis is found in Appendix D.

First, the isotropic Ornstein-Zernike form, Equation (99), was Fourier inverted. The constant in Equation (99) was an average value determined in the comparison with the Monte Carlo results. The Fourier inversion was performed at three temperatures corresponding to the temperatures at which the neutron data were taken. The inversion was performed for diffraction vectors along both neutron scan directions in the (1 0 0) Brillouin zone. Next, the isotropic modified Ornstein-Zernike form, Equation (100), was used in the Fourier inversion at the same temperatures and for the same scans. The value of $\eta = 0.056$ and an average value for the constant C from the Monte Carlo results were used. At all three temperatures and for both scan directions, the cross sections calculated with these spin correlation forms were within a few percentage points of each other.

The anisotropy noted in the Monte Carlo results was treated in two different ways in the cross section calculations. The exact value of the spin correlation coefficients calculated at 42 K for the first 18 shells of neighbors (see Figure 32) were used in a Fourier inversion. For neighbors outside the first 18 shells, the isotropic Ornstein-Zernike form was

used. The cross section was calculated with these spin correlations for both neutron scans and compared with a cross section calculation which used the isotropic Ornstein-Zernike form for all of the spin correlations. These two cross sections were virtually indistinguishable. In the second anisotropic calculation, the modified Ornstein-Zernike form, Equation (100), was assumed. Two different values for the constant C were used. For neighbors in the plane perpendicular to the spin direction, C was set equal to 1.27. For all other neighbors, the value used for C was 1.40. The cross section which used these anisotropic spin correlations was compared with the isotropic modified Ornstein-Zernike spin correlations. Again, these cross sections were everywhere within a few percentage points of each other.

In Figures 40 and 41, the neutron data and the calculated cross sections are compared. The data points are the same points that appear in Figures 29 and 30. The cross section chosen for comparison was the last calculation described. This cross section is based on the anisotropic modified Ornstein-Zernike form of spin correlations. Any of the spin correlation forms just described could have been used, however, since they all produced essentially the same results. Tabulated values of the calculated cross section are listed in Table 11, Appendix C.

The agreement between the neutron data and the calculated cross section is reasonable with one exception. The diffuse neutron scattering in the direction perpendicular to the spin direction was consistently greater than the scattering in the direction parallel to the spin direction. There is about a 20 percent difference in counting rates at all three temperatures for these two different directions. None of the spin correlation forms used produced more than two percent difference in the calculated

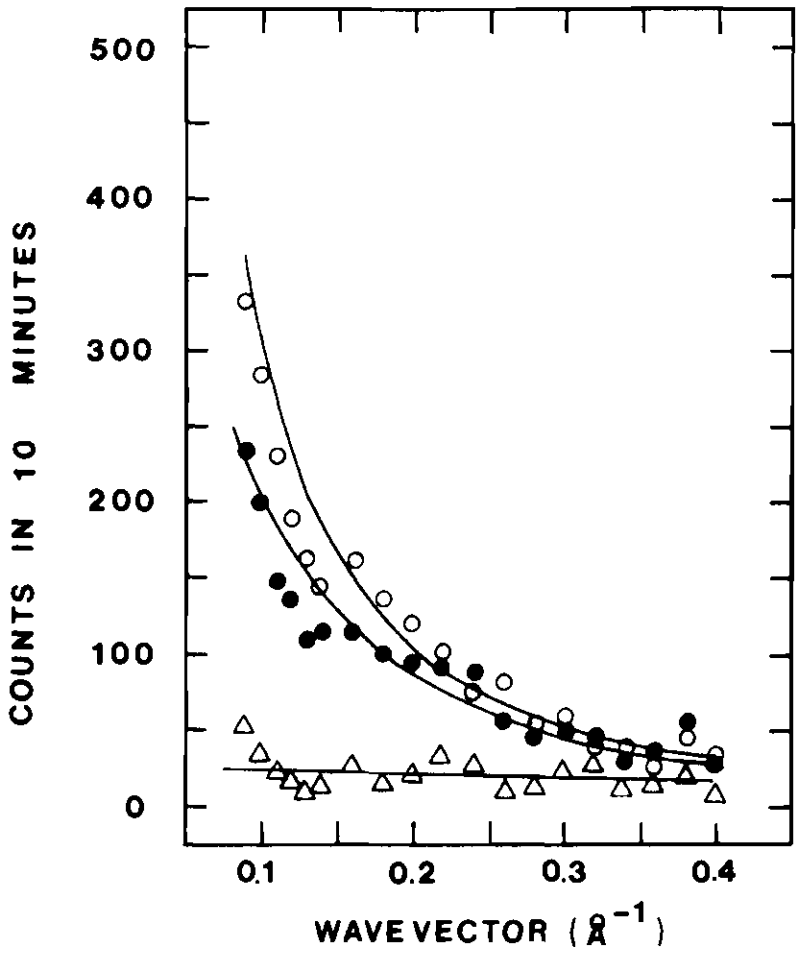

Figure 40. Comparison of the Neutron Data and the Calculated Cross Section in Direction Parallel to Spin Direction

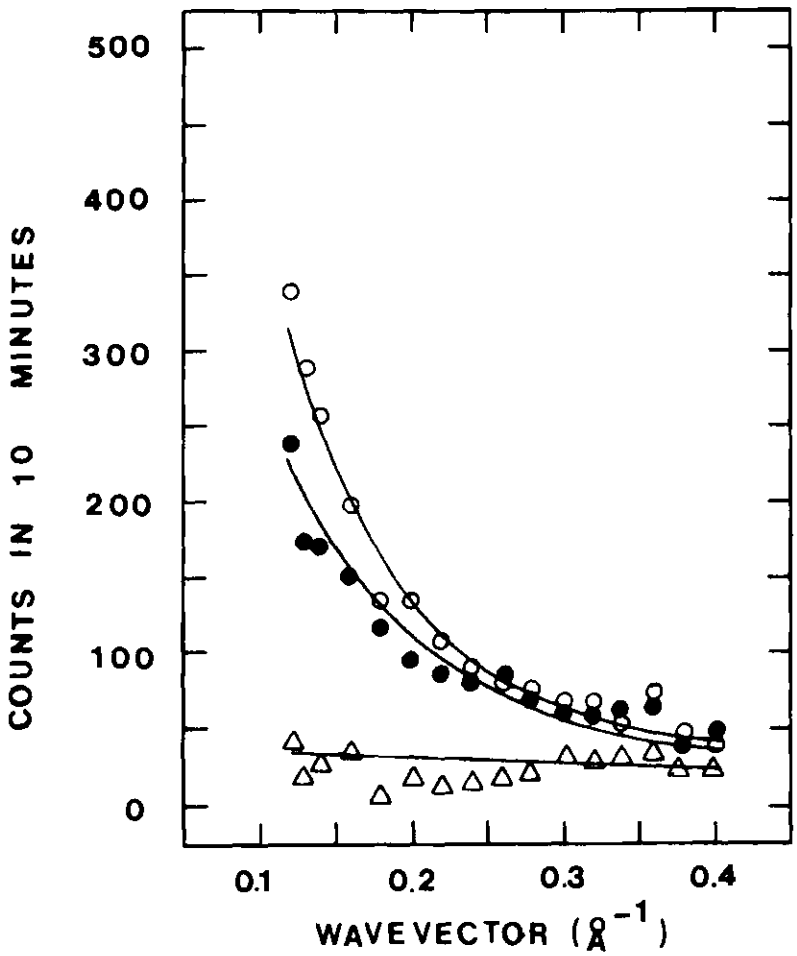

Figure 41. Comparison of the Neutron Data and the Calculated Cross Section in Direction Perpendicular to Spin Direction

cross section for these two scan directions. The agreement between the neutron data and the calculated cross section was obtained by using a different normalization factor in each direction. The normalization factor was determined by a least squares fitting procedure. It is interesting to note, however, that the normalization factor for each direction was the same for all three temperatures.

There is some anisotropy in the magnetic form factor data (see Figure 38). The magnetic form factor could therefore be the source of some of the anisotropy in the diffuse magnetic data. This anisotropy would not appear in the calculated cross section since the isotropic form factor described in this chapter was used in the cross section calculation. Unfortunately, the anisotropy in the Bragg data appears to be too small to account for the 20 percent difference in the diffuse scattering data.

The resolution characteristics of the diffractometer could also introduce anisotropy into the diffuse data. To investigate this possibility, the calculated cross section was folded with ellipsoids of different sizes and shapes, but no ellipsoid that was reasonably consistent with the measured resolution data produced appreciable anisotropy in the calculated cross section. In fact, the folded cross section was very little different from the unfolded cross section. Even when the ellipsoid was doubled in size, the folding process still had a relatively small effect (on the order of five percent) on the shape of the calculated cross section. It is therefore probable that the resolution could have been further relaxed during the diffuse experiment. In this case, the relaxation would have to be accomplished by employing monochromating and analyzing crystals with

relatively broad horizontal mosaic spreads since no horizontal collimators were used in the diffuse experiment. Such crystals should improve the counting rate, and their effect on the data could still be accounted for through the use of the simple folding procedure already described.

CHAPTER V

CONCLUSIONS AND RECOMMENDATIONS

The sublattice magnetization and diffuse magnetic measurements described herein provide further evidence that at low temperatures the magnetic lattice of $FeCO_3$ can be accurately described by an Ising Hamiltonian. The utility and the versatility of the Monte Carlo technique have been demonstrated through its successful application to the $FeCO_3$ magnetic system.

The sublattice magnetization studies were particularly productive. An unambiguous and accurate determination of the temperature dependence of the sublattice magnetization of $FeCO_3$ was made through magnetic neutron Bragg diffraction measurements. Comparison of the Monte Carlo results with the neutron diffraction and other experimental data permitted the determination of both first and second neighbor interaction constants in the Ising Hamiltonian. This study provides the most accurate first neighbor exchange constant and the only quantitative second neighbor exchange constant determinations to date. Monte Carlo and molecular field sublattice magnetization versus temperature curves were compared with the neutron diffraction data. This comparison showed the Monte Carlo results to be clearly superior.

In the Monte Carlo study, the first excited Fe^{2+} ion state was shown to have no effect on the temperature dependence of the sublattice magnetization, a negative but nevertheless, definitive result. In addition, the effect of impurity magnetic ions in $FeCO_3$ was determined. This last calculation gave excellent agreement with the neutron diffraction results.

Two points are worth reiterating here. The first is that, in the impurity Monte Carlo study, all of the input data, impurity ion concentrations, etc., were determined from experimental data other than the neutron diffraction results. There were no free parameters that were adjusted to produce the agreement. The second point is that the impurity calculation was still based on an Ising model. The small differences between the neutron results and the pure Monte Carlo results do not have to be interpreted as a deviation of $FeCO_3$ away from Ising-like behavior. These differences disappear when impurity ions are included in the Monte Carlo calculation. A useful extension of this work would be to repeat the sublattice magnetization measurements on a pure $FeCO_3$ sample and compare these results with the pure Monte Carlo results.

The magnetic diffuse scattering results are more tentative in nature. The Monte Carlo work in this area provides evidence that the behavior of the spin correlations of a three dimensional Ising system does not deviate substantially from the Ornstein-Zernike form over broad temperature and radius vector ranges. It is clear that a very sensitive experiment is required to differentiate between Ornstein-Zernike-like behavior and modified Ornstein-Zernike-like behavior for three dimensional Ising systems. With the present Monte Carlo results, this differentiation cannot be made. However, the accuracy of the Monte Carlo spin correlations is beginning to approach the accuracy that is required to test the two forms. It seems likely, therefore, that enough data for a two dimensional isotropic Ising system could be generated with the Monte Carlo technique to test these two forms in the proper limits.

The diffuse magnetic scattering measurements have a wave vector dependent anisotropy that cannot be obtained from a cross section calculation based on the spin correlations generated in the Monte Carlo study. More diffuse neutron data should be taken to better define the anisotropy that has been noted. These data should be taken with a better sample, assuming one can be found, and the new experiments should be performed at a facility with a higher neutron flux. One interesting feature of the neutron data is the lack of neutron scattering in the direction parallel to the spin direction, both below and above the ordering temperature. This anisotropy is characteristic of Ising systems, and therefore, the neutron diffuse results provide further evidence that the magnetic ground state of $FeCO_3$ is Ising-like.

APPENDIX A

MONTE CARLO EXAMPLE

The model for the Monte Carlo example is a two spin Ising system. Both spins are spin 1/2 particles with only two allowed spin states. The crystal or model states will be represented by the form

(± for site 1, ± for site 2)

where a + stands for a spin up along the axis of quantization, and the - represents a down spin. Thus the four possible crystal states or configurations can be written as

$$(+,+) \equiv \text{State } 1, \tag{A-1}$$
$$(+,-) \equiv \text{State } 2,$$
$$(-,+) \equiv \text{State } 3,$$
$$(-,-) \equiv \text{State } 4.$$

The effective Hamiltonian for the system can be written in the form

$$H = J\sigma_1\sigma_2, \tag{A-2}$$

with $\sigma = \pm 1$. J is assumed to be greater than zero (antiferromagnetic coupling).

Now the vectors and matrices used in the outline of the proof in

the Monte Carlo section will be constructed. The probability vector for this system must contain four elements, one for each crystal state in definitions (A-1). For example, if the model is known to be in State 1 at time t=0 (state in this discussion will mean crystal state, not ion state), then the probability vector will have the form

$$\vec{Y} = \begin{bmatrix} 1 \\ 0 \\ 0 \\ 0 \end{bmatrix} , \tag{A-3}$$

at $t = 0$.

The transition probability matrix P can be constructed by considering the spin flipping process at each model site in turn. The transition matrix for a spin flip at a particular site can be constructed by inspection. The transition matrix for a complete pass through the lattice is then just the product of the matrices for the individual sites. For example, the matrix for the flipping process at site 1 is

$$P_1 = \begin{bmatrix} 0 & 0 & e & 0 \\ 0 & (1-e) & 0 & 1 \\ 1 & 0 & (1-e) & 0 \\ 0 & e & 0 & 0 \end{bmatrix} , \tag{A-4}$$

where

$$e \equiv e^{-\frac{\Delta E}{kT}},$$

$$\Delta E = +\ 2J.$$

The matrix just exhibited can be checked by examining the state to state transitions it predicts. For instance, if the system is known to be in state 1 at time t = 0, then the vector $\vec{Y}$ of Equation (A-3) can be multiplied by P_1 to give the probability of finding the system in any one of the four configurations after the spin flipping process at site one has been completed. The result is

$$\begin{bmatrix} 0 & 0 & e & 0 \\ 0 & (1-e) & 0 & 1 \\ 1 & 0 & (1-e) & 0 \\ 0 & e & 0 & 0 \end{bmatrix} \begin{bmatrix} 1 \\ 0 \\ 0 \\ 0 \end{bmatrix} = \begin{bmatrix} 0 \\ 0 \\ 1 \\ 0 \end{bmatrix}. \tag{A-5}$$

But this is just the result that the spin flipping process must produce. State 1 is a high energy configuration (recall $J > 0$) and so the spin flipping process will turn the spin at site 1 down to give state 3 with probability one.

The corresponding matrix at site 2, P_2, is

$$P_2 = \begin{bmatrix} 0 & e & 0 & 0 \\ 1 & (1-e) & 0 & 0 \\ 0 & 0 & (1-e) & 1 \\ 0 & 0 & e & 0 \end{bmatrix}. \tag{A-6}$$

The product of P_1 and P_2 gives P for this case since there are two spin sites. The result is

$$P = \begin{bmatrix} 0 & e(1-e) & 0 & e \\ 0 & (1-e)^2 & e & (1-e) \\ (1-e) & e & (1-e)^2 & 0 \\ e & 0 & e(1-e) & 0 \end{bmatrix}. \qquad \text{(A-7)}$$

Now the first assertion in the Monte Carlo section is that $\sum_u P_{uu'} = 1$. For $u' = 1$ in the matrix P just constructed, $\sum_u P_{uu'} = 0+0+(1-e)+e = 1$; and for $u' = 2$, $\sum_u P_{uu'} = e(1-e)+(1-e)^2+e+0 = 1$. The results for $u' = 3$, 4 must clearly be the same. The second assertion to be demonstrated is that, for some integer t, all of the elements of P^t (P to the power t) are greater than zero. For the matrix P,

$$P^2 = \begin{bmatrix} e^2 & e(1-e)^3 & 2e^2(1-e) & e(1-e)^2 \\ 2e(1-e) & e^2+(1-e)^4 & 3e(1-e)^2 & (1-e)^3 \\ (1-e)^3 & 3e(1-e)^2 & e^2+(1-e)^4 & 2e(1-e) \\ e(1-e)^2 & 2e^2(1-e) & e^2(1-e)^3 & e^2 \end{bmatrix}. \qquad \text{(A-8)}$$

So, excluding the limiting cases $T = 0$ and $T = \infty$, all of the elements of P^2 are greater than zero.

Another assertion is that the vector $\vec{Y}_E$, given for this model by

$$\vec{Y}_E = \begin{bmatrix} e^{-\frac{J}{kT}} \\ e^{+\frac{J}{kT}} \\ e^{+\frac{J}{kT}} \\ e^{-\frac{J}{kT}} \end{bmatrix} \qquad \text{(A-9)}$$

is an eigenvector of P with eigenvalue one.

$$\begin{bmatrix} 0 & e(1-e) & 0 & e \\ 0 & (1-e)^2 & e & (1-e) \\ (1-e) & e & (1-e)^2 & 0 \\ e & 0 & e(1-e) & 0 \end{bmatrix} \begin{bmatrix} e^{-\frac{J}{kT}} \\ e^{\frac{J}{kT}} \\ e^{\frac{J}{kT}} \\ e^{-\frac{J}{kT}} \end{bmatrix} \tag{A-10}$$

$$\begin{bmatrix} e^{-\frac{2J}{kT}} e^{\frac{J}{kT}} - e^{2\frac{2J}{kT}} e^{-\frac{2J}{kT}} e^{\frac{J}{kT}} + e^{-\frac{2J}{kT}} e^{-\frac{J}{kT}} \\ e^{\frac{J}{kT}}(1-2e+e^2) + e^{-\frac{2J}{kT}} e^{\frac{J}{kT}} + e^{-\frac{J}{kT}} - e^{-\frac{2J}{kT}} e^{-\frac{J}{kT}} \\ e^{-\frac{J}{kT}} - e^{-\frac{2J}{kT}} e^{-\frac{J}{kT}} + e^{-\frac{2J}{kT}} e^{\frac{J}{kT}} + (1-2e+e^2) e^{\frac{J}{kT}} \\ e^{-\frac{2J}{kT}} e^{-\frac{J}{kT}} + e^{-\frac{2J}{kT}} e^{\frac{J}{kT}} - e^{-\frac{2J}{kT}} e^{-\frac{2J}{kT}} e^{\frac{J}{kT}} \end{bmatrix}$$

$$= \begin{bmatrix} e^{-\frac{J}{kT}} \\ e^{\frac{J}{kT}} \\ e^{\frac{J}{kT}} \\ e^{-\frac{J}{kT}} \end{bmatrix} = 1 \cdot \vec{Y}_E .$$

The multiplication yields the desired result. To find the remaining eigenvalues for the matrix P, solutions to the equation

$$P\vec{Y} = \lambda\vec{Y} \tag{A-11}$$

or

$$(P-\lambda I)\vec{Y} = 0$$

where I is the identity matrix, must be found. The λ values are the zeros of the secular equation (determinant of the matrix $[P-\lambda I]$). Expansion of this determinant gives

$$\lambda^4 - 2(1-e)^2\lambda^3 + [(1-e)^4-2e^2]\lambda^2 \qquad \text{(A-12)}$$

$$- 2e^2(1-e)^2\lambda - e^4 = 0.$$

Equation (A-12) can be factored into the form

$$(\lambda-1)(\lambda-e^2)[\lambda^2 + (-e^2+4e-1)\lambda + e^2] = 0. \qquad \text{(A-13)}$$

The eigenvalues of Equation (A-11) must therefore be

$$\lambda_1 = 1, \qquad \text{(A-14)}$$

$$\lambda_2 = e^2,$$

$$\lambda_3 = \frac{e^2 - 4e + 1 + [(e^2-4e+1)^2-4e^2]^{1/2}}{2},$$

$$\lambda_4 = \frac{e^2 - 4e + 1 - [(e^2-4e+1)^2-4e^2]^{1/2}}{2},$$

The absolute value of λ_2 is clearly less than 1. To demonstrate that the moduli of λ_3 and λ_4 are less than one requires some care. The function within the brackets in Equation (A-14) has a zero in the interval $0 < e < 1$ at the point $e = 3 - 2\sqrt{2} \approx 0.172$. For $0 < e < 0.172$, the function within the brackets is positive and both λ_3 and λ_4 are real. For

$0.172 < e < 1$, the function within the brackets is negative, and λ_3 and λ_4 are complex. For the interval $0 < e < 0.172$, both $e^2 - 4e+1$ and the function under the radical are monotone decreasing functions and fall in the intervals

$$6 - 4\sqrt{2} \approx 0.344 < e^2 - 4e+1 < 1 \qquad \text{(A-15)}$$

$$0 < (e^2-4e+1)^2 - 4e^2 < 1.$$

The triangle inequality can now be used for e values in this range to give

$$|\lambda| \leq \frac{|e^2 - 4e + 1| + |[(e^2-4e+1)^2-4e^2]^{1/2}|}{2} < \frac{1 + 1}{2} = 1 \qquad \text{(A-16)}$$

for both λ_3 and λ_4. The definition for the modulus of a complex number must be used in the range $0.172 < e < 1$. This definition is

$$|z| = (x^2+y^2)^{1/2} \qquad \text{(A-17)}$$

where

$$z = x+iy.$$

Since the function within the brackets is negative in this range, λ_3 can be written in the form of Equation (A-17) by rewriting (A-14) as

$$\lambda_3 = \frac{e^2 - 4e + 1 + i[4e^2 - (e^2-4e+1)^2]^{1/2}}{2}.$$

The moduli for both λ_3 and λ_4 are the same in this e range and by Equation (A-17) are equal to

$$\left[(e^2-4e+1)^2 + 4e^2 - (e^2-4e+1)^2 \right]^{1/2} = \frac{2e}{2} = e \qquad \text{(A-18)}$$

But since e is less than one in this range, the moduli of λ_3 and λ_4 are less than one in this range too.

APPENDIX B

RESOLUTION FUNCTION EXPRESSIONS

Cooper and Nathans[41,42] treat the neutron diffraction resolution function problem by assuming that the transmission functions of the collimators and mosaic spreads of the crystals are all Gaussian. For example, the mosaic spread of the monochromator is assumed to be proportional to $e^{-\frac{1}{2}\left(\frac{\gamma_m}{\alpha_m}\right)^2}$. In this expression, γ_m is the angle of rotation of the monochromator away from its optimum orientation. With these assumptions, Cooper and Nathans find that the resolution function, R, can be written in the product form $R_H R_V$ where R_H is the horizontal resolution function and R_V is the vertical resolution function. The functions R_H and R_V are different for double axis and triple axis diffractometers. The double axis case will be considered first followed by the triple axis case.

For a double axis diffractometer, the functions R_H and R_V are given by

$$R_H \propto e^{-\left(L - \frac{m^2}{4N}\right)} \tag{B-1}$$

$$R_V \propto e^{-\frac{1}{2}\left(F'^2 - \frac{G'^2}{E'}\right)}$$

where

$$L = \frac{E^2}{2K^2}\left(\frac{1}{\alpha_m^2} + \frac{1}{\alpha_0^2} + \frac{1}{\alpha_1^2}\right) + \frac{F^2}{2K^2\alpha_2^2} \quad , \tag{B-2}$$

$$M = -\frac{E}{K^2}\left(\frac{G}{\alpha_m^2} + \frac{H}{\alpha_0^2} + \frac{C}{\alpha_1^2}\right) + \frac{F^2 C}{K^2\alpha_2^2} \quad ,$$

$$N = \frac{1}{2K^2}\left(\frac{G^2}{\alpha_m^2} + \frac{H^2}{\alpha_0^2} + \frac{C^2}{\alpha_1^2} + \frac{C^2}{\alpha_2^2}\right) \quad ,$$

$$E = -\frac{q_X}{2\cos(\theta_s)} - \frac{q_Y}{2\sin(\theta_s)} \quad ,$$

$$F = \frac{q_X}{2\cos(\theta_s)} - \frac{q_Y}{2\sin(\theta_s)} \quad ,$$

$$G = \tan(\theta_s) - \tan(\theta_m) \quad ,$$

$$H = \tan(\theta_s) - 2\tan(\theta_m) \quad ,$$

$$F' = \frac{q_Z}{K_i\beta_2} \quad , \qquad G' = \frac{q_Z}{K_i\beta_2^2} \quad ,$$

$$E' = \frac{1}{\beta_1^2} + \frac{1}{\beta_2^2} + \frac{1}{[2\sin(\theta_m)\beta_m]^2 + \beta_0^2} \quad .$$

The quantities in these expressions are defined in Figures 6 and 7.

The function defined by equations (B-1) and (B-2) can be manipulated

into more convenient forms. For the double axis case R_H can be written as

$$R_H \propto e^{-(XXq_x^2 + XYq_xq_y + YYq_y^2)} \tag{B-3}$$

where

$$XX = \frac{1}{8K^2}\frac{1}{\cos^2(\theta_s)}\left(C_1 + C_2 - \frac{C_3^2}{C_5} - \frac{2C_3C_4}{C_5} - \frac{C_4^2}{C_5}\right), \tag{B-4}$$

$$XY = \frac{1}{8K^2}\frac{2}{\sin(\theta_s)\cos(\theta_s)}\left(C_1 - C_2 - \frac{C_3^2}{C_5} + \frac{C_4^2}{C_5}\right),$$

$$YY = \frac{1}{8K^2}\frac{2}{\sin^2(\theta_s)}\left(C_1 + C_2 - \frac{C_3^2}{C_5} + 2\frac{C_3C_4}{C_5} - \frac{C_4^2}{C_5}\right),$$

$$C_1 = \frac{1}{\alpha_m^2} + \frac{1}{\alpha_0^2} + \frac{1}{\alpha_1^2}, \qquad C_2 = \frac{1}{\alpha_2^2},$$

$$C_3 = \frac{D_1}{\alpha_m^2} + \frac{D_2}{\alpha_0^2} + \frac{D_3}{\alpha_1^2}, \qquad C_4 = \frac{D_3}{\alpha_2^2},$$

$$C_5 = \frac{D_1^2}{\alpha_m^2} + \frac{D_2^2}{\alpha_0^2} + \frac{D_3^2}{\alpha_1^2} + \frac{D_3^2}{\alpha_2^2}$$

and

$$D_1 = \tan(\theta_s) - \tan(\theta_m), \tag{B-5}$$

$$D_2 = \tan(\theta_s) - 2\tan(\theta_m),$$

$$D_3 = \tan(\theta_s).$$

The function R_V can be written as

$$R_V = e^{-ZZq_z^2} \tag{B-6}$$

where

$$ZZ = \frac{1}{2K_i^2}\left\{\frac{1}{\beta_2^2} + \frac{\beta_1^2[4\sin^2(\theta_m)\beta_m^2+\beta_0^2]}{\beta_2^2[(\beta_2^2+\beta_1^2)(4\sin^2(\theta_m)\beta_m^2+\beta_0^2) + \beta_1^2\beta_2^2]}\right\} \tag{B-7}$$

For the triple axis case, the functions derived by Cooper and Nathans are

$$R_H \propto e^{-\frac{1}{2}\left(Z - \frac{Y^2}{X}\right)}, \tag{B-8}$$

$$R_V \propto e^{-\frac{1}{2}\left[\frac{NL}{\left(\frac{K_i}{K_f}\right)^{N+L}}\right]\frac{q_z^2}{K_f^2}},$$

where

$$X = \frac{(A+2G)^2}{\alpha_0^2} + \frac{(A+G)}{\alpha_m^2} + \frac{A^2}{\alpha_1^2} + \frac{B^2}{\alpha_2^2} + \frac{(B-RH)^2}{\alpha_a^2} + \frac{(B-2RH)^2}{\alpha_3^2} \tag{B-9}$$

$$Y = \frac{(A+2G)C}{\alpha_0^2} + \frac{(A+G)C}{\alpha_m^2} + \frac{AC}{\alpha_1^2} + \frac{BD}{\alpha_2^2} + \frac{(B-RH)(D+FH)}{\alpha_a^2} + \frac{(B-2RH)(D+2FH)}{\alpha_3^2},$$

$$Z = \frac{C^2}{\alpha_0^2} + \frac{C^2}{\alpha_m^2} + \frac{C^2}{\alpha_1^2} + \frac{D^2}{\alpha_2^2} + \frac{(D+FH)^2}{\alpha_a^2} + \frac{(D+2FH)}{\alpha_3^2},$$

$$A = \frac{\left[\cos(2\theta_s) - \frac{K_i}{K_f}\right]}{\sin(2\theta_s)K_i} , \qquad B = \frac{\left[1 - \cos(2\theta_s)\frac{K_i}{K_f}\right]}{\sin(2\theta_s)K_f} ,$$

$$C = \frac{1}{\sin(2\theta_s)K_i}\left[\frac{m}{\hbar K_f}\Delta\omega + \cos(2\theta_s+\phi)q_x - \sin(2\theta_s+\phi)q_y\right] ,$$

$$D = \frac{1}{\sin(2\theta_s)K_f}\left[\cos(2\theta_s)\frac{m}{\hbar K_f}\Delta\omega + \cos(\phi)q_x - \sin(\phi)q_y\right] ,$$

$$F = \frac{m}{\hbar K_f}\Delta\omega , \qquad G = \frac{\tan(\theta_m)}{K_i} , \qquad H = \frac{\tan(\theta_a)}{\hbar K_f} ,$$

$$L = \frac{1}{\beta_1^2} + \frac{1}{\beta_0^2 + 4\sin^2(\theta_m)\beta_m^2} ,$$

$$N = \frac{1}{\beta_2^2} + \frac{1}{\beta_3^2 + 4\sin^2(\theta_a)\beta_a^2} ,$$

$$R = \frac{K_i}{K_f} .$$

In equations (B-9), m is the mass of a neutron, $\hbar$ is Planck's constant, and the other quantities are defined in Figures 6 and 7.

This resolution function for a triple axis diffractometer can again be written in a more convenient form. The form is

$$R \propto e^{-[XXq_x^2+YYq_y^2+EE\Delta\omega^2+XYq_xq_y+EXq_x\Delta\omega+EYq_y\Delta\omega+ZZq_z^2]} \tag{B-10}$$

where

$$EE = \frac{1}{2S^2}\left(\frac{m}{\hbar K_f}\right)\left[\frac{K_1}{K_i^2} + \frac{K_2}{K_f^2}C^2 + \frac{K_3}{K_f^2}S^2 - \frac{K_4}{K_iK_f}C - \frac{K_5}{K_iK_f}S + \frac{K_6}{K_f^2}SC\right], \tag{B-11}$$

$$XX = \frac{1}{2S^2}\left[\frac{K_1}{K_i^2}\cos^2(2\theta_s+\phi) + \frac{K_2}{K_f^2}\cos(\phi) - \frac{K_4}{K_iK_f}\cos(\phi)\cos(2\theta_s+\phi)\right],$$

$$YY = \frac{1}{2S^2}\left[\frac{K_1}{K_i^2}\sin^2(2\theta_s+\phi) + \frac{K_2}{K_f^2}\sin^2(\phi) - \frac{K_4}{K_iK_f}\sin(\phi)\sin(2\theta_s+\phi)\right],$$

$$XY = \frac{1}{2S^2}\left\{-2\frac{K_1}{K_i^2}\cos(2\theta_s+\phi)\sin(2\theta_s+\phi) - 2\frac{K_2}{K_f^2}\cos(\phi)\sin(\phi) + \frac{K_4}{K_iK_f}[\sin(2\theta_s+\phi)\cos(\phi)+\cos(2\theta_s+\phi)\sin(\phi)]\right\},$$

$$EX = \frac{1}{2S^2}\left(\frac{m}{\hbar K_f}\right)\left\{2\frac{K_1}{K_i^2}\cos(2\theta_s+\phi) + 2\frac{K_2}{K_f^2}\cos(2\theta_s)\cos(\phi) - \frac{K_4}{K_iK_f}[\cos(2\theta_s+\phi)\cos(2\theta_s)+\cos(\phi)] - \frac{K_5}{K_iK_f}S\cos(2\theta_s+\phi) + \frac{K_6}{K_f^2}S\cos(\phi)\right\},$$

$$EY = \frac{1}{2S^2}\left(\frac{m}{\hbar K_f}\right)\left\{-2\frac{K_1}{K_i^2}\sin(2\theta_s+\phi) - 2\frac{K_2}{K_f^2}\cos(2\theta_s)\sin(\phi)\right.$$

$$+\frac{K_4}{K_iK_f}\left[\sin(2\theta+\phi)\cos(2\theta_s)+\sin(\phi)\right]$$

$$\left.+\frac{K_5}{K_iK_f}S\sin(2\theta_s+\phi) - \frac{K_6}{K_f^2}S\sin(\phi)\right\},$$

$$ZZ = \frac{1}{2K_f^2}\left(\frac{C_7C_8}{R^2C_8+C_7}\right),$$

and

$$R = \frac{K_i}{K_f}, \qquad C = \cos(2\theta_s), \qquad S = \sin(2\theta_s)$$

and

$$K_1 = C_1 - \frac{1}{X}\frac{1}{K_i^2}\left[C_1\frac{(C-R)}{S} + C_5\frac{M}{2}\right]^2,$$

$$K_2 = C_2 - \frac{1}{X}\frac{1}{K_f^2}\left[C_2\frac{(1-RC)}{S} - C_3 R\frac{A}{2}\right]^2,$$

$$K_3 = C_4A^2 - \frac{1}{X}\frac{1}{K_f^2}\left[C_3\frac{(1-RC)}{2S}A - C_4 R A^2\right]^2,$$

$$K_4 = \frac{2}{X}\frac{1}{K_iK_f}\left[C_1\frac{(C-R)}{S} + C_5\frac{M}{2}\right]\left[C_2\frac{(1-RC)}{S} - C_3 R\frac{A}{2}\right],$$

$$K_5 = \frac{2}{X}\frac{1}{K_iK_f}\left[C_1\frac{(C-R)}{S} + C_5\frac{M}{2}\right]\left[C_3\frac{(1-RC)}{2S}A - C_4 R A^2\right],$$

$$K_6 = C_3A - \frac{2}{X}\frac{1}{K_f^2}\left[C_2\frac{(1-RC)}{S} - C_3 R\frac{A}{2}\right]\left[C_3\frac{(1-RC)}{2S}A - C_4 R A^2\right],$$

$$A = \tan(\theta_a) , \qquad M = \tan(\theta_m) ,$$

$$X = \frac{C_1}{K_i^2}\frac{(C-R)^2}{S^2} + \frac{C_2}{K_f^2}\frac{(1-RC)^2}{S^2} + C_5\frac{m}{K_i^2}\frac{(C-R)}{S} - C_6\frac{m^2}{K_i^2} - C_3\frac{RA}{K_f^2}\frac{(1-RC)}{S} + C_4\frac{R^2A^2}{K_f^2} ,$$

$$C_1 = \frac{1}{\alpha_0^2} + \frac{1}{\alpha_m^2} + \frac{1}{\alpha_1^2} , \qquad C_2 = \frac{1}{\alpha_2^2} + \frac{1}{\alpha_a^2} + \frac{1}{\alpha_3^2} , \qquad C_3 = \frac{2}{\alpha_a^2} + \frac{4}{\alpha_3^2} ,$$

$$C_4 = \frac{1}{\alpha_a^2} + \frac{4}{\alpha_3^2} , \qquad C_5 = \frac{4}{\alpha_0^2} + \frac{2}{\alpha_m^2} , \qquad C_6 = \frac{4}{\alpha_0^2} + \frac{1}{\alpha_m^2} ,$$

$$C_7 = \frac{1}{\beta_1^2} + \frac{1}{\beta_0^2 + 4\sin^2(\theta_m)\beta_m^2} ,$$

$$C_8 = \frac{1}{\beta_2^2} + \frac{1}{\beta_3^2 + 4\sin^2(\theta_a)\beta_a^2} .$$

If the energy analyzing crystal is set to accept only neutrons that are elastically scattered by the sample, the resolution function has the form

$$R \quad e^{-[XXq_x^2+YYq_y^2+XYq_xq_y+ZZq_z^2]} . \qquad \text{(B-12)}$$

For this elastic triple axis case,

$$XX = \frac{1}{8\cos^2(\theta_s)K_i^2}\left\{C_1 + C_2 - \frac{1}{X}\frac{1}{K_i^2}\left[C_5\frac{M}{2} + C_3\frac{A}{2} - \tan(\theta_s)(C_1+C_2)\right]^2\right\}, \quad \text{(B-13)}$$

$$YY = \frac{1}{8\cos^2(\theta_s)K_i^2}\left\{C_1 + C_2 - \frac{1}{X}\frac{1}{K_i^2}\left[(C_2-C_1)\tan(\theta_s)+C_5\frac{M}{2} - C_3\frac{A}{2}\right]^2\right\},$$

$$XY = \frac{2}{8\sin(\theta_s)\cos(\theta_s)K_i^2}\left\{C_1 - C_2 - \frac{1}{X}\frac{1}{K_i^2}\left[C_3\frac{A}{2} + C_5\frac{M}{2} - (C_1+C_2)\tan(\theta_s)\right]\times\right.$$

$$\left.\times\left[(C_2-C_1)\tan(\theta_s) + C_5\frac{M}{2} - C_3\frac{A}{2}\right]\right\},$$

$$ZZ = \frac{1}{2K_i^2}\frac{C_7C_8}{C_7+C_8},$$

$$X = \frac{1}{K_i^2}\left[(C_1+C_2)\tan^2(\theta_s) - (C_5M+C_3A)\tan(\theta_s) + C_4A^2 + C_6M^2\right].$$

In equations (B-13), the definitions of A, M, and the C's are the same ones given in equations (B-11).

APPENDIX C

DATA TABLES

Table 3. Extinction Correction Data

Temperature[1] (^{o}K)	8.0	13.0	19.0	23.0	28.0	31.0	33.0	37.0
Measured intensity[2]								
(100) counts $\times 10^{-3}$	454.8	444.9	437.4	403.8	346.8	283.2	230.5	88.5
(300) counts $\times 10^{-3}$	33.7	33.2	31.5	29.2	24.2	19.2	15.3	5.8
(144) counts $\times 10^{-3}$	7.3	7.2	7.0	6.0	5.1	4.0	3.0	1.7
Normalized intensity I^{*}								
(100)	1.01	0.99	0.97	0.90	0.77	0.63	0.51	0.20
(300)	1.00	0.99	0.94	0.87	0.72	0.58	0.46	0.17
(144)	1.01	0.99	0.96	0.83	0.70	0.56	0.42	0.23
Extinction corrected I^{*}								
(100)	1.01	0.99	0.96	0.87	0.72	0.57	0.45	0.16
(300)	1.00	0.99	0.94	0.87	0.72	0.57	0.46	0.17
(144)	1.01	0.99	0.96	0.83	0.70	0.56	0.42	0.23

(1) Approximate temperature -- see text.

(2) Intensity corrected for instrumental and sample background scattering.

Table 4. Neutron Sublattice Magnetization Data

Temperature (°K)	Order of Collection	Measured[1] Intensity I(T) (counts × 10^{-3})	$[I(T) \times 10^{-4}]^{\frac{1}{0.624}}$
6.50 ± 0.23	26	63.98 ± 0.88	18.34 ± 0.39
6.60 ± 0.23	16	63.90 ± 0.88	18.30 ± 0.39
9.90 ± 0.21	17	63.76 ± 0.87	18.20 ± 0.39
12.40 ± 0.21	27	64.16 ± 0.87	18.42 ± 0.38
12.50 ± 0.21	18	62.97 ± 0.87	17.89 ± 0.39
14.90 ± 0.21	28	64.46 ± 0.87	18.55 ± 0.39
15.10 ± 0.21	8	63.94 ± 0.87	18.32 ± 0.39
17.40 ± 0.21	19	61.97 ± 0.87	17.45 ± 0.38
20.20 ± 0.12	1	61.71 ± 0.86	17.33 ± 0.37
20.90 ± 0.12	20	60.33 ± 0.86	16.72 ± 0.37
22.70 ± 0.12	9	58.64 ± 0.85	16.00 ± 0.36
22.70 ± 0.12	29	59.75 ± 0.85	16.48 ± 0.36
24.20 ± 0.12	30	57.68 ± 0.84	15.59 ± 0.36
25.30 ± 0.12	2	56.41 ± 0.82	15.05 ± 0.35
26.50 ± 0.12	31	53.90 ± 0.82	14.02 ± 0.34
27.40 ± 0.12	10	51.32 ± 0.81	12.98 ± 0.32
28.80 ± 0.10	32	49.28 ± 0.81	12.18 ± 0.31
29.90 ± 0.10	3	45.38 ± 0.77	10.71 ± 0.28
30.90 ± 0.10	11	42.55 ± 0.75	9.68 ± 0.27
32.60 ± 0.10	4	36.09 ± 0.72	7.48 ± 0.23
33.70 ± 0.10	12	31.60 ± 0.70	6.07 ± 0.21
35.00 ± 0.10	5	25.83 ± 0.67	4.43 ± 0.18
35.80 ± 0.10	21	20.58 ± 0.65	3.10 ± 0.15
36.10 ± 0.10	13	19.05 ± 0.64	2.74 ± 0.14
36.50 ± 0.10	22	16.89 ± 0.60	2.27 ± 0.12
37.00 ± 0.10	23	11.98 ± 0.59	1.32 ± 0.10
37.60 ± 0.10	6	9.57 ± 0.58	0.93 ± 0.09
38.00 ± 0.10	24	4.86 ± 0.58	0.32 ± 0.06
38.80 ± 0.10	14	3.06 ± 0.55	0.16 ± 0.04
39.00 ± 0.10	25	2.41 ± 0.55	0.11 ± 0.04
40.00 ± 0.10	7	1.89 ± 0.55	0.07 ± 0.03
41.30 ± 0.10	15	1.29 ± 0.55	0.04 ± 0.03

(1) Data corrected for extinction, sample, and instrumental background scattering.

Table 5. Neutron Diffraction Reduced Variables

Temperature (^{o}K)	T/T_N (T_N = 38.0 ^{o}K)	$I_R(T)$ $I(T=0) = 63.75 \times 10^3$	$\langle \sigma(T) \rangle_R$
6.50 ± 0.23	0.171 ± 0.006	1.003 ± 0.015	1.002 ± 0.008
6.60 ± 0.23	0.174 ± 0.006	1.001 ± 0.015	1.001 ± 0.008
9.90 ± 0.21	0.261 ± 0.006	0.999 ± 0.015	1.000 ± 0.008
12.40 ± 0.21	0.326 ± 0.006	1.006 ± 0.015	1.003 ± 0.008
12.50 ± 0.21	0.329 ± 0.006	0.987 ± 0.015	0.994 ± 0.008
14.90 ± 0.21	0.392 ± 0.006	1.010 ± 0.015	1.005 ± 0.008
15.10 ± 0.21	0.397 ± 0.006	1.002 ± 0.015	1.001 ± 0.008
17.40 ± 0.21	0.458 ± 0.007	0.971 ± 0.015	0.985 ± 0.008
20.20 ± 0.12	0.534 ± 0.007	0.967 ± 0.015	0.983 ± 0.008
20.90 ± 0.12	0.550 ± 0.007	0.946 ± 0.015	0.973 ± 0.008
22.70 ± 0.12	0.597 ± 0.007	0.919 ± 0.015	0.959 ± 0.008
22.70 ± 0.12	0.597 ± 0.007	0.937 ± 0.015	0.968 ± 0.008
24.20 ± 0.12	0.637 ± 0.007	0.904 ± 0.015	0.951 ± 0.008
25.30 ± 0.12	0.666 ± 0.007	0.884 ± 0.015	0.940 ± 0.008
26.50 ± 0.12	0.697 ± 0.007	0.845 ± 0.014	0.919 ± 0.008
27.40 ± 0.12	0.721 ± 0.007	0.804 ± 0.014	0.897 ± 0.008
28.80 ± 0.10	0.758 ± 0.007	0.773 ± 0.014	0.879 ± 0.008
29.90 ± 0.10	0.787 ± 0.007	0.711 ± 0.013	0.843 ± 0.008
30.90 ± 0.10	0.813 ± 0.007	0.667 ± 0.013	0.817 ± 0.008
32.60 ± 0.10	0.858 ± 0.007	0.566 ± 0.012	0.752 ± 0.008
33.70 ± 0.10	0.887 ± 0.007	0.495 ± 0.012	0.704 ± 0.009
35.00 ± 0.10	0.921 ± 0.008	0.405 ± 0.011	0.636 ± 0.009
35.80 ± 0.10	0.942 ± 0.008	0.323 ± 0.011	0.568 ± 0.009
36.10 ± 0.10	0.951 ± 0.008	0.299 ± 0.010	0.547 ± 0.009
36.50 ± 0.10	0.959 ± 0.008	0.265 ± 0.010	0.515 ± 0.010
37.00 ± 0.10	0.974 ± 0.008	0.188 ± 0.009	0.434 ± 0.012
37.60 ± 0.10	0.988 ± 0.008	0.150 ± 0.009	0.387 ± 0.016
38.00 ± 0.10	1.000 ± 0.008	0.0 ± 0.009	0.0 ± 0.018

Table 6. Data from the Monte Carlo Calculations with No Impurity Content

Lattice Size	Energy 4×4×12	Energy 6×6×18	Energy 8×8×24	Sublattice Magnetization 4×4×12	Sublattice Magnetization 6×6×18	Sublattice Magnetization 8×8×24
Results for K_{NN} = 5.86		K_{NNN} = -2.35				
Temp.						
25.0	-89.1	-89.1		0.949	0.949	
30.0	-78.0	-76.6	-77.3	0.882	0.874	0.878
32.0	-69.7	-70.2	-70.5	0.824	0.828	0.831
34.0	-63.1	-62.2	-62.8	0.768	0.767	0.773
35.0	-58.6	-57.7	-57.8	0.720	0.730	0.730
36.0	-48.2	-53.2	-53.2	0.600	0.689	0.688
37.0	-47.6	-46.4	-46.8	0.625	0.618	0.622
38.0	-41.6	-38.0	-41.8	0.532	0.492	0.557
39.0	-36.5	-33.2	-33.4	0.471	0.400	0.557
40.0	-28.1	-27.1	-25.5	0.343	0.251	0.207
42.0	-26.8	-21.6	-21.2	0.333	0.170	0.138
Results for K_{NN} = 6.84		K_{NNN} = -1.37				
Temp.						
25.0	-88.0	-89.1		0.943	0.949	
30.0	-76.3	-76.5	-76.4	0.869	0.870	0.869
32.0	-69.2	-69.6	-69.2	0.816	0.821	0.817
34.0		-60.7	-60.7		0.748	0.750
35.0	-57.7	-55.6	-55.5	0.726	0.693	0.701
36.0	-48.2	-51.9	-51.0	0.596	0.663	0.656
37.0	-42.0	-43.0	-44.2	0.520	0.545	0.570
38.0	-39.6	-36.4	-35.0	0.502	0.423	0.398
39.0	-33.6	-30.5	-30.4	0.408	0.304	0.314
41.0	-27.5	-23.8	-22.8	0.295	0.200	0.112
Results for K_{NN} = 8.20		K_{NNN} = 0.0				
Temp.						
25.0	-87.9	-88.1		0.941	0.943	
29.0	-77.6	-77.5	-77.7	0.873	0.872	0.874
31.0	-70.0	-70.3	-70.5	0.817	0.817	0.819
32.0	-65.6	-66.6	-66.7	0.781	0.787	0.788
33.0	-61.2	-61.9	-61.2	0.735	0.744	0.738
34.0	-55.1	-55.3	-56.5	0.675	0.670	0.691
35.0	-49.2	-50.0	-49.5	0.586	0.612	0.603
36.0	-42.8	-42.8	-41.5	0.504	0.507	0.436
37.0	-34.2	-36.8	-36.2	0.362	0.387	0.360
38.0	-34.7	-31.3	-31.0	0.397	0.260	0.218
40.0	-32.3	-26.9	-25.7	0.238	0.180	0.101

Table 6. Continued

Lattice Size	Energy 4×4×12	Energy 6×6×18	Energy 8×8×24	Sublattice Magnetization 4×4×12	Sublattice Magnetization 6×6×18	Sublattice Magnetization 8×8×24
Results for K_{NN} = 10.28		K_{NNN} = 2.05				
Temp.						
24.0	-88.9	-89.1		0.943	0.943	
26.0	-83.6	-84.1	-84.0	0.904	0.907	0.908
28.0	-76.4	-77.8	-78.0	0.844	0.858	0.861
29.0	-74.4	-73.3	-72.8	0.832	0.820	0.813
30.0	-69.5	-69.3	-68.8	0.786	0.782	0.794
31.0	-64.2	-64.6	-63.7	0.712	0.727	0.719
32.0	-58.8	-57.6	-56.2	0.659	0.633	0.608
33.0	-49.0	-47.7	-49.0	0.503	0.418	0.464
34.0	-42.9	-42.4	-41.6	0.368	0.328	0.265
35.0	-41.2	-38.0	-37.9	0.341	0.213	0.169
36.0	-39.7	-35.8	-36.1	0.348	0.172	0.119
38.0		-32.8	-32.5		0.128	0.068
	1st Neighbor Correlation			2nd Neighbor Correlation		
Results for K_{NN} = 5.86		K_{NNN} = -2.35				
Temp.						
25.0	- 0.906	- 0.905		0.902	0.902	
30.0	- 0.794	- 0.780	- 0.788	0.788	0.772	0.778
32.0	- 0.714	- 0.716	- 0.719	0.699	0.702	0.706
34.0	- 0.645	- 0.635	- 0.644	0.627	0.619	0.623
35.0	- 0.598	- 0.594	- 0.594	0.575	0.567	0.569
36.0	- 0.500	- 0.549	- 0.546	0.467	0.521	0.521
37.0	- 0.488	- 0.482	- 0.485	0.460	0.444	0.451
38.0	- 0.434	- 0.396	- 0.436	0.396	0.356	0.395
39.0	- 0.386	- 0.350	- 0.352	0.346	0.304	0.301
40.0	- 0.304	- 0.288	- 0.277	0.246	0.236	0.218
42.0	- 0.293	- 0.236	- 0.233	0.242	0.176	0.174
Results for K_{NN} = 6.84		K_{NNN} = -1.37				
Temp.						
25.0	- 0.894	- 0.904		0.890	0.901	
30.0	- 0.780	- 0.780	- 0.778	0.760	0.764	0.764
32.0	- 0.704	- 0.709	- 0.706	0.680	0.689	0.684
33.0	- 0.670			0.644		
34.0		- 0.619	- 0.621		0.589	0.589
35.0	- 0.590	- 0.568	- 0.571	0.552	0.531	0.530
36.0	- 0.498	- 0.536	- 0.526	0.445	0.489	0.477
37.0	- 0.437	- 0.445	- 0.458	0.379	0.387	0.401
38.0	- 0.416	- 0.377	- 0.366	0.346	0.310	0.296
39.0	- 0.355	- 0.324	- 0.324	0.284	0.242	0.243
41.0	- 0.294	- 0.258	- 0.246	0.206	0.170	0.152

Table 6. Continued

Lattice Size	1st Neighbor Correlation 4×4×12	6×6×18	8×8×24	2nd Neighbor Correlation 4×4×12	6×6×18	8×8×24
Results for K_{NN} = 8.20		K_{NNN} = 0.0				
Temp.						
25.0	- 0.893	- 0.896		0.889	0.889	
29.0	- 0.791	- 0.788	- 0.790	0.770	0.767	0.770
31.0	- 0.710	- 0.714	- 0.714	0.677	0.683	0.682
32.0	- 0.665	- 0.677	- 0.679	0.629	0.636	0.638
34.0	- 0.549	- 0.561	- 0.575	0.494	0.500	0.515
35.0	- 0.496	- 0.507	- 0.506	0.428	0.433	0.428
36.0	- 0.434	- 0.434	- 0.423	0.349	0.344	0.324
37.0	- 0.343	- 0.378	- 0.368	0.239	0.267	0.260
38.0	- 0.357	- 0.321	- 0.313	0.241	0.203	0.193
40.0	- 0.279	- 0.270	- 0.267	0.157	0.146	0.138
Results for K_{NN} = 10.28		K_{NNN} = 2.05				
Temp.						
24.0	- 0.897	- 0.899		0.889	0.890	
26.0	- 0.841	- 0.844	- 0.847	0.821	0.824	0.826
28.0	- 0.763	- 0.781	- 0.782	0.724	0.745	0.746
29.0	- 0.745	- 0.728	- 0.725	0.699	0.685	0.677
30.0	- 0.695	- 0.686	- 0.681	0.634	0.628	0.623
31.0	- 0.627	- 0.636	- 0.625	0.544	0.561	0.548
32.0	- 0.575	- 0.558	- 0.541	0.483	0.460	0.436
33.0	- 0.459	- 0.446	- 0.462	0.326	0.305	0.326
34.0	- 0.396	- 0.388	- 0.383	0.237	0.232	0.217
35.0	- 0.383	- 0.335	- 0.339	0.224	0.158	0.159
36.0	- 0.360	- 0.318	- 0.322	0.194	0.143	0.145
38.0		- 0.286	- 0.285		0.112	0.106

Specific Heat Results

Results for K_{NN} = 5.86	K_{NNN} = -2.35		K_{NN} = 6.84	K_{NNN} = -1.37	
Temp.					
25.0	0.445	0.454	0.485	0.464	
30.0	0.783	0.706	0.751	0.736	0.761	0.783
32.0	0.937	0.864	0.940	1.200	1.043	0.870
34.0	1.168	1.157	1.107		1.114	0.990
35.0	1.440	1.429	1.217	1.109	2.075	1.156
36.0	1.553	1.461	1.313	1.341	1.299	1.166
37.0	1.272	1.437	1.412	1.165	1.969	1.601
38.0	1.285	1.950	1.874	1.098	1.565	1.697
39.0	1.225	1.334	1.736	1.169	1.160	1.447
41.0				0.726	0.522	0.419
42.0	0.900	0.456	0.422			

Table 6. Concluded

Lattice Size	Specific Heat Results					
	4×4×12	6×6×18	8×8×24	4×4×12	6×6×18	8×8×24
Results for K_{NN} = 8.20	K_{NNN} = 0.0		K_{NN} = 10.28	K_{NNN} = 2.05		
Temp.						
25.0	0.465	0.460				
26.0				0.695	0.672	0.714
28.0				1.013	0.861	0.788
29.0	0.941	0.743	0.880	0.874	1.056	0.865
31.0	0.811	1.000	0.811	1.625	1.356	1.359
32.0	1.297	1.218	1.022	1.238	1.699	2.012
34.0	1.315	2.001	1.505	0.975	1.011	1.233
35.0	1.811	1.490	2.118	0.942	0.65	0.713
36.0	1.429	1.449	2.944	0.759	0.451	0.533
37.0	1.113	1.311	1.362			
38.0	0.841	0.783	0.639		0.309	0.202
40.0	0.459	0.468	0.277			

Table 7. Data from Monte Carlo Calculations with Impurity Atoms in Model

Lattice Size	Energy			Sublattice Magnetization		
	4×4×12	6×6×18	8×8×24	4×4×12	6×6×18	8×8×24
Temp.						
15.0		-48.7	-48.7		0.993	0.993
18.0	-47.6			0.984		
20.0		-47.1	-47.1		0.976	0.976
25.0	-44.5	-43.9	-43.8	0.944	0.940	0.938
29.0	-40.3			0.890		
30.0		-38.2	-38.2		0.864	0.865
32.0	-35.7	-34.5	-35.0	0.830	0.809	0.818
34.0	-31.2	-31.4	-31.0	0.747	0.760	0.753
36.0	-27.4	-25.7	-26.8	0.681	0.630	0.670
37.0	-24.5	-23.8	-24.4	0.605	0.600	0.612
38.0	-19.8	-20.5	-21.0	0.486	0.504	0.513
39.0	-19.7	-17.6	-17.6	0.480	0.369	0.396
40.0	-15.8	-14.7	-14.4	0.385	0.259	0.200
42.0	-13.8	-12.6	-12.1	0.302	0.184	0.114

Table 8. Neutron Diffuse Scattering Data

Data from the (100) Brillouin Zone in a Direction Perpendicular to the Spin Direction

Wavevector ($Å^{-1}$) / Temperature	Neutron Counts in 10 Minutes 38.8 K	41.2 K	77 K
0.12	343	238	41
0.13	289	175	21
0.14	258	171	31
0.16	199	151	36
0.18	136	119	13
0.20	135	94	19
0.22	107	84	17
0.24	88	87	13
0.26	80	86	21
0.28	77	75	21
0.30	66	66	36
0.32	66	58	28
0.34	55	63	31
0.36	76	74	40
0.38	48	48	24
0.40	38	52	25

Data from the (100) Brillouin Zone in a Direction Parallel to the Spin Direction

Wavevector ($Å^{-1}$) / Temperature	Neutron Counts in 10 Minutes 38.8 K	41.2 K	77 K
0.09	333	235	57
0.10	285	201	38
0.11	231	149	26
0.12	190	136	17
0.13	164	111	15
0.14	146	115	13
0.16	167	117	27
0.18	138	101	17
0.20	118	94	22
0.22	101	94	35
0.24	76	90	26
0.26	79	59	13
0.28	53	50	14

Table 8. (Concluded)

Data from the (100) Brillouin Zone in a Direction Parallel to the Spin Direction

Wavevector ($Å^{-1}$) / Temperature	Neutron Counts in 10 Minutes 38.8 K	41.2 K	77 K
0.30	60	58	27
0.32	40	44	29
0.34	39	39	13
0.36	25	34	19
0.38	47	57	25
0.40	33	33	07

Data from the (111) Brillouin Zone in a Direction Parallel to the Spin Direction

Wavevector ($Å^{-1}$) / Temperature	Neutron Counts in 10 Minutes 37.5 K	41.1 K	77 K
0.10	-17	-09	-03
0.12	-06	-16	-16
0.14	-08	-09	-11
0.16	13	29	15
0.18	-11	08	-05
0.20	-04	-05	04
0.24	-14	05	01
0.26	07	06	05
0.28	08	10	09
0.30	-06	03	05
0.32	01	06	06
0.34	10	05	07
0.36	-03	-02	04
0.38	01	-07	05
0.40	10	13	0

Table 9. Monte Carlo Spin Correlation Results

Shell Radius (Å)	Normalized Spin Correlation Coefficients			
Temperature	41 K	42 K	43 K	45 K
Model Size	(20 × 20 × 30)	(20 × 20 × 30)	(20 × 20 × 30)	(8 × 8 × 24)
3.72	-0.278	-0.259	-0.246	-0.224
4.68	0.181	0.164	0.151	0.133
5.98	-0.128	-0.108		-0.083
7.45	0.112	0.094	0.083	0.071
7.68		-0.084	-0.073	
8.11		0.065	0.058	
9.00	-0.084	-0.064		-0.041
9.37		0.052	0.046	
11.17	-0.058	-0.044	-0.034	-0.026
13.90	-0.042	-0.028		-0.014
14.05		0.021	0.019	
14.90		0.022	0.017	
15.36		0.021	0.016	
16.01	-0.030	-0.016		-0.011
17.27		0.014	0.016	
17.37	0.031	0.017		0.008
18.62		-0.012	-0.010	
18.74		0.010	0.009	

Table 10. Neutron Diffraction Form Factor Data

Miller Indices	Bragg* Integrated Intensity	Form Factor Obtained from Neutron Data	Statistical Error
(100)	1115	330	± 2.0
(300)	64.5	52.6	± 0.5
(533)	12.9	33.7	± 0.7
(522)	17.6	25.3	± 0.5
(311)	119.1	104	± 1.0
(511)	9.44	10.7	± 0.3
(322)	64.1	154	± 2.0
(533)	13.7	35.7	± 0.8
(300)	64.1	52.3	± 0.5
(111)	304.7	16.3	± 1.5
(122)	63.2	51.6	± 0.5
(133)	11.3	11.7	± 0.3
(155)	4.07	6.18	± 0.3
(144)	13.1	18.9	± 0.3
(133)	58.1	74.1	± 0.7
(122)	193.1	231	± 2.0

*Intensities have been corrected for background scattering and extinction.

Table 11. Calculated Diffuse Cross Section Data

	T = 38.8 K		T = 41.2 K		T = 80 K	
	-60.4	14.8	-60.4	14.8	-60.4	14.8
.08	444		252		25.1	
.10	306		207		24.8	
.12	228	308	171	228	24.7	32.6
.14	186	250	143	190	24.5	32.2
.16	153	205	120	160	24.1	31.8
.18	121	165	101	135	23.8	
.20	96	131	86	116	23.5	30.6
.22	80	109	74	100	22.9	30.1
.24	71	97	65	87	22.6	29.4
.26	63	87	57	78	22.1	28.8
.28	54	75	51	68	21.7	28.1
.30	46	64	44	60	21.4	27.5
.32	40	56	40	55	20.6	26.9
.34	37	51	35	49	20.3	26.2
.36	34	47	32	45	19.8	25.6
.38	31	44	30	41	19.2	25.0
.40	29	39	28	37	18.8	24.5

Table 12. Resolution Ellipsoid Parameters

XX	XY	YY	ZZ
2020.	-250.	6920.	3080.

APPENDIX D

TRUNCATION ERROR ANALYSIS

The cross section for diffuse scattering, Equation (58), contains the double sum

$$\sum_{\vec{\ell}',\vec{d}'} \sum_{\vec{\ell},\vec{d}} e^{-i\vec{K}\cdot(\vec{\ell}'+\vec{d}')} e^{i\vec{K}(\vec{\ell}+\vec{d})} \left[< \sigma(\vec{\ell}',\vec{d}')\sigma(\vec{\ell},\vec{d}) > \right. \tag{D-1}$$

$$\left. - < \sigma(\vec{\ell}',\vec{d}') > < \sigma(\vec{\ell},\vec{d}) > \right].$$

Above the ordering temperature the sublattice magnetization goes to zero, and the double sum has the form

$$\sum_{\vec{\ell}',\vec{d}'} \sum_{\vec{\ell},\vec{d}} e^{-i\vec{K}\cdot(\vec{\ell}'+\vec{d}')} e^{i\vec{K}\cdot(\vec{\ell}+\vec{d})} < \sigma(\vec{\ell}',\vec{d}')\sigma(\vec{\ell},\vec{d}) >. \tag{D-2}$$

Now if the translational invariance of a very large crystal is assumed, the double sum can be reduced to the single sum

$$N \sum_{\vec{\ell},\vec{d}} e^{-i\vec{K}\cdot(\vec{\ell}+\vec{d})} < \sigma(\vec{\ell},\vec{d})\sigma(\vec{0},\vec{0}) >, \tag{D-3}$$

where N is the number of ion sites in the crystal. In general, this infinite sum cannot be evaluated exactly. Instead, it is necessary to approximate the sum with a finite number of terms. An estimation of the

truncation error must then be made.

To estimate the truncation error in the sums used in the cross sections described in Chapter IV, the sum (Equation (D-3)) will be broken into two sums. The first sum will contain all the terms for which $|\vec{\ell}+\vec{d}| \leq R$, and the second sum will contain all of the terms for which $|\vec{\ell}+\vec{d}| > R$. Several assumptions will now be made. First, it will be assumed that R is large enough to allow the sum with $|\vec{\ell}+\vec{d}| > R$ to be replaced by an integral. Next, it is assumed that R is so large that the behavior of the spin correlation coefficients can be approximated by the Ornstein-Zernike form. Finally, the antiferromagnetic character of the sum with $|\vec{\ell}+\vec{d}| > R$ (change of sign of $<\sigma(\vec{\ell},\vec{d})\ \sigma(\vec{0},\vec{0}) >$) will not be treated.

With these assumptions, the second sum can be rewritten as follows.

$$\sum_{|\vec{\ell}+\vec{d}| > R} e^{-i\vec{K}\cdot(\vec{\ell}+\vec{d})} < \sigma(\vec{\ell},\vec{d})\sigma(\vec{0},\vec{0}) > \qquad \text{(D-4)}$$

$$\approx \frac{2}{V_o} \int_R^\infty e^{-i\vec{K}\cdot\vec{r}}\ C\ \frac{e^{-\kappa|\vec{r}|}}{|\vec{r}|}\ dV$$

where V_o is the volume of the real space unit cell of $FeCO_3$. The factor of two comes from the fact that there are two magnetic ions in each unit cell of $FeCO_3$. For convenience in evaluating this integral, the Z axis will be assumed to lie along the diffraction vector K. The integration proceeds as follows.

$$\frac{2}{V_o}\int_R^\infty\int_o^\pi\int_o^{2\pi}\frac{Ce^{-\kappa r}}{r}\ e^{iKr\cos(\theta)}\ r^2\sin(\theta)d\phi d\theta dr \tag{D-5}$$

$$=\frac{4\pi C}{V_o}\int_R^\infty\int_o^\pi e^{-\kappa r}\ e^{iKr\cos(\theta)}\ r^2\sin(\theta)d\theta dr$$

$$=\frac{4\pi C}{V_o}\int_R^\infty\left(\frac{e^{-\kappa r}\ e^{iKr}}{iK}-\frac{e^{-\kappa r}\ e^{-iKr}}{iK}\right)dr$$

$$=\frac{4\pi C}{V_o K}\left(\frac{e^{iKR}}{(\kappa-iK)i}-\frac{e^{-iKR}}{(\kappa+iK)i}\right)e^{-\kappa R}$$

Using well known identities, the last form of the integral can be reduced to

$$\frac{8\pi C}{V_o K(\kappa^2+K^2)}\left[\kappa\sin(KR)+K\cos(KR)\right]e^{-\kappa R}. \tag{D-6}$$

The expression in Equation (D-6) was evaluated with appropriate constants and compared with the corresponding finite sums used in the cross section calculations. In every case, the magnitude of R was chosen so that the truncation error, Equation (D-6), was less than five percent of the finite sum. In most cases, the truncation error was actually closer to two percent.

A preliminary estimate of the size of R needed to limit the truncation error to a given percentage can be made using the following results. If the isotropic, ferromagnetic Ornstein-Zernike form is assumed for the spin correlation coefficients for all r, then the sum (D-3) can again be approximated by an integral that can be evaluated by the same method that

was used to evaluate the integral (D-5). The result is

$$\frac{8\pi C}{V_o(K^2+\kappa^2)} \tag{D-7}$$

Now the truncation error, Equation (E-6) can be divided by this approximation of the entire sum to give the ratio

$$P = \frac{1}{K}\left[\kappa \sin(KR) + K \cos(KR)\right] e^{-\kappa R}. \tag{D-8}$$

Now it is clear that

$$P \leq \frac{1}{K}(\kappa+K)\ e^{-\kappa R} \tag{D-9}$$

so that an estimate of the fractional truncation error is given by

$$\left(\frac{\kappa}{K} + 1\right) e^{-\kappa R}. \tag{D-10}$$

For example, at 41.2 K, the inverse range parameter κ has a value of 0.097 $Å^{-1}$, and a typical value for K is 0.25 $Å^{-1}$. For these values, Equation (D-10) indicates that truncating the finite sum at a radius of R = 40 Å will produce an error that is on the order of three percent. There are approximately 5,330 neighbors within this radial distance of a central Fe^{2+} ion in iron carbonate. Because every iron ion is an inversion center, only half of these ions or 2,665 ions, must be included in the sum given in Equation (63).

BIBLIOGRAPHY

1. R. A. Alikhanov, Soviet Physics-JETP, 9, 1204 (1959).

2. I. S. Jacobs, Journal of Applied Physics, 34, 1106 (1963).

3. M. Foex, Annals of Physics, 16, 174 (1921).

4. H. Bizette, Journal of Physics Radium, 12, 161 (1951).

5. I. S. Jacobs, Private Communication.

6. A. Mookherji and S. C. Mathur, Journal of the Physical Society of Japan, 20, 1336 (1965).

7. I. N. Kalinkina, Soviet Physics-JETP, 16, 1432 (1963).

8. D. B. Langille and D. C. O'Shea, Bulletin of the American Physical Society, 17, 269 (1972).

9. Y. A. Popkov, V. V. Eremenko, V. I. Fomin, and A. P. Mokhir, Soviet Physics-Solid State, 14, 2294 (1972).

10. G. A. Prinz, D. W. Forester, and J. L. Lewis, Physical Review B, 8, 2155 (1973).

11. N. Koon, Ph.D. Dissertation, Georgia Institute of Technology, 1969 (Unpublished).

12. H. N. Ok, Physical Review, 185, 472 (1969).

13. A. Okiji and Kanamori, Journal of the Physical Society of Japan, 19, 908 (1964).

14. D. E. Wrege, S. Spooner, and H. A. Gersch, American Institute of Physics Conference Proceedings, 5, 1334 (1972).

15. J. Kanamori, Progress of Theoretical Physics, 20, 890 (1958).

16. J. S. Smart, Effective Field Theories of Magnetism, W. B. Saunders Company, Philadelphia and London (1966), p. 61.

17. P. Weiss, Journal of Physics Radium, 4, 661 (1907).

18. T. Oguchi, Progress of Theoretical Physics, 13, 148 (1955).

BIBLIOGRAPHY (Continued)

19. P. W. Kastelijn and J. Van Kranendonk, Physica, 22, 317 (1956).

20. R. E. Peierls, Cambridge Philosophical Society, Proceedings, 32, 477 (1936).

21. C. S. Rushbrooke and P. J. Wood, Molecular Physics, 1, 258 (1958).

22. C. Domb and M. F. Sykes, Physical Review, 128, 168 (1962).

23. J. W. Essam and M. E. Fisher, Journal of Chemical Physics, 38, 802 (1963).

24. M. Fisher, Reports on Progress in Physics, 30, 615 (1967).

25. G. A. Baker, Jr. and D. S. Gaunt, Physical Review, 155, 545 (1967).

26. M. E. Fisher and R. J. Burford, Physical Review, 156, 583 (1967).

27. J. Als-Nielsen and O. Dietrich, Physical Review, 153, 706 (1967).

28. N. Metropolis, A. W. Rosenbluth, M. N. Rosenbluth, A. H. Teller, and E. Teller, Journal of Chemical Physics, 21, 1087 (1953).

29. A. Tucciarone, H. Y. Lau, L. M. Corless, A. Delapalme, and J. M. Hastings, Physical Review B, 4, 3206 (1971).

30. H. Mook, Private Communication.

31. J. S. Griffith, Theory of Transition-Metal Ions, Cambridge V. P., Cambridge, Mass. (1961), p. 357.

32. Y. Yamada, Journal of the Physical Society of Japan, 15, 429 (1960).

33. W. Marshall and S. W. Lovesey, Theory of Thermal Neutron Scattering, Oxford University Press, Clarendon Press (1971), p. 9.

34. O. Steinsvoll, Physical Review, 161, 499 (1967).

35. L. Van Hove, Physical Review, 95, 249 (1954).

36. W. Marshall and S. W. Lovesey, Theory of Thermal Neutron Scattering, Oxford University Press, Clarendon Press (1971), p. 21.

37. L. D. Fosdick, Methods in Computational Physics, 1, Ed's. B. Alder, S. Ferwback, and M. Rotenberg, Academic Press, New York and London (1963), p. 245.

BIBLIOGRAPHY (Concluded)

38. R. W. G. Wycoff, Crystal Structures, Volume II, Interscience, New York (1964), p. 362.

39. The author wishes to thank Dr. M. K. Wilkinson, Oak Ridge National Laboratory, for the chemical analysis of the Bragg sample.

40. D. E. Wrege, Ph.D. Dissertation, Georgia Institute of Technology, 1971 (Unpublished).

41. M. J. Cooper and R. Nathans, ACTA Crystallographica, A24, 481 (1968).

42. M. J. Cooper and R. Nathans, ACTA Crystallographica, 14, 357 (1967).

43. W. C. Hamilton, ACTA Crystallographica, 10, 629 (1957).

44. E. Schrödinger, Statistical Thermodynamics, Cambridge University Press, Cambridge (1964), p. 25.

45. D. P. Landau, Private Communication.

46. I. Maartense, Physical Review B, 6, 4324 (1972).

47. G. Herzberg, Atomic Spectra and Atomic Structure, Dover Publications, Inc., New York (1944), p. 140.

48. P. J. Brown and J. B. Forsyth, Proceedings of the Physical Society, 92, 124 (1967).

49. C. A. Tracy and B. M. McCoy, Physical Review Letters, 31, 1500 (1973).

50. R. E. Watson and A. J. Freeman, ACTA Crystallographica, 14, 27 (1961).

51. W. Marshall and S. W. Lovesey, Theory of Thermal Neutron Scattering, Oxford University Press, Clarendon Press (1971), p. 152.

52. E. J. Lisher and J. B. Forsyth, ACTA Crystallographica, A27, 545 (1971).

VITA

Ralph Frederick Altman was born in Denver, Colorado on November 23, 1941. He is the son of the late Fred C. Altman and Nina B. Altman.

He attended public schools in Chattanooga, Tennessee and graduated from Chattanooga High School in June, 1960. He entered the Georgia Institute of Technology in September, 1960 and received the degree of Bachelor of Mechanical Engineering with honors in June, 1966. During his undergraduate studies, he worked as a co-operative trainee at the Lockheed-Georgia Company. He received a Western Electric Fund Scholarship during his senior year. He entered the Graduate Division of the Georgia Institute of Technology and held a NDEA Fellowship and a United States Steel Foundation Fellowship. He received the degree Master of Science in Physics in June, 1969.

In August, 1969, Mr. Altman was married to Dorothy Holmes Alleyn, and they have two daughters, Sherrie Lynn Altman and Carol Renee Altman.